

Fabrication and Spectroscopic Studies of Low Dimensional Silicon

Ph.D. Thesis

By

Priyanka Yogi



**DISCIPLINE OF PHYSICS
INDIAN INSTITUTE OF TECHNOLOGY INDORE
September 2018**

Fabrication and Spectroscopic Studies of Low Dimensional Silicon

A THESIS

*Submitted in partial fulfilment of the
requirements for the award of the degree
of*

DOCTOR OF PHILOSOPHY

By

Priyanka Yogi



**DISCIPLINE OF PHYSICS
INDIAN INSTITUTE OF TECHNOLOGY INDORE
September 2018**



INDIAN INSTITUTE OF TECHNOLOGY INDORE

CANDIDATE'S DECLARATION

I hereby certify that the work which is being presented in the thesis entitled “**Fabrication and Spectroscopic Studies of Low Dimensional Silicon**” in the partial fulfillment of the requirements for the award of the degree of **DOCTOR OF PHILOSOPHY** and submitted in the **DISCIPLINE OF PHYSICS, INDIAN INSTITUTE OF TECHNOLOGY INDORE**, is an authentic record of my own work carried out during the time period from December 2014 to August 2018 under the supervision of Dr. Rajesh Kumar, Associate Professor, Discipline of Physics, IIT Indore and Dr. J. Jayabalan, Scientific Officer G, Raja Ramanna Centre for Advanced Technology Indore.

The matter presented in this thesis has not been submitted by me for the award of any other degree of this or any other institute.

Signature of the student with date
Priyanka Yogi

This is to certify that the above statement made by the candidate is correct to the best of our knowledge.

Signature of Thesis Supervisor #1 with date Signature of Thesis Supervisor #1 with date

Dr. Rajesh Kumar

Dr. J. Jayabalan

Priyanka Yogi has successfully given her Ph.D. Oral Examination held on.....

Signatures of Thesis Supervisors
Date:

Signature of External Examiner
Date:

Convener, DPGC
Date:

Signature of PSPC Member #1
Date:

Signature of PSPC Member #2
Date:

Signature of chairman (OEB)
Date:

Dedicated to
My late Grand Maa,
late Khushboo Ma'am

&
Lord Anjaneya



Acknowledgement

With the divine grace of supreme power, I must say, it is the moment when journey of four years come to an end. There have been many people who have walked alongside me during the last four years. They have guided me, placed opportunities in front of me and showed me the doors that might be useful to open. At this occasion, I have many people to thank with open arms for their help, kindness and probably words will fall short.

First and foremost my sincerest thank and gratitude are extended to my guide and path-finder Dr. Rajesh Kumar, (Guru ji) for his guidance and motivation. He has been a tremendous mentor for me. His constant support, valuable advices, constructive criticism and extensive discussion helped me in accomplishing my Ph.D. He has been inculcating inspiration, strength, knowledge, hard work and confidence like qualities and remain source of light throughout my path of journey. He made me to think differently and nourished my reasoning, analytical and writing ability. He not only enriched my subject knowledge but also taught me about challenges of life and win over them. I feel privileged and honoured to being a disciple of him.

I express my sense of indebtedness to my co guide Dr. J. Jayabalan, scientist G (RRCAT, Indore) for his heartfelt support, invaluable guidance, and suggestions to enrich my knowledge. His vision, sincerity, appreciation, energy and enthusiasm towards research always motivated me. He has taught me the methodology to carry out the research and to present the research works as clearly as possible. He is a teacher with great intellectual integrity who kept me abreast of latest scientific knowledge and technologies. I must express deep sense of gratitude to Dr. Pankaj Sagdeo for guidance and support during my research work. He has played a wonderful role of catalyst as well as mentor and helped me in getting in depth learning of subject.

I express my sincere gratitude to Prof. Pradeep Mathur (Director, IIT Indore), who has been highly encouraging during the entire course of my doctoral work.

I would like to express my gratitude towards Dr. Rama Chari (RRCAT, Indore) for her constant support and motivation. I also thanks to Dr. Vivek Kumar (IIIT Chennai) for his guidance and great support and Dr. Ashisha Kumar for scientific discussions that helped me to complete my PhD. I take this opportunity to sincerely acknowledge Prof. A. K. Shukla (IIT Delhi), whose words always motivated and inspired me to do good research. I would like to acknowledge all faculty members of Physics department (IIT Indore) for their kind support and providing me experimental facilities. I want to express my sincere gratitude to Dr. Archana Sagdeo (RRCAT) for always supporting me in my research work. With deep sense of gratitude. I want to thank whole Physics department which was like a family to me in these four years. I never felt alone due to pleasant atmosphere here.

I am truly excited to reveal a sense of respect to Dr. Shailendra Saxena who helped me to start my journey and act as accelerator to complete my research work. I am also indebted to my respected senior and friends Dr. G. Sahu, Dr. Hari Mohan Rai, Ravikiran Late, Dr. Swarup Roy, Dr. K.D Shukla, Vikas Mishra, Dr. Suryakant Mishra, Kamal Warsi, Preetam Singh, Anil Kumar, Sandep Jain, Pooja, Deepika, Rupnayan, Balal, Haardik, Devesh, Aanchal, Anjali, Simran, Manushree, Ritu, Monika, Rahul Kumar, Bajrang for providing friendly and pleasant environment in the Lab. I have great pleasure in acknowledging my gratitude to my fellow research scholars Dr. Tulika, Mithun, Rathinavelu, Arvind, Kavita, Ankit, Shalu and Arjun for their support, encouragement, credible ideas, criticism and contributions that helped me to complete this journey. While writing this thesis I am filling very happy and joyous and as well as wistful for leaving my friends.

I owe my deepest gratitude to my parents and family for all the sacrifice they made on behalf of me. I also express thank to my In-law family for their support, unconditional love and affection and without,

this achievement could not be possible. Words can't express how grateful I am to my mother. Her prayers and blessings helped me to sustain throughout this journey. A profound sense of gratitude binds me to my brother Dr. Arvind Yogi he has been the backbone in moulding my academic career and enhancement of my capabilities. I shall be forever grateful for his guidance, love and gentle care. I would like to pay high regards to my sisters Kusum, Sonia, Neelam Rachna and Kiran for their unconditional love and care.

Words are short to express my thankfulness to Dr. Rupsha Roy for the affection she poured, generous and sisterly care during my PhD work. She was always there when I really needed and her ideals, concepts and suggestions have remarkably influenced me.

It would be inappropriate if I omit to mention the name of my friends Dr. Ashok Pachar, Dr. Anita, Dr. Anil, Ms. Sneha, Ms. Chainika Malhotra, who assisted me as per their abilities in whatever manner possible and ensuring that good times keep flowing. My acknowledgement would be incomplete without thanking my loving husband Dr. Rajesh Kumar Yogi, for immense love, care, affection, and being a pillar of support always for me. I would like to pay homage by dedicating my thesis to late Ms. Khusboo for her motherly care and affection during her fight with life.

I sincerely thank Dr. Vasant Sathe , Dr. U.P. Deshpande, Dr. N.P. lalla, Dr. Salahuddin Khan, Mr. Puspun Mondal and Mrs. Asha Singh for providing me experimental facilities and their support. I thank SIC IIT Indore, most specifically Mr. Kinny Pandey, Mr. Nitin Uppadhaya, Sarita Batra mam, Mr. Ujwal Kulkarni and Mr. Ghanshyam for their support.

I also acknowledge MHRD for providing me financial assistance.

I would like to thank Dr. Shilpa Raut and all staff members of IIT dispensary for taking care of my health and kept me fit so that only I could work efficiently. This journey would not have been possible without the help provided by staff and employees of transport department, I am also thankful to them. I thank the estate section (IIT Indore) for providing me research infrastructure. I want to thank all

staff member of IIT Indore and all those persons whose names may have missed here but contributed throughout the journey of four years to achieve this feat.

I want to thank Lord Hanuman, Lord Krishna to whom I owe my very existence for providing me this opportunity and instilling capability and strength to succeed. I am grateful to them for provision of joys, challenges and grace for growth that have been bestowed upon me during this research work, and indeed, throughout my life.

Last but not least I extend my deepest sense of gratitude to the words said by Dr. A.P.J Kalam (former president of India and a great scientist) that paved a foundation for my journey to start and being a source of inspiration throughout it.

"You have to dream before your dreams can come true"

Priyanka Yogi

LIST OF PUBLICATIONS

(A) From thesis work

- [1] **P. Yogi**, M. Tanwar, S. K. Saxena, S. Mishra, D. K. Pathak, A. Chaudhary, P. R. Sagdeo, R. Kumar, “Quantifying the Short-Range Order in Amorphous Silicon by Raman Scattering,” *Anal. Chem.*, vol. 90, no. 13, pp. 8123–8129, Jul. 2018.
- [2] **P. Yogi**, S. K. Saxena, A. Chaudhary, D. K. Pathak, S. Mishra, P. Mondal, B. Joshi, P. R. Sagdeo, R. Kumar, “Porous Silicon’s fractal nature revisited,” *Superlattices Microstruct.*, vol. 120, pp. 141–147, Aug. 2018.
- [3] **P. Yogi**, D. Poonia, P. Yadav, S. Mishra, S. K. Saxena, S. Roy, P. R. Sagdeo, R. Kumar, “Tent-Shaped Surface Morphologies of Silicon: Texturization by Metal Induced Etching,” *Silicon*, pp. 1–7, Apr. 2018.
- [4] **P. Yogi**, D. Poonia, S. Mishra, S. K. Saxena, S. Roy, V. Kumar, P. R. Sagdeo, R. Kumar, “Spectral Anomaly in Raman Scattering from p-Type Silicon Nanowires,” *J. Phys. Chem. C*, vol. 121, no. 9, pp. 5372–5378, Mar. 2017.
- [5] S. K. Saxena, **P. Yogi**, S. Mishra, H. M. Rai, V. Mishra, M. K. Warshi, S. Roy, P. Mondal, P. R. Sagdeo, R. Kumar, “Amplification or cancellation of Fano resonance and quantum confinement induced asymmetries in Raman line-shapes,” *Phys. Chem. Chem. Phys.*, vol. 19, no. 47, pp. 31788–31795, 2017.
- [6] **P. Yogi**, S. Mishra, S. K. Saxena, V. Kumar, R. Kumar, “Fano Scattering: Manifestation of Acoustic Phonons at the Nanoscale,” *J. Phys. Chem. Lett.*, vol. 7, no. 24, pp. 5291–5296, Dec. 2016.
- [7] **P. Yogi**, P. Mondal, S. Khan, A. Singh, R. Chari, R. Kumar, J. Jayabalan, “Size and porosity dependent photoluminescence lifetime from silicon nanowires,” (communicated)

(B) Beyond thesis work

- [8] **P. Yogi**, S. K. Saxena, S. Mishra, H. M. Rai, R. Late, V. Kumar, B. Joshi, P. R. Sagdeo, R. Kumar, “Interplay between phonon confinement and Fano effect on Raman line shape for semiconductor nanostructures: Analytical study,” *Solid State Commun.*, vol. 230, pp. 25–29, Mar. 2016.
- [9] **P. Yogi**, S. K. Saxena, P. Yadav, S. Mishra, H. Pandey, H. M. Rai, V. Kumar, P. R. Sagdeo, R. Kumar, “Role of metal nanoparticles on porosification of silicon by metal induced etching (MIE),” *Superlattices Microstruct.*, vol. 94, pp. 101–107, Jun. 2016.
- [10] M. Tanwar, **P. Yogi**, S. Lambora, S. Mishra, S. K. Saxena, P. R. Sagdeo, A. S. Krylov, R. Kumar, “Generalisation of phonon confinement model for interpretation of Raman line-shape from nano-silicon,” *Adv. Mater. Process. Technol.*, vol. 0, no. 0, pp. 1–7, Dec. 2017.
- [11] S. Mishra, **P. Yogi**, P. R. Sagdeo, R. Kumar, “Mesoporous Nickel Oxide (NiO) Nanopetals for Ultrasensitive Glucose Sensing,” *Nanoscale Res. Lett.*, vol. 13, pp. 16, Jan. 2018.
- [12] S. Mishra, S. Lambora, **P. Yogi**, P. R. Sagdeo, R. Kumar, “Organic Nanostructures on Inorganic Ones: An Efficient Electrochromic Display by Design,” *ACS Appl. Nano Mater.*, vol. 1, no. 7, pp. 3715–3723, Jul. 2018.
- [13] S. Mishra, **P. Yogi**, P. R. Sagdeo, R. Kumar, “TiO₂–Co₃O₄ Core–Shell Nanorods: Bifunctional Role in Better Energy Storage and Electrochromism,” *ACS Appl. Energy Mater.*, vol. 1, no. 2, pp. 790–798, Feb. 2018.
- [14] S. Mishra, **P. Yogi**, S. K. Saxena, S. Roy, P. R. Sagdeo, R. Kumar, “Fast electrochromic display: tetrathiafulvalene–graphene nanoflake as facilitating materials,” *J. Mater. Chem. C*, vol. 5, no. 36, pp. 9504–9512, Sep. 2017.
- [15] S. Mishra, **P. Yogi**, S. Saxena, J. Jayabalan, P. R. Sagdeo, R. Kumar “Significant field emission enhancement in ultrathin nano-thorn covered NiO nano-petals,” *J. Mater. Chem. C*, vol. 5, no. 37, pp. 9611–9618, Sep. 2017.
- [16] S. Mishra, H. Pandey, **P. Yogi**, S. Saxena, S. Roy, P. R. Sagdeo, R.

- Kumar, “Interfacial redox centers as origin of color switching in organic electrochromic device,” *Opt. Mater.*, vol. 66, pp. 65–71, Apr. 2017.
- [17] S. Mishra, H. Pandey, **P. Yogi**, S. Saxena, S. Roy, P. R. Sagdeo, R. Kumar, “Live spectroscopy to observe electrochromism in viologen based solid state device,” *Solid State Commun.*, vol. 261, pp. 17–20, Aug. 2017.
- [18] S. Roy, S. K. Saxena, S. Mishra, **P. Yogi**, P. R. Sagdeo, R. Kumar, “Spectroscopic Evidence of Phosphorous Heterocycle–DNA Interaction and its Verification by Docking Approach,” *J. Fluoresc.*, vol. 28, no. 1, pp. 373–380, Jan. 2018.
- [19] S. Roy, S. Mishra, **P. Yogi**, S. K. Saxena, V. Mishra, P. R. Sagdeo, R. Kumar, “Polypyrrole–vanadium oxide nanocomposite: polymer dominates crystallinity and oxide dominates conductivity,” *Appl. Phys. A*, vol. 124, no. 1, pp. 53, Jan. 2018.
- [20] S. Roy, S. K. Saxena, S. Mishra, **P. Yogi**, P. R. Sagdeo, R. Kumar, “Evidence of bovine serum albumin-viologen herbicide binding interaction and associated structural modifications,” *J. Mol. Struct.*, vol. 1139, pp. 447–454, Jul. 2017.
- [21] S. Roy, S. K. Saxena, S. Mishra, **P. Yogi**, P. R. Sagdeo, R. Kumar, “Ecofriendly gold nanoparticles- Lysozyme interaction: Thermodynamical perspectives,” *J. Photochem. Photobiol. B*, vol. 174, pp. 284–290, Sep. 2017.

Contents

Acknowledgement	i
List of Publications	v
List of Figures	xii
List of Tables	xxi
List of Abbreviations	xxii
Chapter 1: Introduction	1-10
Chapter 2: General Overview and Theoretical Background	
2.1 Overview of Si	11
2.1.1 Crystal Structure of Si	11
2.1.2 Phonons in Si	12
2.1.3 Band Structure and Optical Properties of Si	13
2.2 Low-dimension Semiconductor and effect of Reduced Dimensionality	16
2.2.1 Energy Gap Enhancement	16
2.2.2 Modification in the Electron Density of States	18
2.3 Raman Scattering	20
2.3.1 Raman Scattering in Semiconductors	20
2.3.2 Raman Scattering in Crystalline Si	23
2.3.3 Raman Scattering from Poly-/Nano- Crystalline Semiconductor	24
2.3.4 Brillouin Scattering	25
2.4 Raman Study of Electron Phonon Coupling in Heavily Doped n- and p-type Silicon	26
2.5 Raman Spectrum of Amorphous Silicon	29
2.6 Photoluminescence	31

2.6.1 Photoluminescence from Si Nanostructures	31
--	----

Chapter 3: Experimental Methodology and Sample Details

3.1. Sample Preparation	35
3.1.1 Metal Induced Etching Method	36
3.1.2 Laser Induced Etching Method	37
3.2 Instruments' Details	41
3.2.1 Scanning Electron Microscope	41
3.2.1.1 Signals Generated	41
3.2.1.2 Imaging in SEM	42
3.2.2 Transmission Electron Microscopy	43
3.3 Raman Spectroscopy	44
3.4 Diffuse Reflectance Spectroscopy	46
3.5 Photoluminescence Spectroscopy	48
3.6 Time Correlation Single Photon Counting (TCSPC)	49

Chapter 4: Fabrication and Surface Morphology of Silicon Nanostructures

4.1 Surface Morphologies of Si Nanostructures	54
4.2 Porosification Mechanism and Role of Metal	57
4.3 Porosification and Effect of Metal	60
4.3.1 Comparison of Surface Morphology of the Si NSs Fabricated by Different Metal Nanoparticles	60
4.3.2 Band Bending and Surface Texturization	65
4.4 Effect of Doping Level on the Porosification	67
4.5 Summary	75

Chapter 5: Confined Phonon in Low Dimension Silicon

5.1 Raman Studies from Low Dimension Solids: Theoretical Background	77
5.2 Phonon Confinement Model	79

5.2.1 Evolution of Asymmetric Raman Line-Shape for Nanostructures	82
5.2.2 Effect of Size on Raman Line Shape	84
5.2.3 Modified Phonon Confinement Model	86
5.3 Raman Spectroscopy from Si NSs Prepared by MIE	89
5.4. Raman Spectroscopy for Quantification of Short Range Order in Amorphous Si	93
5.5 Summary	100

Chapter 6: Fano Resonance and Fano-scattering in Silicon Nanostructures

6.1 Electron-Optic Phonon Interaction: Fano Resonance	103
6.1.1 Fano Resonance in Crystalline Si	105
6.1.2 Fano Resonance in Quantum Confined Si	110
6.1.3 Fano Resonance in Si Nanostructures: Raman Scattering	115
6.2 Electron Acoustic Phonon Interaction: Fano scattering	119
6.3 Study of Non-radiative Transition in Si Nanostructures by Fano Scattering	126
6.4 Summary	128

Chapter 7: Optoelectronic properties of Silicon Nanostructures

7.1 Band Gap Estimation from Diffuse Reflectance using Kubelka-Munk Function	130
7.1.1 Band Gap Estimation of Si NSs Samples	131
7.1.2 Doping Dependent Band Gap of n- & p-type SiNWs	134
7.2 Photoluminescence of Si NSs	136
7.3 Time Resolved Photoluminescence of Si NSs	137
7.4 Summary	144

Chapter 8: Conclusions and Future Scope

8.1 New scientific Findings in Present Thesis Work	145
8.2 Conclusions	145
8.2 Future Scope	148

Appendices

Appendix 1	149
Appendix 2	153
Appendix 3	155

References	157
-------------------	------------

List of Figures

Figure 1.1: Cartoon displaying various applications of Si NSs	4
Figure 1.2: Various morphologies of Si NSs fabricated using MIE	8
Figure 2.1: Silicon crystal structure	12
Figure 2.2: Phonon dispersion curve of silicon	12
Figure 2.3: Band diagram of silicon	13
Figure 2.4: Interband transitions in (a) direct band gap and (b) indirect band gap solids. The vertical arrow represents the photon absorption while wiggly arrow represents the absorption or emission of a phonon	14
Figure 2.5: Absorption coefficient versus photon energy for Si at room temperature	14
Figure 2.6: Room temperature inter band absorption spectrum of Si	15
Figure 2.7: Energy level diagram of quantum well structure	18
Figure 2.8: Density of states in different confinement configurations (a) bulk, (b) quantum well, (c) quantum wire and (d) quantum dot	20
Figure 2.9: Raman scattering processes in terms of elementary interactions H_{E-L} (Electron-Lattice interaction Hamiltonian), H_{E-R} (Electron-Radiation interaction Hamiltonian), ω_i (frequency of vibrational excitation) and ω_s (frequency of scattered photon). (a) shows first order Raman scattering process whereas (b), (c) shows second-order Raman scattering	22

Figure 2.10: Raman spectrum of c-Si	24
Figure 2.11: Conduction bands of heavily doped n-type c-Si [100]	27
Figure 2.12: Raman lineshape for different value of q (n-type) for negative q values (p-type) for positive q values and bottom panel shows asymmetry ratio for positive and negative q value	28
Figure 2.13: Raman spectrum of the <i>a</i> -Si	30
Figure 3.1: Schematic diagram of step by step formation of SiNWs. (1) cleaned Si wafer, (2) MNPs deposited Si wafer, (3) etched Si wafer, (4) increase etching time and (5) SiNWs after removal of MNPs.	37
Figure 3.2: Experimental set up for the laser induced etching	38
Figure 3.3: Schematic diagram of SEM	42
Figure 3.4: Schematic diagram of TEM	44
Figure 3.5: Schematic diagram of Raman Spectrometer	45
Figure 3.6: Experimental set-up for UV-Vis diffuse reflectance spectroscopy	46
Figure 3.7: Experimental set up for diffuse reflectance measurement (a) Carry 60 UV-Vis spectrometer, (b) an integrating sphere attachment to detect diffuse reflectance	47
Figure 3.8: Schematic diagram of PL setup	48
Figure 3.9: Typical block diagram of a TCSPC instrument	50
Figure 4.1: SEM of clean surface of Si wafer	54
Figure 4.2: Surface morphology of AgNPs deposited Si wafers (a) $N_{Ag}^{\#}$, (b) $P_{Ag}^{\#}$, (c) N_{Ag}^{*} and (d) P_{Ag}^{*}	55
Figure 4.3: Surface morphology of etched Si wafer (a) $N^{\#}$, (b) $P^{\#}$, (c) N^{*} and (d) P^{*}	56

Figure 4.4: Cross sectional SEM image of etched Si samples (a)N [#] , (b)P [#] , (c) N* ['] and (d) P* [']	56
Figure 4.5: The schematic diagram showing redox pair energies with respect to hydrogen electrode potential	57
Figure 4.6: Dissolution mechanism of Si in the HF proposed by Lehmann and Foll	58
Figure 4.7: The schematic diagram depicting the porosification during MIE	59
Figure 4.8: The top panel image are surface morphology of AgNPs deposited n- and p-type Si wafers (sample N _{Ag} [#] and P _{Ag} [#]) and bottom panel shows the top view SEM images of sample N [#] and P [#] respectively	60
Figure 4.9: The top panel images are surface morphologies of AuNPs deposited Si wafer (sample N _{Au} ^{#'''} and P _{Au} ^{#'''}) and bottom panel shows the top view SEM images (surface morphologies) of sample N ^{#'''} and P ^{#'''} respectively	61
Figure 4.10: SEM images used to analyse (using ImageJ) the tent structure in sample N [#] and P ^{#'''} . Inset shows the selected area (marked by red circle) 3D surface plot	62
Figure 4.11: SEM image of sample P ^{#'''} obtained by tilting the sample. The red and black marked line shows the single tent width and height respectively. Inset shows the bending of Si-tent tip	63
Figure 4.12: SEM images used for the ImageJ to analyse the tent structure in sample N ^{#'''} and P [#] . Inset shows the 3D surface plot of corresponding SEM images	64
Figure 4.13: Band diagram along with SEM micrographs	65

showing a correlation between band bending and morphology after porosification

Figure 4.14: Schematic showing mechanism of texturization of Si wafer into nano tent of Si NSs. Red arrows, in step 3, show the direction of force being felt by the wires as a result of surface tension. 66

Figure 4.15: The left panel SEM images are surface morphologies whereas right panel images are X-sectional morphologies of sample P^{*} , $P^{\#}$, N^{*} and $N^{\#}$ respectively 68

Figure 4.16: TEM images of sample $N^{\#}$ and $P^{\#}$ 69

Figure 4.17: TEM image of samples $N^{\#}$ and $P^{\#}$, prepared by MIE. Inset shows the selected area (marked by red dotted line) 3D surface plot of TEM image 70

Figure 4.18: Surface morphologies of samples $N_{Ag}^{\#\prime\prime}$ and $N^{\#\prime\prime}$, top panel shows the AgNPs decorated Si wafer for 60 min and bottom panel shows the surface morphology of corresponding etched Si wafer (sample $N^{\#\prime\prime}$) 71

Figure 4.19: Surface morphologies of samples $P_{Ag}^{\#\prime\prime}$ (pre-porosification) and $P^{\#\prime\prime}$ (post-porosification), top panel shows the AgNPs decorated Si wafer for 60 min and bottom panel shows the surface morphology of corresponding etched Si wafer (sample $P^{\#\prime\prime}$) 72

Figure 4.20: Schematic representation showing the formation of fractal porous silicon (i) AgNPs deposited Si wafer followed by (ii) etching by MIE followed by (iii) non-vertical etching progress and resulting in (iv) porous nanowires present in porous Si matrix with inset showing 74

the actual TEM image of one SiNWs

Figure 5.1: Schematic diagram shows the phonon dispersion and Raman line-shape of Si, where left hand side and right hand side display Raman active optical mode for c-Si and Si NSs, respectively 79

Figure 5.2: Confined NSs in (a) three (sphere), (b) two (column), (a) one (thin film) dimension 81

Figure 5.3: Symmetric Raman line shape for c-Si calculated using Eq. 5.14 and inset shows the dispersion curve for Si evaluated using Eq. 5.13 83

Figure 5.4: (a) Raman line-shapes theoretically generated using phonon confinement model Eq. 5.11 for different Si NSs sizes. Inset shows the asymmetry ratio (left Y-axis) and peak position (right Y-axis) with respect to size of Si NSs.(b) depicted pre-maximum & post maximum sides in Raman line shape and the half widths in lower energy side (γ_L) and higher energy side (γ_H) at $I/2$ i.e. at 50% of the total intensity I 85

Figure 5.5: Raman line-shapes obtained using modified phonon confinement model (Eq. 5.18) for different nano crystallite sizes. Inset shows the variation of asymmetry ratio (left Y-axis) and peak position (right Y-axis) with respect to size of Si NSs 88

Figure 5.6: Raman spectrum from c-Si recorded using photon energy of 2.54 eV 89

Figure 5.7: Raman spectra of Si NSs N^s and N^{*'} for etching time 60 minutes. The experimental data are shown by discrete data points whereas theoretical fitting using Eq. 5.11 is shown as continuous lines 90

Figure 5.8: Raman spectrum from sample P^{*'} (p-type Si NSs, etching time 60 min). The experimental data shown 91

by discrete data points whereas theoretical fitting using Eq. 5.15 is shown as solid line

Figure 5.9: Raman spectra of Si NSs of sample N*’ and N[§] for etching time 60 minutes. The experimental data are shown by discrete data points whereas theoretical fitting using MPCM (Eq. 5.18) is shown as continuous solid lines 92

Figure 5.10: Raman spectra of *a*-Si samples AS1, AS2 and AS3. Left hand inset shows the theoretical Raman line shapes of *c*-Si and Si NSs respectively 94

Figure 5.11: Illustration for depicting various Raman processes involving the scattering from *c*-Si, Si NSs and *a*-Si 95

Figure 5.12: Theoretically simulated curves of Raman shift vs size for Si sphere, column and *a*-Si. The red, green and blue data points correspond to the calculated results for column, sphere and *a*-Si respectively. The pictorial representation corresponds to the shape used to calculate the curve of *a*-Si 98

Figure 5.13: Theoretically obtained Raman line shapes for (a) *c*-Si, (b) SiNSs and (c) *a*-Si displayed in the different circles. The schematic (blue, green and red line on the top of Raman line shape) shows the abrupt transition from *c*-Si to *a*-Si 99

Figure 6.1: Schematic diagram representing Fano resonance 105

Figure 6.2: Theoretical Raman line shapes obtained using Eq. 6.1 for (a) heavily doped n-type *c*-Si (*c*-Si-N) (b) heavily doped p-type *c*-Si (*c*-Si-P) (d) Fano parameter dependent α_R for heavily doped n and p-type Si 107

Figure 6.3: Raman spectra for heavily doped crystalline 109

silicon samples c-Si-N and c-Si-P along with intrinsic c-Si (dotted black line)

Figure 6.4: Theoretical Raman line shapes obtained using Eq. 6.3 for (a) heavily doped n-type low dimensional Si (b) heavily doped p-type low dimensional Si (c) Fano parameter dependent α_R for heavily doped low dimensional for n and p-type Si 112

Figure 6.5: (a) Theoretically obtained Raman line shape for various combinations of q and L using Eq 6.3 (b) the variation of α_R as a function of Fano parameter q for different nanostructure sizes 114

Figure 6.6: Raman spectra for sample N[#] and sample P[#] along with intrinsic c-Si (dotted line). Discrete points represent experimentally observed data while solid lines represent the theoretical Raman line shapes (Eq.6.3). Inset shows the corresponding Raman spectra in wider spectral range to show antiresonance (arrow marked) 116

Figure 6.7: (a) Schematic representation of inter- and intra-band transitions. (b) Graphics to explain various combinations of electronic-discrete energies where Fano interaction is possible 121

Figure 6.8: (a) Raman spectra from sample N25, N45 and N60 containing Si NSs. (b) Size-dependent variation in FWHM and α_R obtained from Raman scattering data shown in (a) 123

Figure 6.9: Raman spectra from samples N25, N45 and N60. Discrete points correspond to the experimental data whereas the solid lines corresponding to the theoretical line-shape calculated using Eq.6.4 125

Figure 6.10: Schematic representation of nonradiative intraband transitions can be extracted using Fano 126

scattering

Figure 6.11: Nonradiative continuum obtained from Fano scattering data corresponding to Si NSs of different size. Dotted line shows constant continuum for c-Si for comparison 127

Figure 7.1: DRA spectra of sample P*['] and P[#]['], discrete data points show the experimentally obtained DRA spectra whereas solid line corresponds to theoretical fitting. Inset (a) & (b) shows the schematic representation of energy band gap of P*['] (along with c-Si) and P[#]['] (along with c-Si) samples respectively etching time 132

Figure 7.2: DRA spectra of sample N[#]['] and N*['], discrete data points show the experimentally obtained DRA spectra whereas solid line corresponds to theoretical fitting. Inset (a) & (b) shows the schematic representation of energy band gap of N[#]['] and N*['] (along with c-Si) samples respectively. 133

Figure 7.3: DRA spectra of sample N[#]['] (low doped) and P[#]['] (highly doped) Si NSs. Discrete data points show the experimentally obtained DRA spectra whereas solid line corresponds to theoretical fitting. Inset (a) & (b) shows the schematic representation of energy band gap of N[#]['] and P[#]['] (along with c-Si) samples respectively. 135

Figure 7.4: PL spectra of sample N*['], N[#]['] and P*['] at RT. Green line over the corresponding experimental points is the best fit to the data with sum of multiple Gaussian peaks. The isolated individual peaks are shown in pink color for all the samples. The inset shows a representative actual photograph of PL emission from the sample N[#]['] when excited using 405 nm source 136

Figure 7.5: The time dependence of the PL intensity of sample N*’, N#’ and P*’ measured using TCSPC. The data is plotted in different time range to show existence of multi exponential decay in the PL intensity. Dots represent the experimental data, the cyan line is the IRF and the red lines are the best fit obtained by fitting the data with Eq. 7.6 convoluted with IRF

Figure 7.6: The dependence of PL life times (τ_2 and τ_3) on the size of the Si nanostructures present in the sample

Figure 7.7: The dependence of amplitude of spatial variation in the material on the spatial frequencies for samples N*’, N#’ and P*’ estimated from TEM image of NWs. For the reader, the length periodicity in density distribution of material that will give rise to signal (I_{SF}) at two frequencies are also shown as vertical lines

List of Tables

Table 3.1: List of Si NSs samples prepared by the MIE using AgNPs	39
Table 3.2: List of Si NSs samples prepared by the MIE using AuNPs	40
Table 3.3: List of Si NSs samples prepared by the LIE using Argon ion laser (514.5nm)	40
Table 3.4: List of amorphous Si samples	40
Table 5.1: Size obtained by fitting the experimental Raman scattering data in Figure 5.7 and 5.8	91
Table 5.2: Raman parameter calculated from fitting of Raman spectra of AS1, AS2 and AS3 with Eq. 5.18. Values of D in the bracket in last column are the sizes estimated using Eq. 5.19	97
Table 6.1: Raman parameters calculated from the theoretically developed Raman line-shape	113
Table 6.2: Raman parameters estimated from Raman spectra of SiNWs samples of N [#] and P [#] by theoretical fitting of experimental data (discrete points in Figure 6.6) with Eq.6.3	118
Table 6.3: Various fitting parameters obtained Eq. 6.5 with experimentally observed Raman spectra. Values in bracket in column 2 represent the nanocrystallite size estimated from optical Raman spectra shown in Figure 6.9	125
Table 7.1: Decay time obtained from the best fit of time dependent PL (Figure 7.5).	139

Abbreviations

Silicon	Si
Nanostructures	NSs
Crystalline Si	c-Si
Porous silicon	Psi
Nanowires	NWs
Metal induced etching	MIE
Metal nanoparticles	MNPs
Silver nanoparticles	AgNPs
Gold nanoparticles	AuNPs
Phonon confinement model	PCM
Modified Phonon confinement model	MPCM
Full width at half maximum	FWHM
Diffuse reflectance absorption	DRA
Photoluminescence	PL
Scanning electron microscope	SEM
Transmission electron microscope	TEM
Time correlation single photon counting	TCSPC
Fast Fourier transformation	FFT
Instrument response function	IRF
Face centered cubic	FCC
Transverse optical	TO
Longitudinal optical	LO
Density of states	DOS
Zone center phonon	ZCP
Laser induced etching	LIE
Asymmetry ratio	α_R

Chapter 1

Introduction

Today, the word “Nano” is omnipresent and ubiquitous, while nanotechnology [1–5] has become benevolent to people of modern world unlike it was confined to a few in earlier days. The impact of nanoscience & nanotechnology is also evident from the discoveries of cryo electron microscopy, molecular machines, optical microscope and ground breaking experiment of Graphene for which scientists across the world namely, Jacques and Richard Henderson, Jean-Pierre Sauvage, Sir J. Fraser Stoddart and Bernard L. Feringa, Erich Betzig, Stefan W. Hall and William E. Moerner, Andre Geim and Kostya Novoselov, won the Nobel prizes in recent years.

Nanotechnology has captured the attention of media, scientific community and public too [6,7] as it offers great potential in improving the well-being of humankind [8]. In simple words, nanotechnology is amalgam of state of the art in physics, chemistry, biology, engineering and many more disciplines and interdisciplinary areas [8]. Being highly converged topic in nature and diversified in applications it can't be, and need not be, defined properly and should not be confined within a single discipline. Science without nanotechnology driven new technological advancement, a smart, blooming, intelligent, sustainable and prosperous transforming world is beyond our imagination.

Looking microscopically, the advancement is a result of miniaturizing induced [9–11] spectrum of novel properties which are usually not observed otherwise. Materials of very low dimensions exhibit interaction and assembling of atoms & molecules into structures which show properties different from its bulk form enabling one to tailor

Chapter 1

properties such as vibrational, electronic and optical etc. [12–14] by simply varying the size of the material in the range of nanometers. For instances opaque substance like copper become transparent, inert material like platinum become catalyst, stable material like aluminium turn combustible, solid like gold turn into liquids at room temperature and even loses conductivity, insulating/semiconducting silicon (Si) becomes conductor and transform into a direct band gap material from an indirect one [8]. Much of the fascination with nanotechnology stems from these unique phenomena that matter exhibits at nanoscale.

Although nanotechnology [15] is a comparatively modern research field (the term “nanotechnology” was first defined by Norio Taniguchi in 1974) [16], central concepts of nanotechnology evolved over a longer period of time. Nanotechnology was used unwittingly since thousands of years in making steel, in vulcanizing rubber, and in paintings (e.g. Lycurgus Cup, Notre Dame Cathedral in Paris). Today from agriculture to aerospace research impact of nanotechnology is being felt. Historically, Richard Feynman’s role is also discussed in the context of nanotechnology [17]. Furthermore, existence of nanometer-scaled structures in nature are now a very well-known fact. Colour of butterfly’s wings imparted by photonic crystals is one such beautiful example. The nanoscale processes relies on the properties of stochastically-formed atomic ensembles of numerous nanometers in size, and is notable from chemistry in that they do not rely on the properties of discrete molecules but rather on the properties that reach more than a few hundreds of atoms.

The first observations and size measurements of nanoparticles were made during the first decade of the 20th century [17,18]. They are mostly associated with Richard Adolf Zsigmondy [18] who made a comprehensive study of gold sols and other nanomaterials with sizes less than 10 nm by use of a dark-field ultra-microscope. Zsigmondy was the first who characterized particle size and used nanometer scale clearly in 1914 [18]. Science is approaching towards technological advancements to extract multiple applications from a single material. These nanostructures offer a wide range of opportunities for

development of nanoscale electronics [19–21], optical devices [20,22], nanomedicine and therapeutics [19]. As mentioned earlier, due to the reduced size, the de Broglie wavelength of elementary excitations within nanostructures (e.g. excitons, electrons and phonons) is of the orders of dimension of the nanostructure itself. In such cases, quantization of energy and momentum are significant factors, modifying material properties based on those elementary excitations (electron and phonon density of states). Indeed, interest in the nanostructures is triggered by the discovery that their physical properties (electronic, optical, thermodynamical) are different from those of the corresponding bulk material due to the effect of quantum confinement. Consequently, the size of nanostructures is a new design parameter for devices. Interestingly, the size dependent changes in physical properties strongly depend on the texturization of semiconductor nanostructures which has become one of the field of great interest recently due to its applications in various fields [23,24] especially the one which improves the light trapping efficiency of semiconductors [25].

It is a well-known fact that Si is the most abundant solid in Earth's crust and said to be the gift of nature to the mankind. Crystalline Si (c-Si) is the most imperative semiconductor for the electronics and photovoltaic industry nowadays, and it has turn out to be cornerstone of our knowledge based society. In its miniaturized form it exhibits fascinating properties and is of great interest as it has a potential of integration with already existing Si electronics industry. According to the present scenario, the Si nanostructure (NSs) is one of the most significant material for current semiconductor industry, due to well-documented capable applications in the fields such as nano-electronics [23–25], optoelectronics [26–28], energy conversion [29–31], energy storage [32], bionic models and chemical or biological sensors [32–35].

The cartoon in Figure 1.1 displays the spectrum of various applications of nanomaterials in general and of Si NSs in particular. Consequently, extensive investigation on Si thin films [36], nanowires (NWs) [36–

39], nanoparticles [40–42], nanotubes [43,44], and porous structures has been carried out over the past couple of decades due to their unique physical properties and various applications ranging from electronics to biophysics [45,46]. Crystalline Si is an indirect band gap semiconductor with band gap of ~ 1.1 eV, which precludes the efficient emission and absorption imparting it relatively poor optical properties. Phonon mediated process emits light in c-Si and emitted light is in the range of near infrared. Additionally, the competitive non-radiative recombination rates in c-Si are much higher than the radiative ones and most of the excited electron-hole pairs recombine nonradiatively. This yields very low internal quantum efficiency of visible luminescence for c-Si [47].

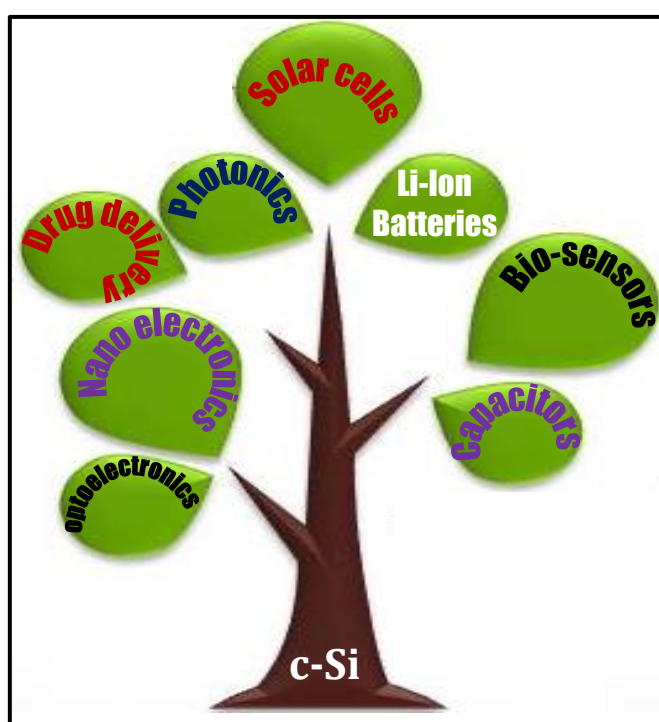


Figure 1.1: Cartoon displaying various applications of Si NSs.

Process of miniaturization converts c-Si into nano-crystalline Si and converts it into a direct band gap material, hence expected to behave differently and is of technological interest. It also plays an important role in the fabrication and improvement in efficiency of solar cells [25]. Miniaturized c-Si with different shape and size has been

fabricated by many groups [25,48,49] by various different methods. As the size of Si becomes comparable to its Bohr radius, various properties get modified compared to its bulk counterpart. Additionally, porous materials [50–52] have also attracted interest due to its unique properties [28,53–55] and many applications [56–58] such as optoelectronics [19,59], nanoelectronics [68,69], sensors [22,45] as well as energy storage [32] devices and many more.

As mentioned above, one of the reasons that enable Si NSs to be used in new applications is the presence of quantum confinement effect. The quantum confinement effect provides the flexibility to tune optical, electrical, chemical and thermal properties of Si. The one dimensional system provides a platform to explore the physical phenomenon taking place at nanoscale [60–62] as well as to observe the dependence of their properties on size and dimension for fundamental research [60,62,63]. Many growth techniques have been developed to prepare Si NSs materials such as electron-beam lithography [64,65], epitaxy [66,67], chemical vapour deposition [68,69] and numerous simple etching techniques [70–72]. Also, many laser-assisted processes such as laser ablation and continuous wave laser annealing of amorphous Si [69], have also been used to engineer Si NSs.

From the last decade metal induced chemical etching (MIE) is one of the most extensively used techniques to prepare Si quantum wires by using the solution of hydrofluoric acid (HF) and hydrogen peroxide (H_2O_2) for the chemical dissolution of Si. The Si NSs fabricated by this process is present as porous Si network, consisting of pores separated by thin walls of Si having thickness in the range of a few to several nanometers. Properties of such materials depend on various experimental parameters such as etching time, concentration of HF and deposition time of metal nanoparticles. In the present study the Si NSs have been prepared by MIE technique [73–78]. This technique is a method of porosification where metal nanoparticles are deposited onto semiconductors followed by etching in an etchant. The metal nanoparticles (MNPs) play a very important role in porosification of Si wafer [79–81].

Chapter 1

Another reason for the increased research activity in the area of Si NSs was observation of [48,55,56] visible photoluminescence (PL) at room temperature. However origin of the same has been a subject of extensive research since its discovery [82] as being an indirect band gap material, Si in its bulk form restrict the emission of light [83] even at low temperatures. Several studies have been carried out by many research groups worldwide to understand the mechanism of this emission. Still the mechanism for emission of visible PL from SiNWs is still in infant state and highly debatable research topic. Several studies explains that the attribute of visible emission is due to the quantum confinement effect on the carriers or due to the strong oxide layer formed on the top of the nanostructures [54,84] with quantum confinement being the most acceptable one for the NSs [83,84]. This model suggests that PL occurs due to the band to band transition of confined charged carriers in Si NSs whose electronic band structure is modified to result in an enhanced band gap. In order to validate the presence of quantum confinement effect, Raman spectroscopy emerged as a superior tool over the others for characterization of Si NSs especially where a quick and extremely sensitive technique is required [85].

Raman scattering [86] in solids, especially semiconductors, occurs from the zone center phonons (the $k=0$ selection rule) [87,88] resulting in a sharp symmetric Raman spectrum having peak position corresponding to zone center phonon frequency. This $k=0$ rule gets relaxed in NSs where phonons other than zone center also participate in the Raman scattering resulting in a red shifted and asymmetrically broaden Raman spectra [88–90]. This happens due to the confinement of phonons within the physical boundary of the NSs. To understand confinement effect in NSs using Raman spectroscopy, Richter *et al.* [91] gave phonon confinement model (PCM) which was improved later by Campbell *et al.* [77] This improved model not only explains the experimental observation but also proves to be very useful in estimating the size and degree of confinement in NSs. Phonon confinement effect in terms of asymmetric Raman line shape in Si NSs

has been investigated very extensively [62,91,92] due to its capability of being extremely useful method in investigating subtle physics at nanoscales.

In addition to confinement effect, Fano resonance [93–95] (electron-phonon interaction) is another factor that can induce asymmetry in Raman spectral line shape [96–98]. In contrary to phonon confinement effect where the broadening occurs in Raman line shape only in pre maximum side, the presence of Fano effect results in increased half width in the pre-maximum side and post-maximum side for heavily doped n- type and p-type Si respectively meaning that it depends on the nature of the system. Therefore in n-type quantum confined system (broadening in the pre maximum side of Raman line shape), Fano effect produces extra broadening in n-type system. On the other hand, for Fano effect in p-type confined system the situation will be entirely different because confinement effect result in increased half width in pre maximum side (appears asymmetric broadening) and Fano effect results the increased half width in post maximum side. By observing these Raman line shape, it will be very difficult to observe the confinement effect. It is necessary and interesting to study the n- and p-type confined systems which possess Fano effect too. Hence there is a need to understand the Fano effect in conjuncture with the framework of phonon confinement to understand the impact of Fano effect on low dimensional systems.

Above mentioned discussion, though looks complicated, is the simplified version of facts that are actual players in the system where both of these effects are present. Looking at the different nature of the two effects and their response on Raman line-shape, a careful analysis is necessary to understand the consolidate effect on the Raman line-shape. The objective of this thesis is to study the effect of quantum confinement and Fano resonance (electron-phonon interaction) on Si NSs using Raman, PL and diffuse reflectance absorption spectroscopy. The Si NSs have been fabricated by MIE [99] technique using different metal nanoparticles as a catalyst. Both n- and p-type Si wafers with doping at different levels are used to fabricate the Si NSs.

Different samples of Si NSs having different sizes and morphologies were prepared by optimizing the etching time and deposition of metal nanoparticles which is displayed in Figure 1.2 just for qualitative purpose and the same will be discussed in great detail in appropriate chapters. Surface and X-sectional morphologies of these samples are studied by electron microscopy. The mechanism responsible for the formation of given Si NSs has been proposed on the basis of electron transfer process from Si to metal ion and metal to H_2O_2 thereafter.



Figure 1.2: Various morphologies of Si NSs fabricated using MIE.

The presences of quantum confinement in Si NSs have been carried out using Raman scattering experiments. The asymmetrical broadening towards pre-maximum side and red shifted (with respect to bulk counterpart) Raman spectra have been observed as a result of quantum confinement effect of optical phonons. The theoretical Raman line shapes have been studied under the frame work of PCM. Raman scattering has been used to study the Fano resonances and Fano scattering, electron-acoustic phonon interaction in Si NSs observed experimentally and later validated by theoretical Raman line shape analysis. Additionally, Raman line-shape analysis from amorphous Si has also been carried out and a universal model has been proposed for quantification of extent of so called “short-range order” in amorphous materials. The visible PL has been observed from the Si NSs prepared

by MIE technique. The origin of visible PL has been investigated by time resolved PL study and its mechanism has been explained on the basis of porosity present in SiNWs.

All the results, discussion and conclusions have been presented in the thesis as per the following chapter-wise plan:

Chapter 1 (current chapter): It provides an introduction and discusses the current status of the problem dealt here and defines the objectives.

Chapter 2: The general background and overview of Si is summarized in chapter 2 along with its basic properties and how it is affected by various perturbations. Other relevant theoretical backgrounds, helpful in explaining the results, are also included here.

Chapter 3: This chapter summarizes the experimental methods used to fabricate and characterize Si NSs. Recipe for sample preparation using MIE and details of all the samples used for investigations are also listed here. Model and make of all the characterization tools and their working principle is also provided here for a quick reference.

Chapter 4: The surface morphology of Si NSs prepared by MIE have been reported here explaining the mechanism for the reported morphologies for a given fabrication parameter and condition. This chapter reports the effect of wafers' doping density and other etching parameters on the resultant morphology. Observed fractal nature of porous Si along with explanation is also provided here.

Chapter 5: This chapter comprises the step by step formulism of asymmetric Raman line shape from semiconductor NSs. Phonon confinement effect and their consequences in terms of Raman line-shape for Si NSs is studied here. Phase identification, estimation of size & dimensionality of confinement has been investigated within the framework of phonon confinement model.

Chapter 6: This chapter presents the investigation of electron-phonon (Fano) interaction in heavily doped Si NSs. Interplay between phonon confinement and Fano effect in Si Nanowires is also studied here. The Fano resonance have been observed in the low frequency Raman scattering and named as Fano scattering. This chapter also explains the application of Fano scattering in extracting various subtle information

Chapter 1

about the processes taking place at microscopic level.

Chapter 7: This chapter discusses the carrier dynamics in SiNWs and its optoelectronic properties. Quantum confinement effect in SiNWs samples by means of band gap tailoring is also studied here by diffuse reflectance spectroscopy. Visible PL and its origin in Si NSs is discussed too.

Chapter 8: All the conclusions deduced from the results reported in above chapters are listed here. This chapter also discusses possible future scope of work that can be carried out for further development in this field.

Chapter 2

General Overview and Theoretical Background

2.1 Overview of Si

Silicon [100], the second most abundant element (after oxygen) in the earth's crust, making up 25.7% of the crust by mass, is the backbone for electronics and IC technology. It is most commonly found in nature as Si dioxide (SiO_2). Pure Si is a rigid and dark grey solid with a metallic lustre. It holds a crystalline structure same as that of diamond form of carbon. It shows many chemical and physical similarities with carbon. Highly purified Si, doped with elements such as boron, phosphorus and arsenic, is the basic material used in computer chips, transistors, Si diodes and various other electronic circuits. Three stable isotopes of the Si are known: ^{28}Si (92.2 %), ^{29}Si (4.7 %) and ^{30}Si (3.1 %). Other properties of Si are discussed below. General properties of Si have been given in appendix 1.

2.1.1 Crystal Structure of Si

Si is a non-metallic element which belongs to the fourth group of element in the periodic table with four electrons in its outermost shell. Each Si atom shares one of its four valence electrons in a covalent bond with each of four adjacent Si atoms. Crystal structure of Si is shown in Figure 2.1. It has diamond like structures consisting of two inter penetrating face centered cubic (FCC) lattices, displaced along the body diagonal by one-fourth of the diagonal length. It is regarded as an FCC lattice with a basis containing two identical atoms. In c-Si, each Si atom is connected to four other atoms tetrahedral. The lattice

parameter of c-Si is 0.357 nm and tetrahedral angle is 109.2° .

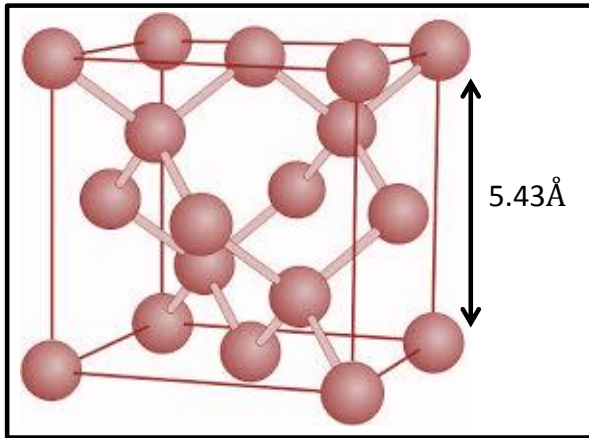


Figure 2.1: Crystal structure of Si [100].

2.1.2 Phonons in Si

The phonon dispersion curve [101–103] of c-Si is shown in Figure 2.2. Different transverse, longitudinal, acoustic, optic modes are marked as LA, LO, TA and TO in the Figure. 2.2. As it is well known that the Si is the non-polar semiconductor material due to that the frequency of LO and TO modes [104] are equal at the zone centre ($k=0$). It is evident from Figure 2.2 that, near zone edge the frequency of TA mode shows relatively flat nature as compared to other modes. It is also worth mentioning here that the energy of TA mode is comparatively lower than the LA mode. Understanding the phonon dispersion in a solid is important to understand the Raman scattering from that material and vice-versa.

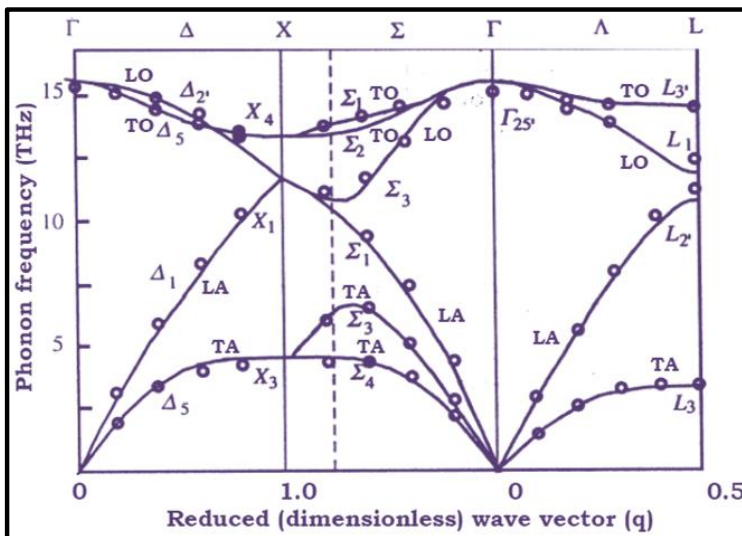


Figure 2.2: Phonon dispersion curve of Si [105].

2.1.3. Band Structure and Optical Properties of Si

It is well known that the Si is an indirect band gap solid (in bulk form). Figure 2.3 shows the energy band structure of Si reported by Cardona and Pollak [101]. It is evident from Figure 2.3 that in case of c-Si, the valence band maximum is located at the centre of the Brillouin zone and the minimum of conduction band is located at X point along the Δ direction which makes it an indirect band gap material with band gap of 1.1eV. Due to the indirect nature of band gap, c-Si cannot emit light (emission of photon when sufficient amount of energy have been incident on it) efficiently since the radiative recombination of the electron-hole pairs needs the participation of a momentum-conserving phonon, thus making the process less favourable. Unlike the other semiconductors like GaAs and InP, in which the maximum of valence band and minimum of conduction band are located at the same k point which makes it a direct band gap materials. In this case, the radiative recombination is more probable as no mediating phonon is required.

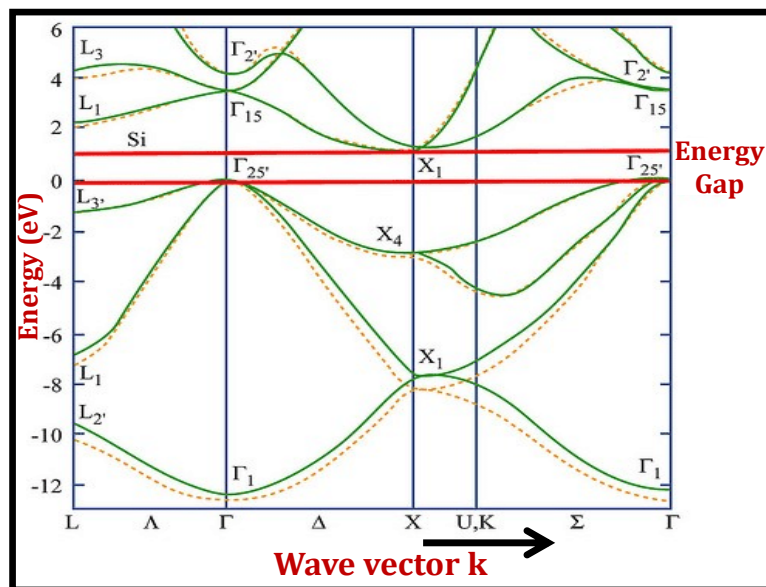


Figure 2.3: Energy band diagram of Si [101].

Figure 2.4 shows the schematic representation of direct and indirect band gap transition. It is clear from Figure 2.4 that an indirect transition involves photons and phonons both at a time. In quantum mechanics there are two different processes namely first order and

second order process. The first order process involves direct transition with no role of phonons whereas second order process involves indirect transitions where a photon must be destroyed and a phonon must be either created or destroyed.

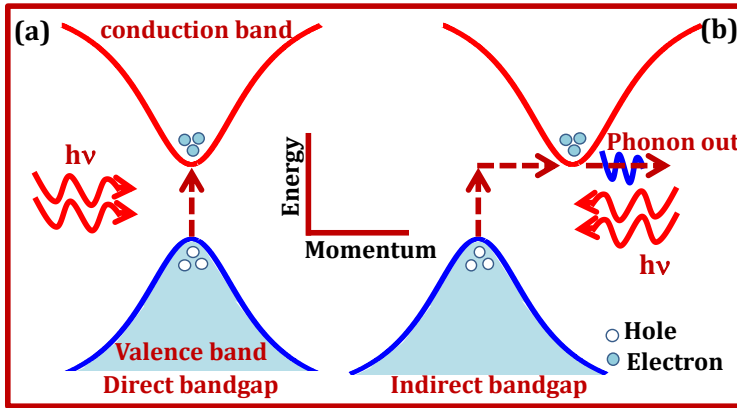


Figure 2.4: Interband transitions in (a) direct band gap and (b) indirect band gap solids. The vertical arrow represents the photon absorption while wiggly arrow represents the absorption or emission of a phonon [106].

The rate of transition of an indirect absorption is therefore much smaller than that of direct absorption. The smaller transition rate for indirect process can be clearly shown in the absorption spectrum of Si [107] in Figure 2.5. The increase in absorption is slow because of the indirect nature of band of Si which having band gap of 1.1 eV.

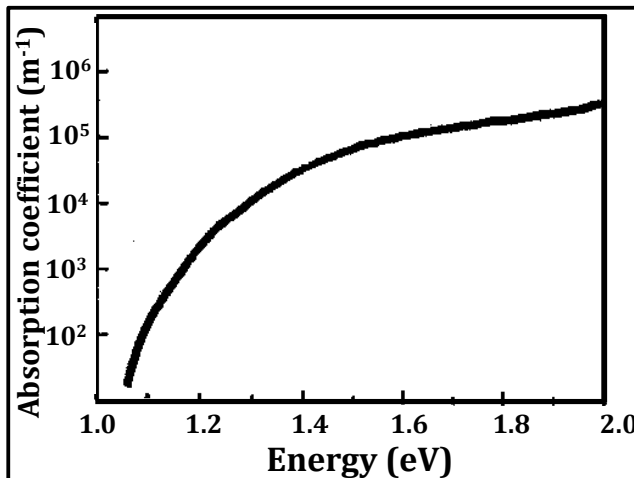


Figure 2.5: Absorption coefficient versus photon energy for Si at room temperature [107].

In addition to this, there are two distinct absorption peaks at 3.5eV and 4.3eV (Figure 2.6) present in the absorption spectra of Si when scanned in the range of 0-10 eV. The absorption coefficients in the spectral region around these two values are very large as compared to its value near band edge (1.1 eV) (as shown in the Figure 2.5). This is a significance of following two factors. Firstly, the band edge absorption is weak because it is indirect band gap material, and secondly, the density of states at the band edge is comparatively small. The measured absorption spectrum is actually dominated by direct absorption at photon energies where the density of states is very high. The 3.5eV transition energy corresponds to the minimum direct separation between the conduction and valence band near the 'L' points (i.e. $L_1 - L_3$ in the Figure 2.3). Apart from this, the separation of the conduction and valence bands adjacent to the X point is also significant. This energy corresponds to the absorption maximum at 4.3 eV. A small kink appreciated near 5.4 eV, which corresponds to the energy E_3 , near 'L' point in Figure 2.3.

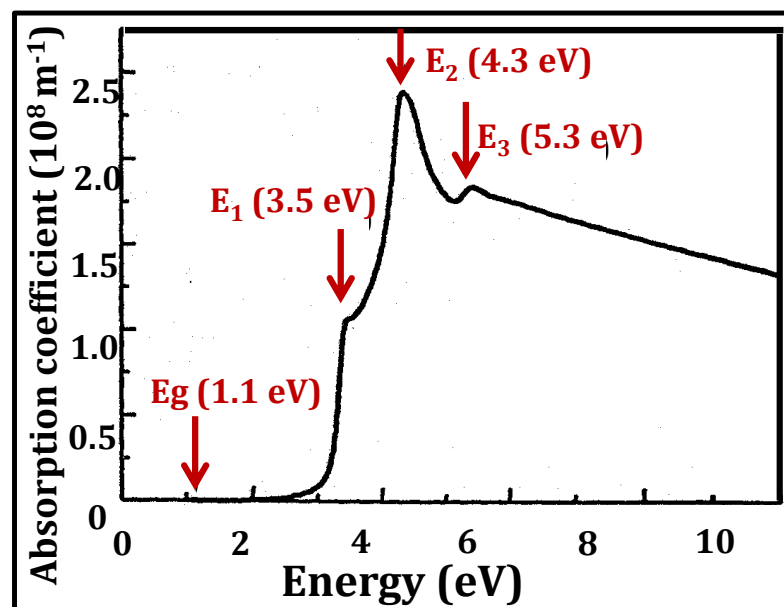


Figure 2.6: Room temperature inter band absorption spectrum of Si [106].

2.2 Low Dimensional Semiconductors and Effect of Reduced Dimensionality

When the size or dimension of a material is reduced from a large or macroscopic size to a very small size, dramatic changes in properties of these nanomaterials can be observed. In these low-dimensional systems, electronic, optical and vibrational properties are different compared to that of the bulk mainly due to the quantum size effects [106,108]. The most dramatic changes in properties take place in the structures when the carriers/phonons are confined in the region of a characteristic length which is of the order of its Bohr exciton radius.

When the confining dimension is large compared to the de Broglie wavelength of the particle, the particle behaves as free particle within confined area. As the confining dimension is decreased and reaches the order of the de Broglie wave length, the electronic and vibrational states of particle are modified due to the overlap of the wave functions reflected from the barriers. This is defined as the "*quantum confinement*" [99,108]. The effect of reduction in size of the semiconductor, known as quantum size effect, leads to confinement of electrons and phonons in one or more directions. Due to this quantum effect, the electronic and optical properties of the semiconductors can be tailored for novel device applications. Depending upon the degree of confinement, a variety of quantum structures can be fabricated with modulated properties. Some of the major properties that change with size of the low-dimensional semiconductors are discussed in following sub-sections.

2.2.1 Energy Gap Enhancement

Leading effect of reduced dimensions of the semiconductor is reflected in modification of electronic energy gap. Effective energy gap of the quantum structure is enhanced due to quantum size effect. This enhancement in energy gap can be calculated using the analogy to the problem of a particle within a suitable potential barrier. Modifications

of energy gap with confinement dimensions are given below [109,110]:

(i) Quantum dots

In case of confinement in all three spatial directions, quantum dot or quantum box structures are formed depending on their curvilinear or rectangular cross-sections, respectively. Quantum confinement effect is most pronounced in such structures. Translational motion of the carriers is constrained along all directions and the energy eigen value is given by:

$$E_{g_{eff}}^{0D} = E_g + \frac{\pi^2 \hbar^2}{2m_r} \left(\frac{1}{d_1^2} + \frac{1}{d_2^2} + \frac{1}{d_3^2} \right), \quad (2.1)$$

where d_1 , d_2 and d_3 are the confinement dimensions along x-, y- and z- directions respectively.

(ii) Quantum wires

In case of confinement along two spatial directions, the motion along the third dimension is not confined and the structure is called quantum wire. Two-dimensionally confined quantum wire structure acts as a potential well that narrowly confine electrons and holes in two directions. If the confinement dimensions are taken to be along x- and y-directions, the motion of the carriers in the z-direction remains unaffected by the potential barrier. The energy eigen value for quantum wire is given by:

$$E_{g_{eff}}^{1D} = E_g + \frac{\pi^2 \hbar^2}{2m_r} \left(\frac{1}{d_1^2} + \frac{1}{d_2^2} \right), \quad (2.2)$$

where d_1 and d_2 are the confinement dimensions along x- and y- direction, respectively ($d_3 \gg d_1, d_2$).

(iii) Quantum well

In case of confinement along one spatial direction, the structure is named as quantum wells. The motion of electrons and holes is confined in one dimension (along x direction, say) but is free to move in the other two directions (y-z directions). In these structures, the semiconductor with smaller band gap is sandwiched between larger band gap semiconductors. If thickness of the narrow gap

semiconductor layer is small enough, the energy of electrons and holes in the direction perpendicular to the interfaces is quantized. With analogy to the problem of a particle in an infinite well, the energy eigen value of the system is given by

$$E_{g_{eff}}^{2D} = E_g + \frac{\pi^2 \hbar^2}{2m_r} \left(\frac{1}{d_1^2} \right), \quad (2.3)$$

In Eq. 2.1 – 2.3, E_g is energy gap of the bulk and E_g^{eff} is energy gap due to confinement and m_r is reduced mass of electron and hole. Energy level diagram of a quantum well structure is shown in Figure 2.7.

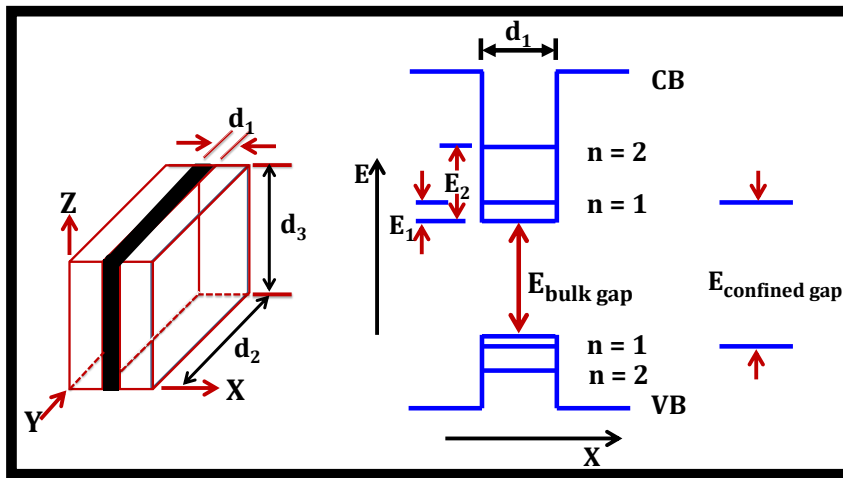


Figure 2.7: Energy level diagram of a quantum well structure.

2.2.2 Modification in the Electron Density of States

Quantum confinement of charge carriers modifies the density of states in low-dimensional semiconductors. The density of states of crystalline semiconductor is a continuous parabolic function of energy. While in the case of low-dimensional semiconductors, carriers are confined to move and the momentum vector k takes well discrete values for confined directions. This leads to density of states which are different from that of crystalline semiconductors. Density of states $g(E)$ for crystalline and low-dimensional semiconductors are given by Alivisatos *et al.* [111] as follows:

1. Crystalline semiconductor

$$g(E)_{3D}dE = \frac{1}{2\pi^2} \left(\frac{2m^*}{\hbar^2} \right)^{3/2} E^{1/2} dE, \quad (2.4)$$

where E and m^* is the energy and effective mass of electrons.

2. Quantum well structure

$$g(E)_{2D}dE = \frac{m^*}{2\hbar^2} \sum_i H(E - E_i) dE, \quad (2.5)$$

where 'i' is a quantum number used to label the discrete levels in confined direction and $H(E-E_i)$ is the Heaviside function. The $H(E-E_i)=1$ for $(E-E_i)>0$ and $H(E-E_i)=0$ for $(E-E_i)<0$.

3. Quantum wire Structure

$$g(E)_{1D}dE = \frac{1}{\pi} \left(\frac{m^*}{2\hbar^2} \right)^{1/2} \sum_i \frac{n_i H(E - E_i)}{(E - E_i)^{1/2}} dE, \quad (2.6)$$

4. Quantum dot Structure

$$g(E)_{0D}dE = \sum_i 2\delta(E - E_i) dE, \quad (2.7)$$

where $\delta(E-E_i)$ is the delta function. Figure 2.8 shows the variation of density of states with energy according to Eqs. 2.4 to 2.7. Quantum dot shows discrete spectrum of a pseudo-atom or a molecular system, ideally with vanishing width of the states and a separation similar to that found for atoms and molecules. Density of states is generally used to determine various electronic and optical properties. Since $g(E)$ varies differently in all the three cases of quantum confinement, the properties of a material can be drastically different for different degrees of confinement.

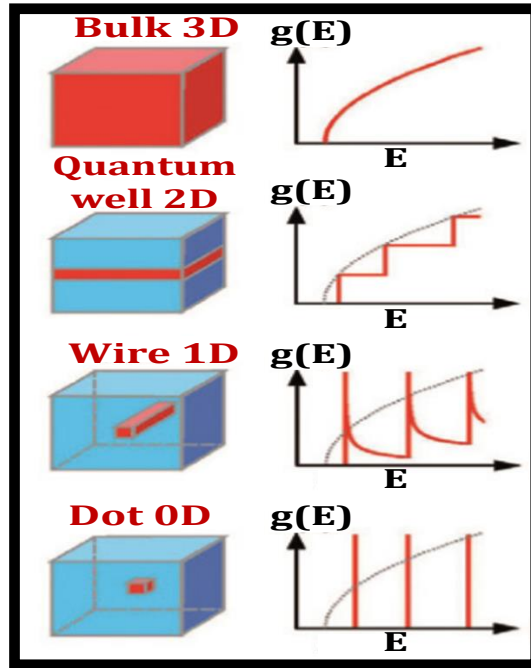


Figure 2.8: Density of states in different confinement configurations (a) bulk (b) quantum well (c) quantum wire (d) quantum dot [109].

2.3 Raman Scattering

Raman scattering is an inelastic light scattering phenomenon. When a beam of monochromatic light illuminates a gas, liquid or solid, a very small fraction of light is scattered in all directions. Scattered light consists of almost same incident frequency, known as Rayleigh scattering. Additional frequencies, known as Raman lines, are also present above and below the incident frequency [112] (possessing higher and lower energies than the energy of incident). The lines on the low frequency side of the exciting line are called ‘Stokes’ line, whereas those on the high frequency side are called ‘anti-Stokes’ lines. Observation of low and high frequency components along with the incident frequency in the scattered radiation is known as the Raman effect and this type of scattering is called Raman scattering.

2.3.1 Raman Scattering in Semiconductors

In the Raman scattering [112,113] process, a certain amount of energy is gained or lost by an incident photon having energy $\hbar\omega_i$ (incident) in order to create or annihilate elementary excitations of the solid, usually

phonons, resulting in a scattered photon of a different energy $\hbar\omega_s$ (scattered). The amount of energy transferred corresponds to the eigen energy $\hbar\omega_j$ of the elementary excitation involved. The energy conservation in first-order Raman scattering in which one phonon participate is given by

$$\hbar\omega_i = \hbar\omega_s \pm \hbar\omega_j, \quad (2.8)$$

Here the “minus” sign stands for a phonon excitation (Stokes process) while the “plus” sign implies a phonon annihilation (anti-Stokes process). The momentum $\hbar k_i$ of the vibrational excitation is related to the momentum of the incident photon $\hbar k_j$ and scattered photon $\hbar k_s$ according to momentum conservation is given by

$$\hbar k_i = \hbar k_s \pm \hbar k_j, \quad (2.9)$$

In fact, Raman interaction between photon and phonon in the semiconductor takes place through the involvement of the electronic virtual states [114] as shown in Figure 2.9. It shows Hamiltonian for electron-radiation and electron-lattice interaction as H_{E-R} and H_{E-L} , respectively. For homopolar semiconductor (e.g. Si), the electron lattice interaction is due to the excitation of phonons which perturb the periodic potential acting on the electrons by the displacement of atoms. The electronic dipole moment M produced by an electric vector of the incident light is written as [113]

$$M_\rho = \sum_{\sigma} \alpha_{\rho\sigma} E_\sigma, \quad (2.10)$$

where $\alpha_{\rho\sigma}$ is the polarizability tensor associated with electrons in the crystal. The electronic polarizability[126] can be expanded in a power series of r ,

$$\alpha_{\rho\sigma} = \alpha_{\rho\sigma}^{(0)} + \sum_{\mu} \alpha_{\rho\sigma,\mu} \cdot r_{\mu} + \sum_{\mu\nu} \alpha_{\rho\sigma,\mu\nu} \cdot r_{\mu} \cdot r_{\nu} + \dots, \quad (2.11)$$

$$\alpha_{\rho\sigma,\mu} = \left(\frac{\partial \alpha_{\rho\sigma}}{\partial r_\mu} \right)_{r=0} \quad \text{and} \quad \alpha_{\rho\sigma,\mu\nu} = \left(\frac{\partial^2 \alpha_{\rho\sigma}}{\partial r_\mu \partial r_\nu} \right)_{r=0}, \quad (2.12)$$

In Eq. 2.12, the second term is linear in r and the third term is quadratic in r which gives rise to first-order and second-order Raman scattering, respectively. Figure 2.9(a) shows the first-order Raman scattering process. For Si, the electron-lattice interaction is due to the excitation of phonons, which perturbs the periodic potential acting on the electrons by displacement of atoms. Since k_i and k_s ($\sim 105 \text{ cm}^{-1}$) are negligible in comparison to the width of the Brillouin zone ($\sim 3 \times 10^8 \text{ cm}^{-1}$), momentum conservation allows the first-order Raman scattering for the phonon frequency at $k \approx 0$ (i.e. wavelength of the phonon is very large compared to the lattice). This is known as selection rule of the first-order Raman scattering for phonons.

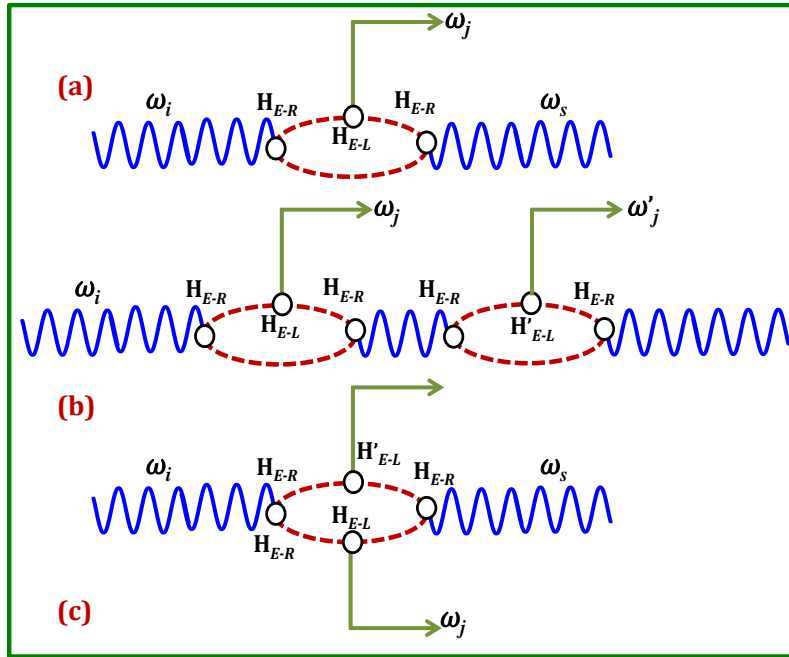


Figure 2.9: Raman scattering processes in terms of elementary interactions H_{E-L} (Electron-Lattice interaction Hamiltonian), H_{E-R} (Electron-Radiation interaction Hamiltonian), ω_i (frequency of incident photon), ω_j (frequency of vibrational excitation) and ω_s (frequency of scattered photon). (a) first-order Raman scattering process and (b), (c) shows second-order Raman scattering.

Second-order Raman scattering, in which two phonons participate, is either a line spectrum or a continuous spectrum [113]. Second-order line Raman spectrum is due to two successive first-orders Raman scattering as shown in Figure 2.9 (b) and the frequency shift is the sum or difference of Raman shifts occurring in the first-order Raman spectrum. The line nature of the second-order scattering is the result of wave-vector conservation in two successive first-order Raman scattering.

The second order continuous Raman spectrum is due to a scattering process in which a pair of phonons participates in a single event as shown in Figure 2.9 (c). Since wave-vectors of two phonons should be equal and opposite according to the conservation of wave-vectors. Therefore, the second order continuous Raman spectrum reflects a combined density of pairs of phonons with equal and opposite wave-vectors as well as the frequency dependence of the electron-lattice and electron-radiation interaction.

2.3.2 Raman Scattering in Crystalline Si

Phonon frequencies present in the c-Si can be obtained from the phonon dispersion curve shown in the Figure 2.2. Figure 2.10 shows the Raman spectrum of c-Si. c-Si has a first-order Raman active peak with Lorentzian line-shape centred at 520.5 cm^{-1} with natural line width of 4 cm^{-1} at room temperature. Second-order Raman scattering [115] is shown in Figure 2.10 in the frequency range $200\text{--}500 \text{ cm}^{-1}$ and $550\text{--}1000 \text{ cm}^{-1}$. A kink at 230 cm^{-1} and the peaks at 300 cm^{-1} and 435 cm^{-1} are associated with the second order transverse acoustic (2TA) phonons (see Figure 2.10) from the critical points at L, X and near Σ directions, respectively.

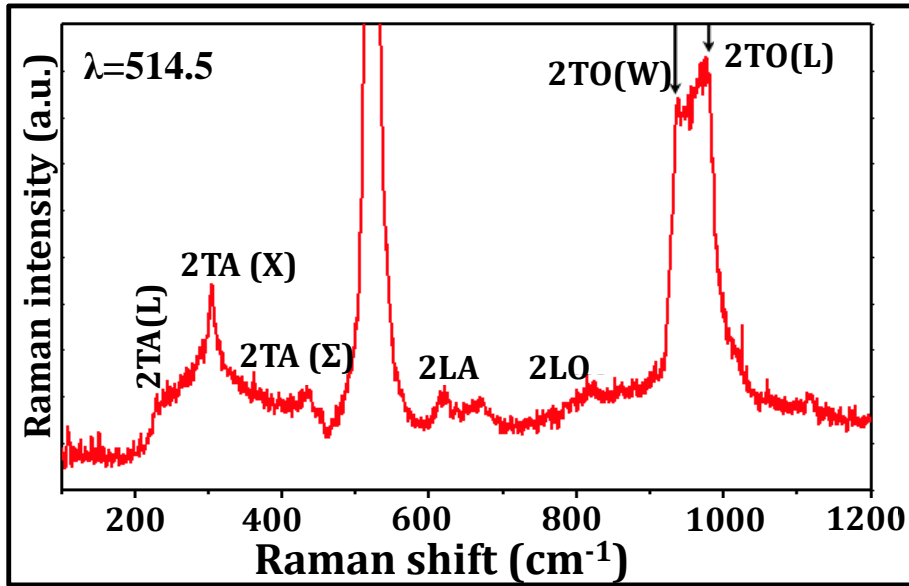


Figure 2.10: Raman spectrum of c-Si.

Weak scattering at 460 cm^{-1} is associated with Raman scattering involving phonons along and near Σ direction. The features at 610 cm^{-1} and 820 cm^{-1} in the two phonon Raman spectra are contributed by two acoustic and optic phonons in the Σ direction, respectively. Scattering in the range $900\text{--}1050\text{ cm}^{-1}$ is identified with second-order transverse optic (2TO) phonon overtones from the critical point at X, while shoulders at 940 cm^{-1} and 975 cm^{-1} are associated with 2TO phonon overtones at W and L point respectively [12–14].

2.3.3 Raman Scattering from Poly-/Nano- Crystalline Semiconductor

Raman scattering measurement is a powerful and sensitive atomic scale probe and can provide in-depth information on the structural modification caused by formation of nano crystallites and disorder on the semiconductor surface. It is an extremely useful tool for obtaining information about structural quality of a material at the atomic scale as it depends on lattice excitations. The technique is also sensitive to perturbation to electronic state of the solid. Study of Raman scattering from nanomaterials and disordered semiconductors is based on phenomenological PCM proposed by Ritcher *et al.* [91], in which the correlation length shortening leads to softening and asymmetric

broadening of first-order optical phonon modes.

In a crystalline material, the region over which the spatial correlation function extends is infinite, which leads to $k \approx 0$ momentum selection rule of first-order Raman scattering. However, in nano crystalline and disordered semiconductors, the phonons are confined to the small particle volume, resulting in relaxation of the momentum selection rule $k \approx 0$, and cause the softening and asymmetric broadening of the phonon modes in the Raman spectra. When the size of the particle is reduced to the order of nanometer, the wave function of optical phonons will no longer be a plane wave and the localization of wave function leads to a relaxation of $k \approx 0$ selection rule for first-order Raman active optical mode [16–18]. Therefore, not only the zone-centre phonons with wave vector $k \approx 0$ but also those away from the zone centre with $k > 0$ also take part in the Raman scattering process. Since the optical phonon dispersion relations in most semiconductors have negative dispersion, the Raman spectra exhibit downward shift in peak position and broadening of the peak width i.e. phonon softening of Raman active optical mode.

2.3.4 Brillouin Scattering

Raman scattering measures optical phonons because the relatively large energy transfers mean that the high frequencies, characteristic of optical phonons, are excited. However, acoustic phonons can also be excited using electromagnetic radiation with appropriate probability. The corresponding technique is called *Brillouin scattering* [116] and is based on the same process as Raman scattering and is subject to the same selection rule. In order to probe *acoustic phonons*, much smaller energy transfers need to be measured, and therefore the frequency resolution must be much higher. While Raman scattering can be carried out using an optical grating to resolve the spectrum, a Fabry-Perot interferometer is typically used in Brillouin spectrometers, i.e. the incident beam is reflected back and forth between two semi-transparent mirrors and made to interfere with itself.

Interference is constructive only if the distance between the mirrors is an integer multiple of the wavelength, effectively monochromatize the beam. The spectrum is swept by changing the mirror spacing. This provides the necessary resolution to measure frequencies, ν , up to 200GHz, characteristic of acoustic phonons. Like Raman scattering, Brillouin scattering is limited to the wave vectors close to the centre of the Brillouin zone, $k \approx 0$.

2.4 Raman Study of the Electron-Phonon Coupling in Heavily Doped n- and p-type Si

In heavily doped c-Si, Raman line-shape exhibits asymmetry and peak shift [117–120]. Such changes in the Raman line-shape can be explained with the Fano-type [121] interaction model based on a discrete continuum interaction. It was Ugo Fano [121], who suggested the first theoretical explanation of observed asymmetric profiles in some of the Rydberg spectral atomic lines and proposed a formula (also known as the Beutler-Fano formula) that predicts the shape of spectral lines based on a superposition principle of quantum mechanics.

Fano's interpretation of these “strange line-shapes” of spectral absorption lines is based on the interaction of a discrete excited state of an atom with a continuum sharing the same energy level which results in an interference phenomenon. The resulting line shape is produced by the interference between the discrete and continuum states. Using this model, the observed Raman line-shape of heavily doped c-Si has been explained as a result of electron-phonon (e-ph) interaction i.e. the interference between the discrete phonon state and continuum of electronic states present due to heavy doping. When doping in Si is of the order of 10^{19} cm^{-3} , the semiconductor behaves like a degenerate semiconductor.

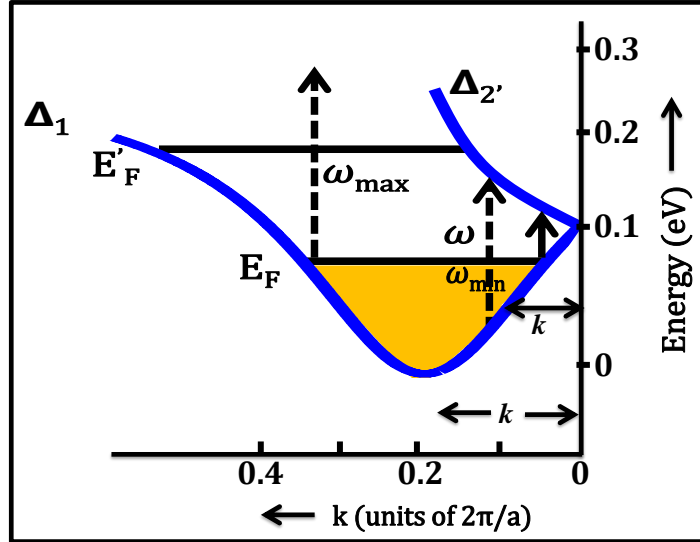


Figure 2.11: Conduction bands of heavily doped n-type c-Si [89].

Position of the Fermi level goes deep inside the conduction band as shown in Figure 2.11. This gives rise to continuous electronic Raman scattering due to inter-band transitions between the Δ_1 and Δ_2 bands along (100) directions [97,120,122]. A continuum of transitions exists from a minimum energy $\hbar\omega_{\min}$ to a maximum energy $\hbar\omega_{\max}$ determined by the Fermi level E_F as shown in Figure 2.11. If, energy $\hbar\omega_0$ of a discrete optical phonon state, which has the same symmetry as the inter-band transitions, falls within the continuum, interference between a discrete state and the continuum, takes place [97,120], i.e.

$$\hbar\omega_{\min} < \hbar\omega_0 < \hbar\omega_{\max}, \quad (2.13)$$

when this condition is satisfied, the zone-centre phonon mode in the Raman spectrum of heavily doped c-Si leads to asymmetric line shapes. Raman line-shape in the presence of Fano interference is expressed by

$$I_F(\omega) = \frac{(q+\varepsilon)^2}{1+\varepsilon^2}, \quad (2.14)$$

where $\varepsilon = \frac{\omega-\omega_0}{\gamma/2}$; γ and ω_0 being FWHM, and observed wavenumber-

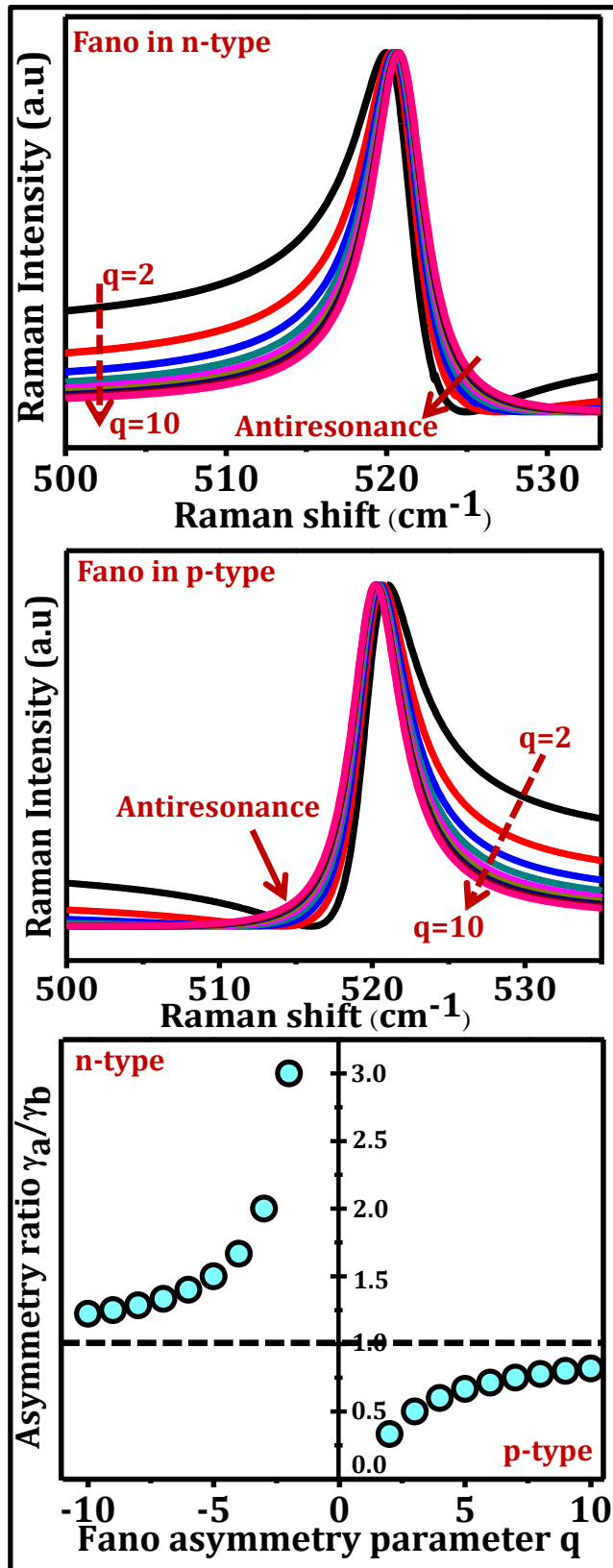


Figure 2.12: Raman lineshape for different value of q (n-type) for negative q values (p-type) for positive q values and bottom panel shows asymmetry ratio for positive and negative q value.

of Fano transition respectively (reflected as peak position in Raman-Fano line-shape). Here the quantity 'q' is known as Fano asymmetry parameter which measures the extent of Fano interference. Smaller value of 'q' means strong e-ph interaction. The presence of Fano effect will result in increased half width in the pre-maximum side and post-maximum side for heavily doped n- type and p-type Si respectively. Figure 2.12 shows the calculated Raman line shape for n- and p-type semiconductor and bottom panel shows the asymmetry ratio for positive and negative q value for p- and n-type Si.

2.5 Raman Spectrum of Amorphous Si

As discussed above, first-order Raman spectrum of the c-Si is a measure of the phonon frequency in the vicinity of $k=0$. Other phonons with nonzero k values are Raman forbidden as a result of the translational symmetry. However, these phonons can be observed as two phonon processes in the second-order Raman spectrum. In this case only the sum of the k values of the two phonons must be vanishingly small and the whole Brillouin zone contributes to the second-order Raman spectrum [115,123,124]. In the a -Si, the translational invariance is broken due to lack of long-range order. As a result, the k conservation selection rule breaks down and all phonon modes become first-order Raman allowed [124,125]. The tetrahedral short-range order is preserved in a -Si.

Thus the density of vibrational states of these materials is simply a broadened version of that of their amorphous counterparts. First-order Raman spectrum of a -Si reflects the DOS modulated by transition matrix elements and statistical factors [126]. Raman study by Wihl *et al.* [127] also establishes that the short-range order remaining in the a -Si material suffices to preserve the main features of the phonon density of states of the corresponding crystalline material. This type of finding is also mentioned by Smith *et al.* [128] in their study. Thomsen and Bustarret *et al.* [129] studied the gradual change in the Raman spectra

of Si when a crystal is damaged and is transformed into the amorphous form.

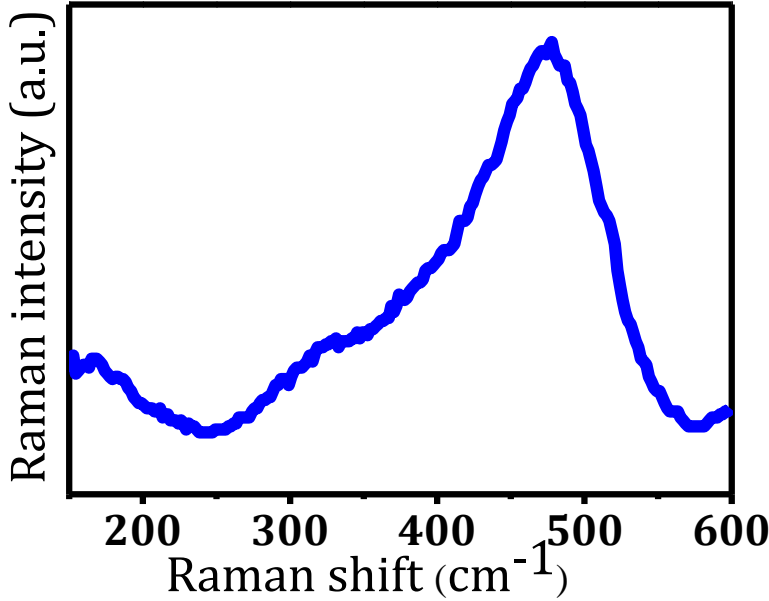


Figure 2.13: Raman spectrum of *a*-Si.

Different theories are presented for the observed Raman spectrum from the *a*-Si [130–133]. As mentioned in the above paragraph, disorder in the *a*-Si relaxes the Raman selection rule for $k=0$, which allows first-order Raman scattering by phonons of larger k values. The maximum value of k of the participating phonon is of the order of $1/\Lambda_j$ [124], where Λ_j is the coherence length of the normal mode ‘j’. Room temperature Raman spectrum of the *a*-Si is shown in the Figure 2.13 Shuker and Gammon *et al.* [134] attempted to quantify the Raman scattering from *a*-Si. Their analysis was based on following assumptions: (i) the vibrations are harmonic so that they can be analyzed into normal modes and (ii) the vibrations couple to light through the displacement dependence of the electronic polarizability of the material. Following line-shape of the *a*-Si was proposed:

$$I(\omega) = \sum_b C_b \left(\frac{1}{\omega}\right) [1 + n(\omega)]g(\omega), \quad (2.15)$$

where $n(\omega) = \left[\frac{\hbar\omega}{k_\beta T} - 1\right]^{-1}$, k_β is the Boltzmann constant and $g(\omega)$ is the phonon DOS function. The C_b represents the coupling of different vibration bands to the radiation. It also contains the

polarization dependence of Raman scattering from the α -Si. If all vibrational modes in a given band couple equally to the incident light, Eq.2.15 can be used to obtain $g(\omega)$ from the Raman spectrum reduced by the term $[n(\omega) + 1]/\omega$. This technique shows that Raman scattering in the amorphous solids can be used to obtain a semi quantitative picture of the phonon DOSs of the crystalline solids. A complete quantification of short-range order in α -Si is still not available and should be done which can be helpful in technological advancement and Raman scattering may prove to be a good tools for this quantification.

2.6 Photoluminescence

Photoluminescence is the spontaneous emission of light from a material under optical excitation. PL spectroscopy is an extremely sensitive and non-destructive method of probing the electronic structure of materials. Intensity and spectral content of this PL is a direct measure of various important material properties. In PL spectroscopy, photons are absorbed from an excitation source such as laser or lamp, which injects electrons into the conduction band and holes into the valence band. The electrons are initially created in higher electronic states in the conduction band and lose energy by emitting photons. In the case of photo-excitation, these electrons return to valence band resulting luminescence of lower frequency. This luminescence is called PL.

2.6.1. Photoluminescence from Si Nanostructures

Visible PL has been observed from Si NSs [22–24,26] unlike bulk Si, which has indirect bandgap corresponding to infrared region. Visible PL from Si NSs can be explained using uncertainty principle and zone folding as discussed below. When the electron is localized, its momentum becomes uncertain according to the Heisenberg Uncertainty Principle. This phenomenon may offer a solution to indirect bandgap of Si. The uncertainty principle, $\Delta p \cdot \Delta x \approx \hbar$ or $\Delta k \cdot \Delta x \approx 1$, where Δx and Δk are the uncertainties in the position and

wave vector, respectively. In c-Si, Δx is infinity due to its translational symmetry. Thus only transitions of electrons with $\Delta k = 0$ is allowed by the uncertainty principle. In a NS of size ' L ', the uncertainty in position is ' L ' which brings an uncertainty of $1/L$ in the momentum (i.e. $\Delta k \sim 1/L$). All the transitions are allowed when Δk lies in the range of $1/L$. Therefore, optical recombination is possible in appropriately low dimensional materials. As a consequence, it can be said that the band gap is effectively a direct type in nature for optical transitions to take place. However, to find the exact up-shift and its dependence on the confinement dimensions, rigorous band structure calculations have been primarily done for idealized Si quantum wire and dot structures using semi-empirical [135,136] and first-principles calculations [28–30].

Using the effective mass theory, some authors [137,138] have explained that the fundamental indirect band gap in Si is expected to behave like a direct band gap at the Brillouin-zone centre. A concept of zone folding has also been used to explain the coupling between the conduction band minima and the valence band maxima [138,139]. In bulk Si, the indirect conduction band has six minima positioned at $\pm (0, 0, 0.85) 2\pi/a_0$, $\pm (0, 0.85, 0) 2\pi/a_0$ and $\pm (0.85, 0, 0) 2\pi/a_0$, where the zone boundary is at $2\pi/a_0$ and a_0 ($\sim 5.43 \text{ \AA}$) is the lattice constant. These minima are anisotropic ellipsoids with two light transverse electronic masses, $m_T = 0.19$ and one heavy longitudinal electronic mass, $m_L = 0.92$.

These minima are up-shifted in energy by a large amount in the confinement plane and less amount in other directions. The concept of zone folding rests with an increase in the coupling of conduction band minima near the zone boundary and the valence band maxima at the zone centre. This is done conceptually by repeated folding of the Brillouin-zone itself in submultiples. This defines the new reduced zone boundary about which the conduction band is folded to the zone centre and making the direct bandgap. Different theories, which explain the visible PL from Si NSs at room temperature, are available

in the literature to calculate analytically the exact up-shift and its dependence on the confinement dimensions. Most of the reported work on visible PL correlates this phenomenon due to quantum confinement effect [140–142]. Other proposed models attribute this PL due to oxide related interfacial defect states and surface states [143–145].

Chapter 3

Experimental Methodology and Sample Details

Experimental details, including various characterization techniques used, and methodology adopted for the research work is discussed in the current chapter. The sample preparation technique and details of all the samples under investigation has also been provided in the current chapter.

3.1 Sample Preparation

Most of the samples containing Si NSs used in the present study have been fabricated using metal induced etching (MIE). For some studies, Si NSs have been prepared using laser induced chemical etching (LIE) techniques also. Details of the methods and recipe used are as follows.

3.1.1 Metal Induced Etching Method

Amongst various techniques of nanomaterial fabrication, including CVD, PVD, MBE, MIE [32,146,147] is one of the simplest and economic methods. MIE is a two-step method in which, first metal nanoparticles (MNPs), mainly silver (Ag) or gold (Au), are deposited on a clean semiconductor surface usually by dipping the wafer in a solution containing appropriate metal salt dissolved in acid. Size and distribution of metal NPs deposited on the wafer depends on concentration of the solution and deposition time.

After the metal deposition step (or pre-porosification step), wafers (containing metal NPs) are transferred into etching solution for porosification. A typical etching solution for this purpose consists of hydrofluoric acid (HF) and hydrogen peroxide (H_2O_2). After a particular time of etching, porous Si/Si NSs get fabricated on the semiconductor surface. In this method, the materials and chemicals used are Si wafer, HF, $AgNO_3$, $KAuCl_4$, H_2O_2 , distilled water (DI) and HNO_3 . The steps involved in sample preparation are discussed below.

Si wafer cutting and superficial cleaning: The n- and p-type Si wafers of required dimensions were cut using a diamond tip glasscutter. Since the surficial cleaning of Si substrates is critical for sample fabrication, these were cleaned to remove inorganic impurities present on the surface using the ultrasonic bath. Substrates were subsequently cleaned in acetone and iso-propanol (IPA) for 10 minutes each followed by washing with DI water.

Surface treatment: The Si wafer were further washed with 5% HF solution to remove the thin oxide layer formed on the surface of Si wafer due to exposure to air and then with DI water to remove unnecessary fluoride ions attached on the surface of the Si wafer.

Metal Deposition: These wafers were then dipped in solution

containing 4.8M HF and 5mM AgNO₃ and KAuCl₄ for required deposition time to deposit Ag nanoparticles (AgNPs) and Au nanoparticles (AuNPs) respectively and then rinsed with distilled water. The deposition of MNPs plays an important role to determine the diameter of Si nano wires (Si NWs).

Etching process: The MNPs (AgNPs/AuNPs) deposited Si wafer is then kept for etching in an etching solution containing 4.6M HF and 0.5M H₂O₂. Etching time decides the length of the SiNWs with a direct proportionality between the two.

Removal of Ag- & Au-NPs: The etched Si wafer (SiNWs) is dipped in the HNO₃ acid for two min to remove the MNPs present inside the pores. The strong oxide layer is formed on the surface of SiNWs after the treatment of HNO₃ acid. In order to remove the oxide layer from the surface of SiNWs, samples were transferred to the HF solution and then washed with DI water. Figure 3.1 displayed the schematic diagram of steps involved in the MIE technique.

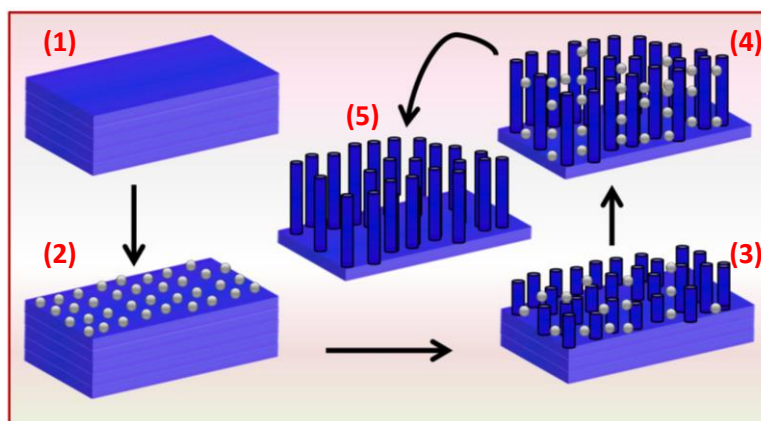


Figure 3.1: Schematic diagram of step by step formation of SiNWs. (1) cleaned Si wafer, (2) MNPs deposited Si wafer, (3) etched Si wafer, (4) increase etching time and (5) SiNWs after removal of MNPs.

3.1.2 Laser Induced Etching Method

In LIE, the cleaned Si wafer is placed inside the HF acid kept in a plastic or Teflon beaker and then laser beam was focused on this wafer using a convex lens with the sample kept at the focal point of the lens which was 15 cm in the present case. The LIE experimental set up used

for sample- preparation is shown in the Figure 3.2. The wafer has been kept on a Teflon beaker in such a way that the wafer dips fully in the HF acid. The level of HF acid was not very high above the Si wafer as it may cause beam refraction and attenuation of the laser beam [148,149]. As the reaction between HF acid and Si atoms takes place, the Si atoms are removed from the wafer surface and it forms porous Si. The Si NSs are formed inside the pores [78].

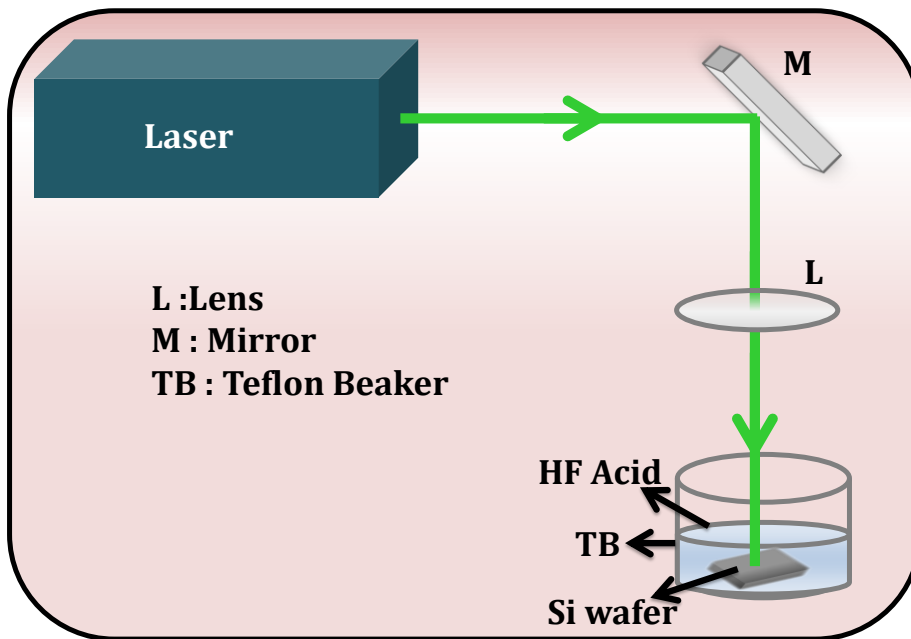


Figure 3.2: Experimental set up for the laser induced etching.

Sample description: Various samples were fabricated to carry out research work presented in this thesis. Some samples were prepared using MIE technique, listed in Table 3.1, which were used to study the mechanism of MIE and formation of different morphology as a result of MIE using AgNPs. Effect of AuNPs on the etching & resulting morphology has also been studied and the sample prepared using gold (by MIE) has been listed in Table 3.2. A set of samples, which were prepared by LIE, were used for study of low frequency Raman scattering and the same has been listed in Table 3.3. In addition to these, Raman scattering from *a*-Si has been analysed and a model has been proposed for quantification of short-range order. This study was

done on Raman data reported in literature [150]. For ease of discussion, these samples have been listed in Table 3.4.

Table 3.1: List of Si NSs samples prepared by the MIE using AgNPs

Sample Name	Starting wafer Type and (resistivity in Ω -cm)	AgNPs deposition time (minutes)	Etching time (minutes)
N_{Ag}^{*1}	n-type (0.01)	1	00
$N_{Ag}^{\#1}$	n-type (0.001)	1	00
P_{Ag}^{*2}	p-type (0.01)	1	00
$P_{Ag}^{\#2}$	p-type (0.001)	1	00
N^{*3}	n-type (0.01)	1	60
$N^{\#3}$	n-type (0.001)	1	60
$N^{\$}$	n-type (1000)	1	60
P^{*4}	p-type (0.01)	1	60
$P^{\#4}$	p-type (0.001)	1	60
$N_{Ag}^{\#\#5}$	n-type (0.001)	60	00
$P_{Ag}^{\#\#5}$	p-type (0.001)	60	00
$N^{\#\#\#6}$	n-type (0.001)	60	60
$P^{\#\#\#6}$	p-type (0.001)	60	60
c-Si-N	n-type (0.001)	00	00
c-Si-P	p-type (0.001)	00	00
c-Si	bare Si wafer	00	00

Table 3.2:List of Si NSs samples prepared by the MIE using AuNPs

Sample Name	Starting wafer Type and (resistivity in Ω -cm)	AuNPs deposition time (s)	Etching time (minutes)
N_{Au}^{#''''}	n-type (0.001)	60	00
P_{Au}^{#''''}	p-type (0.001)	60	00
N^{#''''}	n-type (0.001)	60	60
P^{#''''}	p-type (0.001)	60	60

Table 3.3:List of Si NSs samples prepared by the LIE using Argon ion laser (514.5nm)

Sample Name	Starting wafer Type and (resistivity in Ω -cm)	Laser power density (kW/cm ²)	Etching time (minutes)
N25	n-type (~5)	1.76	25
N45	n-type (~5)	1.76	45
N60	n-type (~5)	1.76	60

Table 3.4:List of amorphous Si samples.

Sample Name	Raman spectra taken from ref. and fabricated using ion implantation
AS1	Al-Salman R. <i>et al</i> [184]
AS2	Lopez T. <i>et al.</i>[183]
AS3	Kumar <i>et al.</i> [150]

3.2 Instruments' Details

3.2.1 Scanning Electron Microscope

Scanning electron microscopy (SEM) is a noncontact, non-destructive technique for imaging surfaces to understand the morphology. Figure 3.3 displays the schematic diagram of SEM. The SEM employs a focused beam of high-energy (which typically has an energy ranging from 0.2 keV to 50 keV). These electrons, with significant amounts of kinetic energy, generate a range of signals on interaction with the surface of specimens. The signals that are obtained from the electron-sample interactions reveal information about the sample's surface.

3.2.1.1 Signals Generated

Electron-matter interaction leads to emission of secondary electrons (SEs), backscattered electrons (BSEs), Auger electrons, X-rays, etc. In case of SEM, the interaction products most frequently used for the generation of images are (i) SEs and (ii) BSEs.

Secondary electrons (SE)

When the incident electron beam hits the specimen, secondary electrons are produced from the emission of the valence electrons of the constituent atoms in the specimen. Since the energy of secondary electrons is very small generally less than 50 keV SEs are extremely abundant and the SE yield (the number emitted per primary electron), is dependent on the accelerating voltage.

Backscattered electrons (BSE):

All electrons having energies higher than 50 keV are BSE and are generated by elastic scattering and BSE yield depends on atomic number Z , so information from a relatively deep region is contained in the backscattered electrons. The BSE are sensitive to the composition of the specimen.

X-Rays: When electrons in the inner shells are excited, X-rays are generated whose energies correspond to the energy difference between the shells involved in this transition. The generated X-rays are basically used for elemental analysis in SEM.

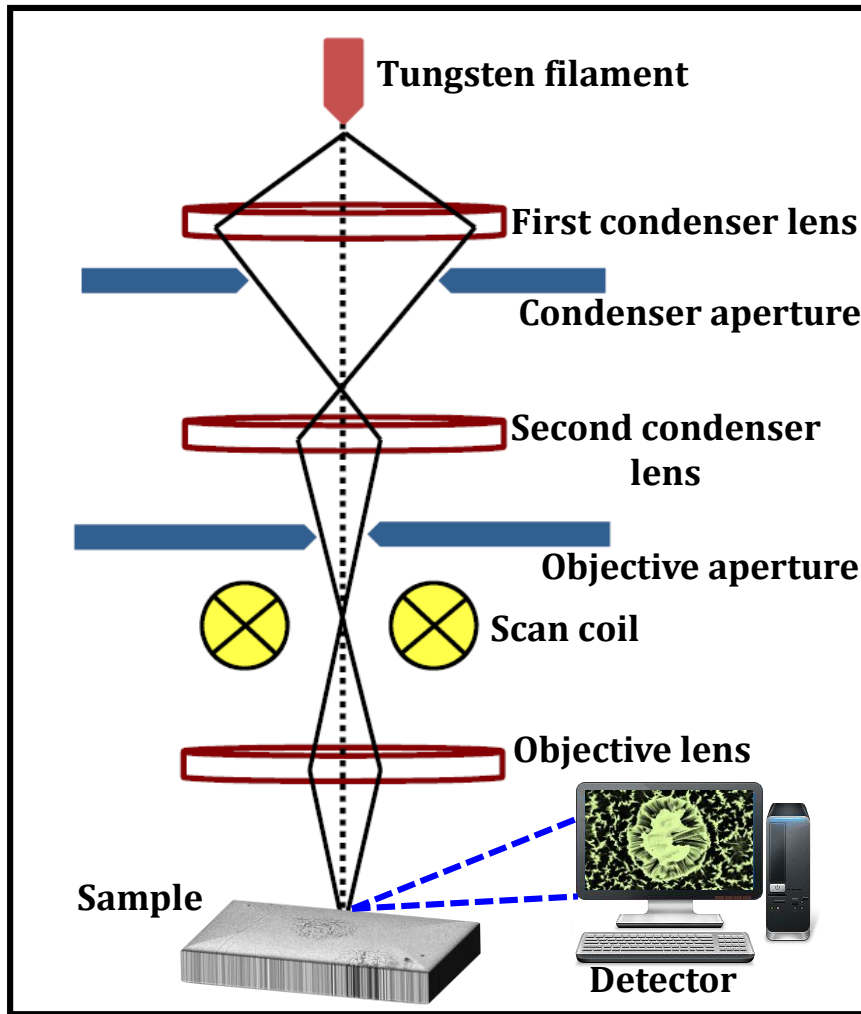


Figure 3.3: Schematic diagram of SEM.

3.2.1.2 Imaging in SEM: The interaction of e-beam with sample does not occur at a point but throughout the volume, these sizes of volume depend on beam energy and shape of interaction volume and atomic number.

Components of the instrument: The SEM requires an electron probe, a specimen stage to place the specimen, a secondary-electron detector to collect secondary electrons, an image display unit, and an operation system to perform various operations.

i) Electron source: The illumination system of SEM consists of an electron source, which is maintained at a negative potential. The emitted electron beam, which typically has an energy ranging from a few hundred eV to 50 keV, is passed through a magnetic lens system.

ii) Condenser Lens and Objective Lens: Placing a lens below the

electron gun enables to adjust the diameter of the electron beam. Two-stage lenses are located below the electron gun. The objective is a very important lens that determines the final diameter of the electron probe up to 5 to 10 nm.

iii) Detector: A scintillator is coated on the tip of the detector and a high voltage of about 10 kV is applied to it. The secondary electrons hit the scintillator and generate the light signal. This light is directed to a photo-multiplier tube PMT and amplified, then transferred to the display unit. Since the scanning on the display unit is synchronized with the electron-probe scan, brightness variation, which depends on the number of the secondary electrons thus forming an SEM image. A cathode-ray tube (CRT) or liquid-crystal display (LCD) is used as a display unit. In this work SEM images were recorded using Supra55 Zeiss, oxford instruments.

3.2.2 Transmission Electron Microscope

Transmission electron microscopy (TEM) is used to study the local structures, morphology, dispersion of multicomponent polymers, cross sections and crystallization of metallic alloys, semiconductor's micro, nano and angstrom-structure of composite materials etc. Figure 3.4 shows the schematic diagram of TEM. In this technique, a beam of high energy electrons (typically 100–400 keV) is collimated by magnetic lenses and allowed to pass through a specimen in very high vacuum. The transmitted beam and a number of diffracted beams can form a resultant diffraction pattern, which is imaged on a fluorescent screen kept below the specimen. The diffraction pattern gives the information regarding lattice spacing and symmetry of the structure under consideration. Alternatively, either the transmitted beam or the diffracted beams forms a magnified image of the sample on the screen as bright-and dark field imaging manners respectively. This gives information about the size and shape of the micro, nano and angstrom-structural constituents of the samples. High resolution image contains information about the atomic structure of the material. This can be

obtained by recombining the transmitted beam and diffracted beams together [151,152].

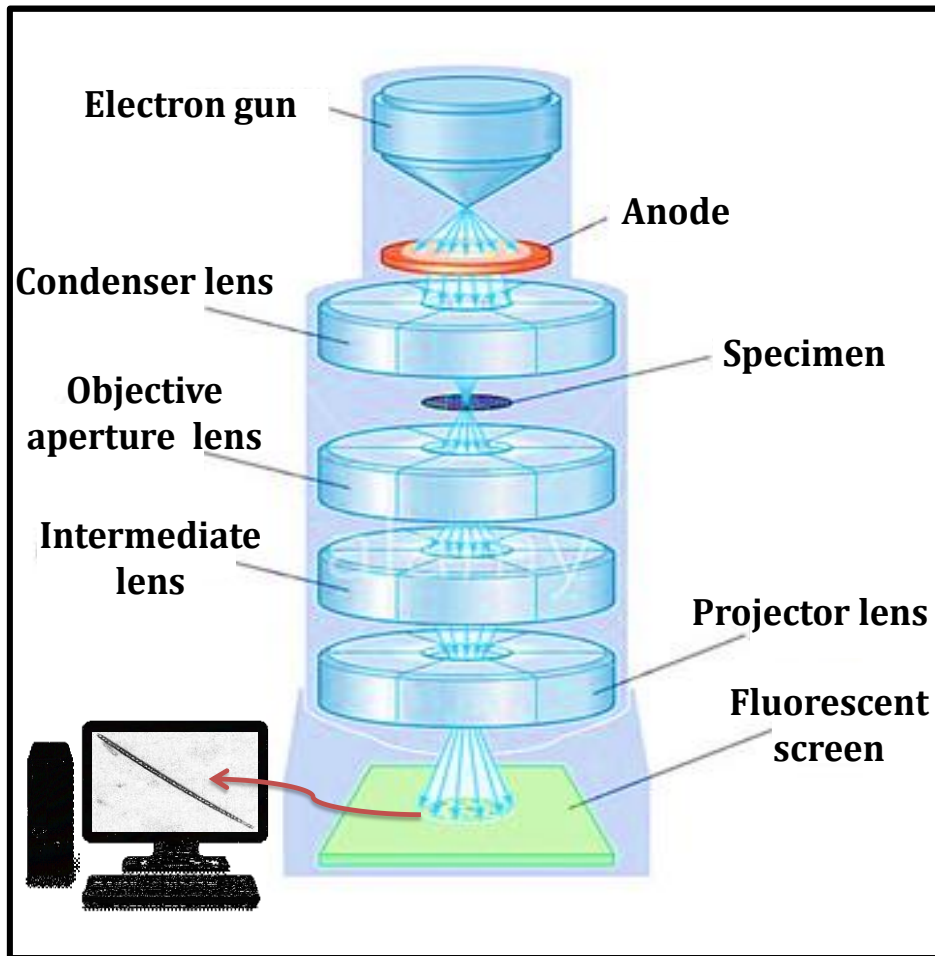


Figure 3.4: Schematic diagram of TEM [152].

3.3 Raman Spectroscopy

Raman scattering [112,153], after its discovery, has now been established as one of the versatile spectroscopic tools widely used, not only to study crystal structure, chemical composition, crystal defects but also to investigate different physical phenomena taking place at microscopic levels like confinement, chemical compositions, defect states etc. Whether the objective is qualitative or quantitative, Raman spectroscopy can provide key information, easily and quickly, specifying the chemical composition and the structure of the probed material. The Raman spectroscopy is used to observe vibrational, rotational and other low frequency modes in the samples under investigation. It relies on inelastic scattering or Raman scattering of

monochromatic light, usually from a laser in the visible, near infrared or near ultraviolet range. The schematic of experimental set-up of a Raman spectrometer is shown in Figure 3.5.

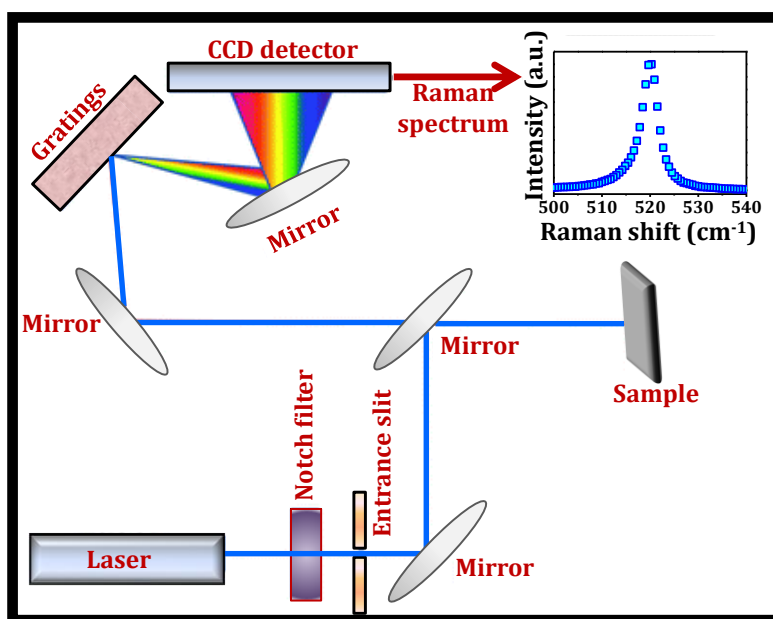


Figure 3.5: Schematic diagram of Raman Spectrometer

The laser light interacts with molecular vibrations, phonons or other excitations in the system, resulting in the energy of the laser photons being shifted towards lower values of energy. The shift in energy gives information about the vibrational modes in the system [11,12,154]. In the Raman scattering, a sample is illuminated with a laser beam. Electromagnetic radiation from the illuminated spot is collected with a lens and passed through a monochromator. Elastically scattered radiation at the wavelength corresponding to the laser line (Rayleigh scattering) is filtered out, while the rest of the collected light is dispersed onto a detector. The scattered light is analysed to see the components available in the signal. In order to record the light intensity as a function of energy (in wavenumber units), a charge-coupled device (CCD) detector is used. In this work Horiba LabRAM HR micro Raman spectrometer was used for recording the Raman signals of Si NSs. The low frequency Raman spectra have been recorded using Horiba JY T64000 spectrometer.

3.4 Diffuse Reflectance Spectroscopy

When electromagnetic radiation (light), in the UV-Visible region, interacts with matter, various effects can be observed such as reflection, scattering, absorption, transmission and fluorescence/phosphorescence. Total potential energy of a molecule can be represented as the sum of its electronic, rotational and vibrational energies. When energy of incident light is equal to the energy required to excite an electron from a lower energy level to higher level, the light is absorbed. UV-Vis spectroscopy deals with how the electromagnetic radiation is, absorbed, transmitted and reflected by/through a material. The block diagram of a typical UV-Vis spectrophotometer is shown in Figure 3.6.

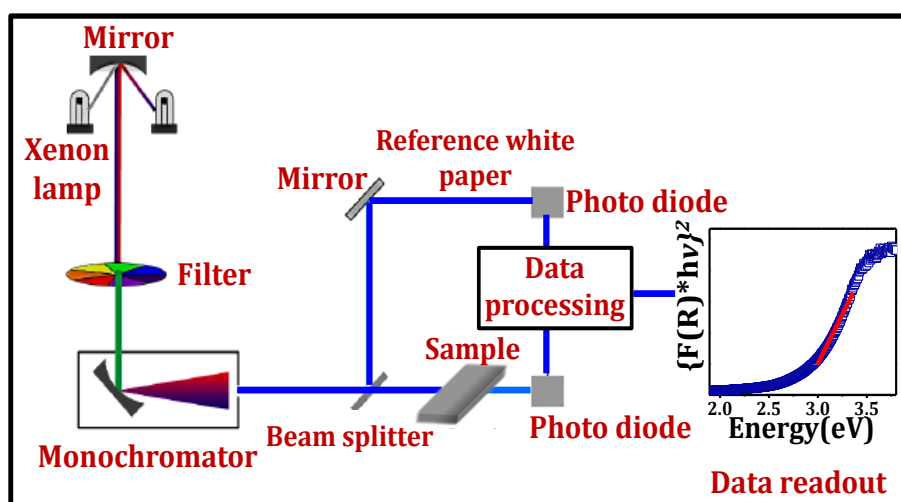


Figure 3.6: Experimental set-up for UV-Vis diffuse reflectance spectroscopy.

Working principle

The amount of light absorbed is decided by the ratio of incident radiation (I_0) and the reflected or transmitted radiation (I). Quantitatively absorbance is described by following equation:

$$A = -\log\left(\frac{I_0}{I}\right), \quad (3.1)$$

where, A is absorbance, I_0 and I are the intensities of incident and transmitted light respectively at a given wavelength. A UV-Vis

spectrophotometer uses a tungsten-halogen or deuterium lamp as a source. A dispersion device like a monochromator is used to select the incident wavelength. A detector, which converts UV- visible light into electrical signal is the final component of the spectrophotometer. It is easy to estimate band gap (E_g) from absorption spectra, in case of solid films of known low thickness, due to low scattering properties. However, in colloidal samples, due to large surface area exposure scattering is enhanced. As dispersed light does not reach up to the detector it is counted as absorbed light. Figure 3.7(a) shows the photograph of UV-Vis setup used in the current study. UV-Vis spectra from opaque materials like porous Si/ Si NSs are recorded by directly putting the sample below the target plate shown in Figure 3.7(b).



Figure 3.7: Experimental set up for diffuse reflectance measurement (a) Carry 60 UV-Vis spectrometer, (b) an integrating sphere attachment to detect diffuse reflectance.

Diffuse reflectance spectroscopy (DRS) enables one to obtain E_g of opaque samples [61,155]. The estimation of E_g using DRS utilizes Kubelka & Munk model [156], in which diffuse reflectance R is related to Kubelka–Munk function $F(R)$ by following equation:

$$F(R) = \frac{(1-R)^2}{2R}, \quad (3.2)$$

where, R denotes the percentage reflectance from the sample. If $h\nu$ is the energy of photon, a graph between $[F(R).h\nu]^2$ versus $h\nu$ (in eV) can provide the E_g values of a sample with direct bandgap. An indirect

bandgap can be obtained from a plot of $[F(R).hv]^{1/2}$ versus hv [157,158]. A UV-Vis spectrometer model Carry 60 of Agilent make has been used in the current work.

3.5 Photoluminescence Spectroscopy

To investigate the emission characteristic of Si NSs, PL measurements were performed using a Dongwoo Optron PL system with an He-Cd laser and diode laser, which having choice of excitation wavelength of 325 nm or 405 nm respectively. The PL setup has been developed on the optical table using the combination of lens and mirror assembly. Figure 3.8 shows the schematic picture of setup developed for PL measurement using 405 nm diode laser. The laser beam coming from laser source has been directed with the help of mirrors and focused on the sample using the lens (L). The emission of light from sample is collected using lens assembly and focus on the optical fiber based Spectrograph. The final signal has been recorded using spectrograph which is connected with the computer. All measurements have been done at room temperature as well as down to 11 K. The schematic of the PL measurement setup is shown in Figure 3.8. The output of a laser light source (405 nm) is passed through the excitation slit and sample is placed in the path of the monochromatic light with an angle close to 45° .

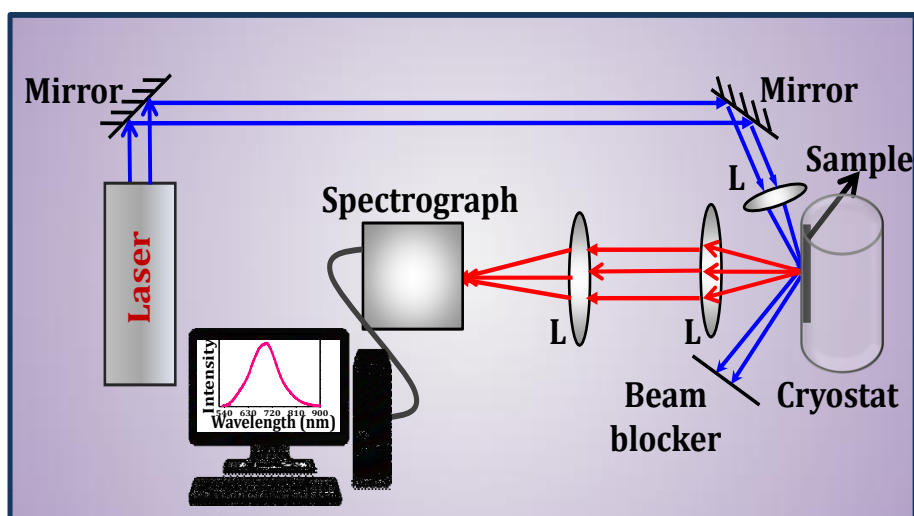


Figure 3.8: Schematic diagram of PL setup

While placing the sample, it is important not to send the reflected excitation light directly to the emission slit. When the sample is

optically excited, it emits light in all directions at various wavelengths depending on its band gap and other states. A portion of the emitted light collected and passes through the entrance of the spectrograph.

3.6 Time Correlation Single Phonon Counting

Time resolved fluorescence measurements were carried out using the time-correlated single photon counting (TCSPC) technique. It is a most widely used technique to record the time dependent fluorescence or PL of a sample with single photon detection sensitivity in the nanosecond to picosecond time scale. The basic principle of the TCSPC relies on the fact that after excitation of the sample with short pulse from a laser, time-dependent probability distribution of the single photon emission from the sample is equivalent to time dependent changes in the fluorescence intensity in the sample following its short pulse excitation [159,160].

Figure 3.9 describes a schematic block diagram of a TCSPC system. The excitation light pulse from the excitation source is split into two parts. One part is used to excite the sample and another part is directed to trigger a photodiode. The optical signal generated by the photodiode generates an electrical START signal which is routed through a constant-fraction-discriminator (CFD) and reaches to the time to amplitude converter (TAC) module. After receiving the start pulse, a timing capacitor in the TAC starts to charge linearly. Meanwhile, the sample after optical excitation emits the photons. These emitted photons are detected one by one by the PMT to generate electrical STOP pulses for each of the individual emission photon received. These electrical pulses which are also routed through another CFD reaches to the same TAC unit.

On receiving the first electrical STOP pulse, TAC stops the charging of the capacitor and delivers a voltage output which is directly proportional to the delay time (Δt) between the start and stop pulses reaching the TAC unit. The ADC module converts this voltage to a numerical value which is then fed into the input of a multi-channel

analyzer (MCA) and selects the particular channel in the MCA where a single count is added up. A histogram of the counts is generated in the MCA after repetition of this cycle (from excitation to data storage in the MCA) again and again.

This distribution of the counts against the channel number in MCA represents the fluorescence decay curve of the sample which is convoluted with instrument response function (IRF) of the TCSPC system. IRF is the dead time of the TCSPC and limits its time resolution. IRF is collected in a similar way just by replacing the sample by a non-fluorescent thin scattering sample. Using an iterative method, the intrinsic emission decay kinetics is deconvoluted from the IRF. To avoid the pulse pile-up error, the collection rate of the emission photons by the stop PMT is kept low, around 2% or less, compared to the repetition rate of the excitation pulses. Low pulse energy and low sample concentration are also recommended to ignore this effect. For the measurements carried out in this thesis, a TCSPC system called Lifespec-RED from Edinburgh Instruments is used.

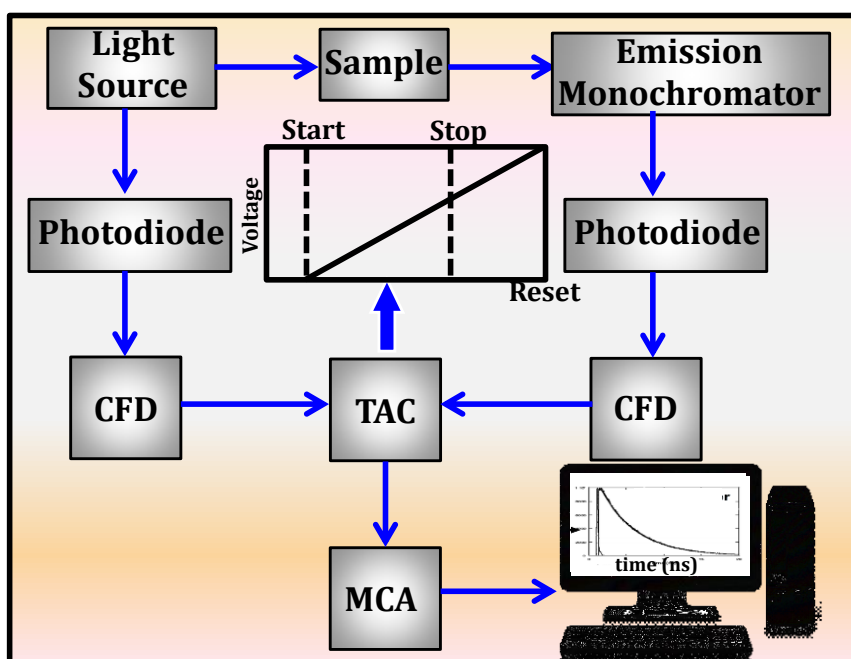


Figure 3.9: Typical block diagram of a TCSPC instrument.

Second harmonic output of a tunable femtosecond laser (Cohrent Model Verdi pumped by Cohrent Model Mira) was used as the

excitation source having pulses of ~ 150 fs. A pulse picker (Coherent model 9200) was used to select pulses at 3.8 MHz repetition rate. Fluorescence from the sample was collected at the right angle to the excitation. An emission polarizer was used before the collection optics and fluorescence is recorded at angle 54.7° polarization with respect to excitation light. To avoid the scattered excitation light, proper emission filters were used. Fluorescence signal was detected by a thermoelectric cooled Hamamatsu microchannel plate PMT (R3809U-50) and the IRF of this instrument was ~ 50 ps. The fluorescence decays were deconvoluted from the IRF and fit to either single or multi exponential function as described in the Eq.3.3.

$$I(t) = \sum_i a_i e^{\left(-\frac{t}{\tau_i}\right)}, \quad (3.3)$$

where τ_i is the fluorescence lifetime, a_i is the amplitude of the decay lifetime. The goodness of the fit was judged by visual inspection of the plots of weighted residuals which was randomly distributed around zero line and reduced chi-square value close to 1.0 [160].

Chapter 4

Fabrication and Surface Morphology of Silicon Nanostructures

This chapter deals with the fabrication and study of resulting morphology of Si NSs prepared by MIE. The MIE mechanism and role of metal nanoparticles herein have been discussed on the basis of charge transfer dynamics between surfaces involved. The step by step modification in surface morphology of samples has been understood with the help of SEM and TEM. The fractal nature has been observed in the porous Si fabricated by MIE technique. The SEM and TEM studies have been consolidated to model the growth mechanism for the observed fractal nature of porous Si¹.

¹Priyanka et al., *Silicon*, 1–7. (2018),

Priyanka et al., *Superlattices Microstruct*, 120,141-147, (2018)

4.1 Surface Morphology of Si Nanostructures

The Si NSs have been fabricated using MIE [31,48,161] technique in the current study. The SEM and TEM microscopic tool have been used to study the surface and X-sectional morphologies of all the samples. The systematic SEM images have been recorded to understand the step-by-step progress of etching. The MIE is mainly a two steps process as discussed in chapter 3. Figure 4.1 shows the cleaned Si wafer surface which has been used for etching by dipped into the solution containing 4.8M HF and 5mM AgNO₃ for the deposition of AgNPs on the wafer surface at room temperature for 1 min and then rinsed with DI water to remove the extra silver.

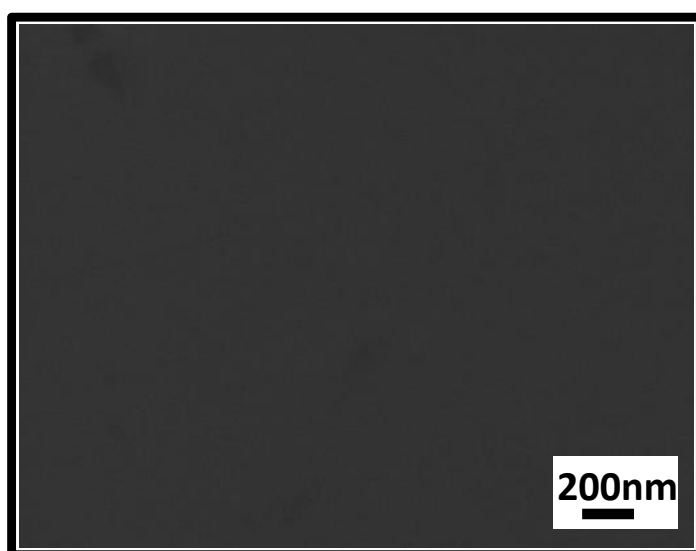


Figure 4.1: SEM image of a clean surface of Si wafer.

Surface morphologies of AgNPs deposited n- and p- type Si wafers with different resistivity have been shown in Figure 4.2. It is evident from Figure 4.2 that the AgNPs of different shapes and sizes have been successfully deposited on both the types of Si wafers (sample description given in Table 3.1 in chapter 3). In order to fabricate the Si NSs, the AgNPs deposited Si wafer is transferred to the etching solution containing 4.8M HF & 0.5M H₂O₂ and kept there for 60 min.

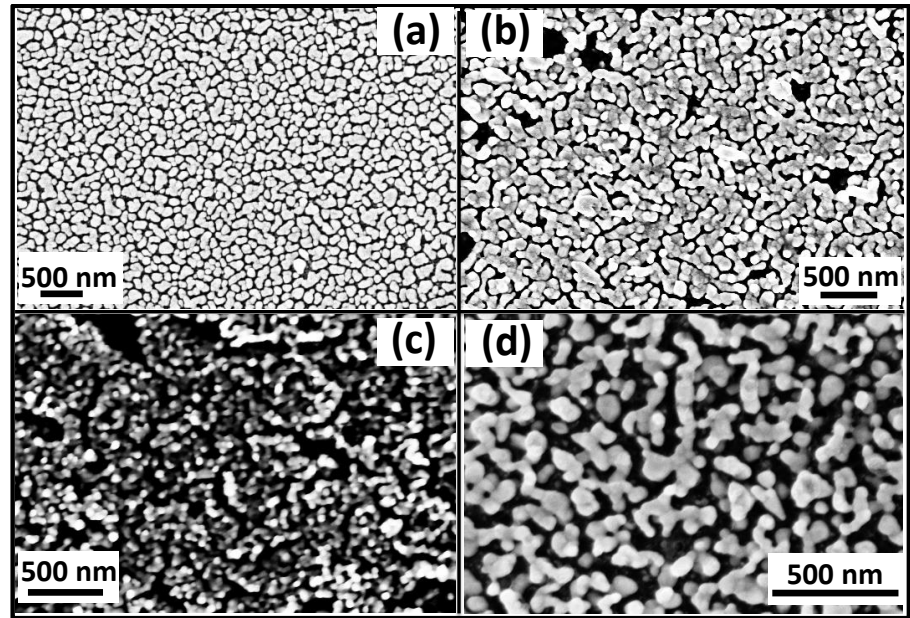


Figure 4.2: Surface morphology of AgNPs deposited Si wafers (a) $N_{Ag}^{\#}$, (b) $P_{Ag}^{\#}$, (c) N_{Ag}^{*} and (d) P_{Ag}^{*} .

The etched Si wafer is dipped in the HNO_3 acid for 2 min to remove the residual AgNPs. A strong oxide layer is formed on the etched Si wafer after the treatment of HNO_3 acid. In order to remove the oxide layer from the SiNWs, samples were transferred to HF solution and then washed with DI. To see whether the Si wafers after etching have some modification or not the SEM images of etched Si wafer have been recorded. Figure 4.3 shows the SEM images of etched Si wafers.

It can be observed from the surface morphologies of both n- and p-type Si wafers that the pore like structures are formed which are spread on the whole surface. As have been reported earlier [48,49,162] that these pores might be interconnected or may be parallel to one another depending on the specifications of Si wafers used for the porosification. In order to know the nature of pores, X-sectional SEM images of all samples, have been recorded and shown in Figure 4.4. Figure 4.4 confirms that the wire like structures have been successfully fabricated in all the etched Si wafers.

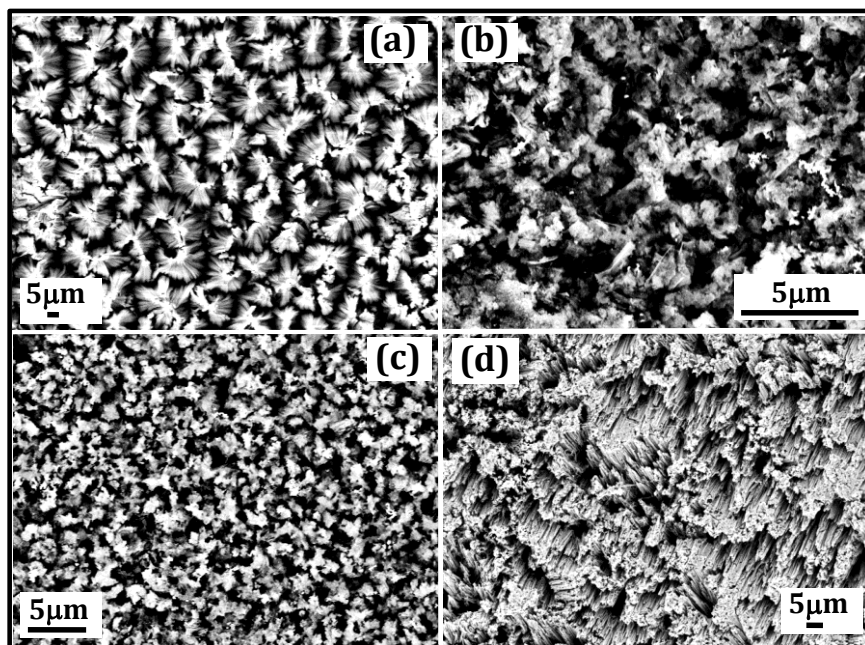


Fig 4.3: Surface morphology of etched Si wafer (a) $N^{\#}$, (b) $P^{\#}$, (c) N^{*} and (d) P^{*} .

The SiNWs are laterally separated by pores of width varying from sub-microns to a few microns. The height of SiNWs is decided by the etching time because when the etching time increases the vertical penetration distance of MNPs in Si wafer also increases due to progress of etching which result in height of the wires (SiNWs).

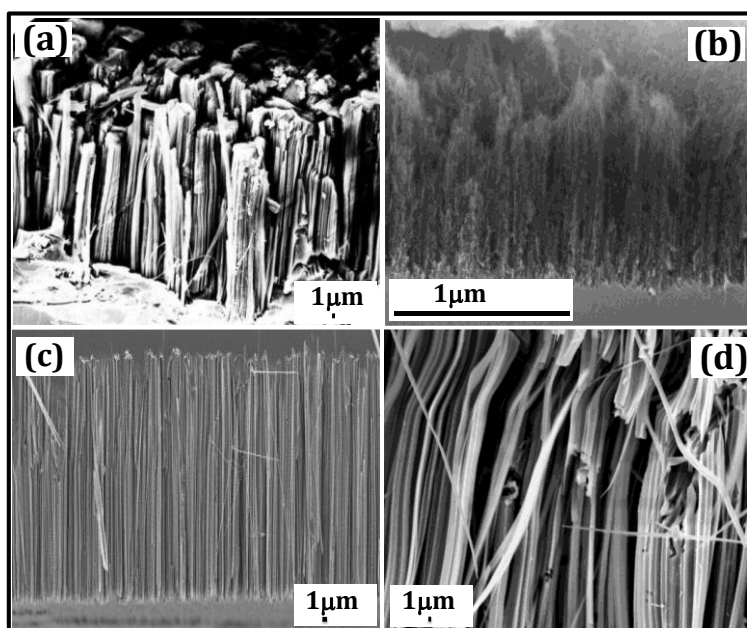


Figure 4.4: Cross sectional SEM images of etched Si samples (a) $N^{\#}$, (b) $P^{\#}$, (c) N^{*} and (d) P^{*} .

Figure 4.4 reveals that the wires are well aligned, straight as well as uniformly distributed throughout in all the samples, as has already been reported [61,62,163]. Even though the well aligned SiNWs have been successfully fabricated by MIE, but the exact mechanism of MIE is still not clear and certain ambiguity remains regarding the role of metal nanoparticles which is very important to be revealed.

4.2 Porosification Mechanism and Role of Metal

As discussed above, the MIE method involves mainly two steps, the deposition of MNPs and the porosification step. When the clean Si wafer is dipped into the solution of AgNO_3 and HF, the Ag^+ ions, available in the solution of AgNO_3 & HF sit on the surface of Si. Here Ag^+ takes one electron from the Si and gets neutralized for getting deposited as AgNPs after many such ions' neutralization on the surface. The exchange of electron from Si to Ag^+ is favourable because the redox energy for the pair Ag^+/Ag (0.79 V) is higher than the valence band energy of Si (0.62 V) [164] as depicted in Figure 4.5 which shows the redox pair energies and valence band energies.

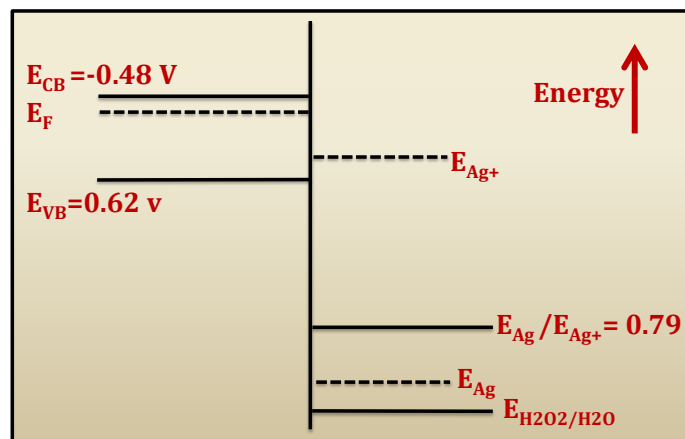


Figure 4.5: The schematic diagram showing redox pair energies with respect to hydrogen electrode potential.

The exchange of electron from Si to Ag^+ induces injection of holes (creation of positive site in Si) in the Si which eventually initiates the porosification [48,73,165]. After taking the electron from Si wafer, AgNPs gets deposited on the surface of Si wafer. Further in the next

step, these AgNPs deposited samples are put into the etching solution which contains proper ratio of HF and H_2O_2 . The fluoride ions (F^-) present in the etching solution attack the positive sites of Si (where hole is present). This attack is known to be resulting in H_2SiF_6 before getting dissolved in HF solution and creates a physical pit on the surface of Si [166].

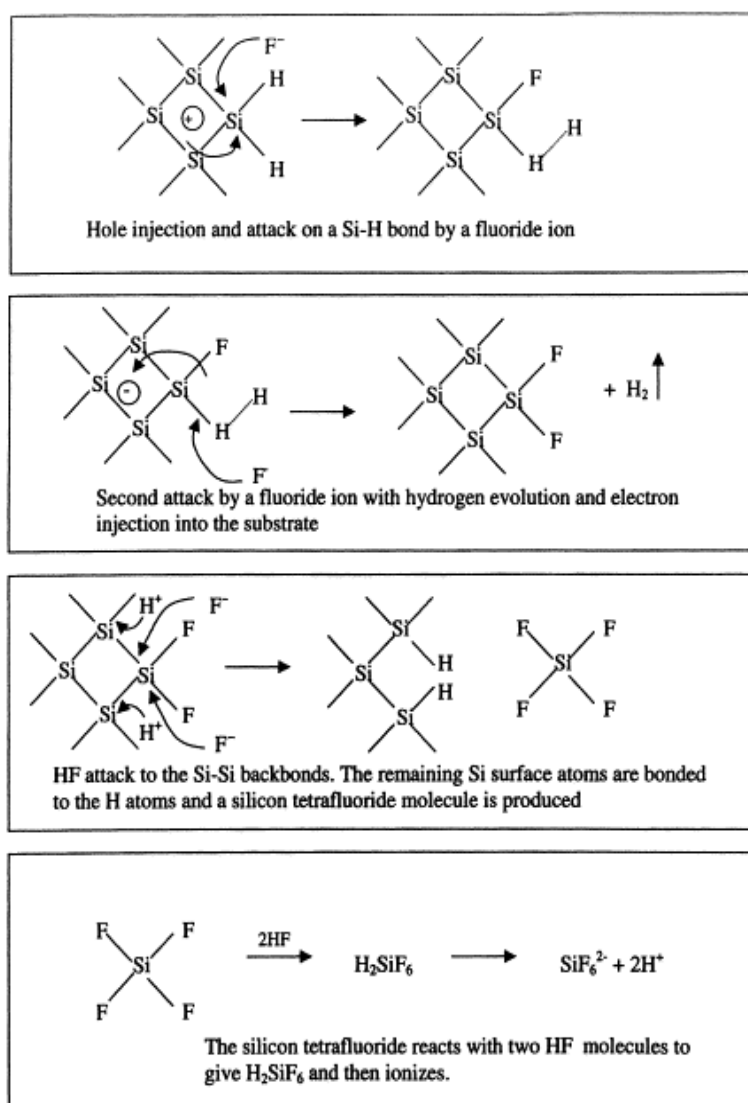


Figure 4.6: Dissolution mechanism of Si in the HF proposed by Lehmann and Foll [166].

The steps involved in dissolution of Si in the HF solution is depicted in the Figure 4.6 [166]. Further transfer of another electron from Ag to H_2O_2 takes place which results reduction of H_2O_2 and creation of Ag^+ to start the next cycle of etching by providing continuous supply of

Ag^+ and thus of the holes (h^+). The exchange of electron process and transfer of electron is favourable because the redox energy for the pair $\text{H}_2\text{O}_2 / \text{H}_2\text{O}$ (1.78 V) is higher (Figure 4.5) than the redox energy for the pair Ag^+/Ag (0.79 V) [164]. The continuation of cycle is governed by etching time which decides the depth of pits inside the Si wafer.

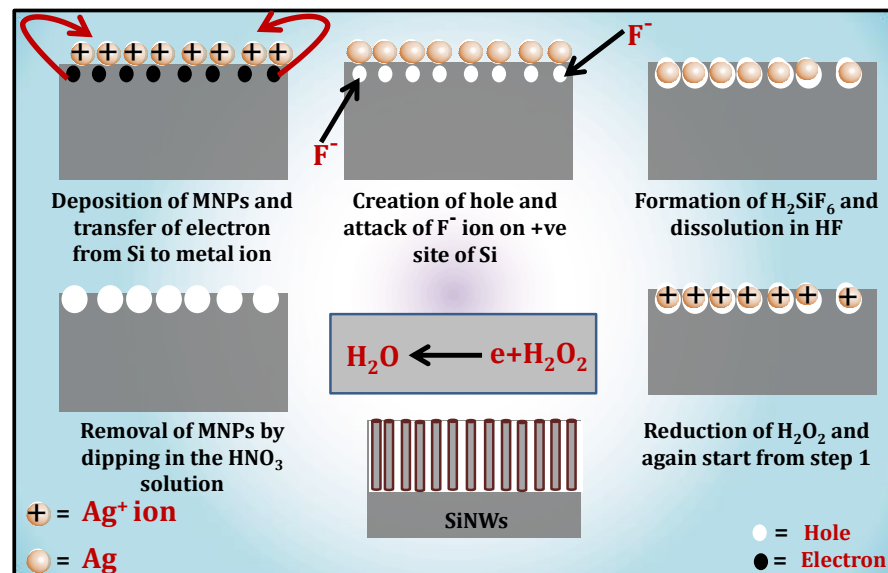
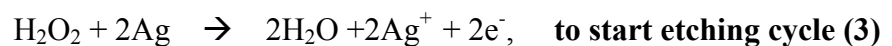
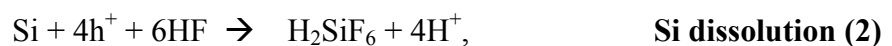


Figure 4.7: The schematic diagram depicting the porosification during MIE.

The chemical reactions involved during the fabrication of SiNWs in MIE are as follows [70]:



The schematic displayed in Figure 4.7 shows the overall step-by-step formation mechanism involved in MIE. It is worth mentioning here that the dissolution starts from the sites where metal nanoparticles are present (Fig 4.7). Figure 4.7 indicates that, if more metal nanoparticles cover the surface of Si wafer than it will result in higher porosification leading to highly porous Si surface.

4.3 Porosification and Effect of Metal

4.3.1 Surface Morphology Resulting from Different Metal Nanoparticles

It is clear from the above discussion that the etching process strongly depends on the MNPs and presence of holes. Thus, the role of MNPs/semiconductor junction cannot be neglected as either of the two junctions (Ohmic/Schottky) can be formed depending on the relative Fermi energies and work functions. This will affect the flow of holes and thus the porosification [167]. In order to understand the effect of MNPs, and hence the surface dynamics therein, on the porosification of Si surface two types of MNPs have been used for fabrication of Si NSs from n- and p- type Si wafers.

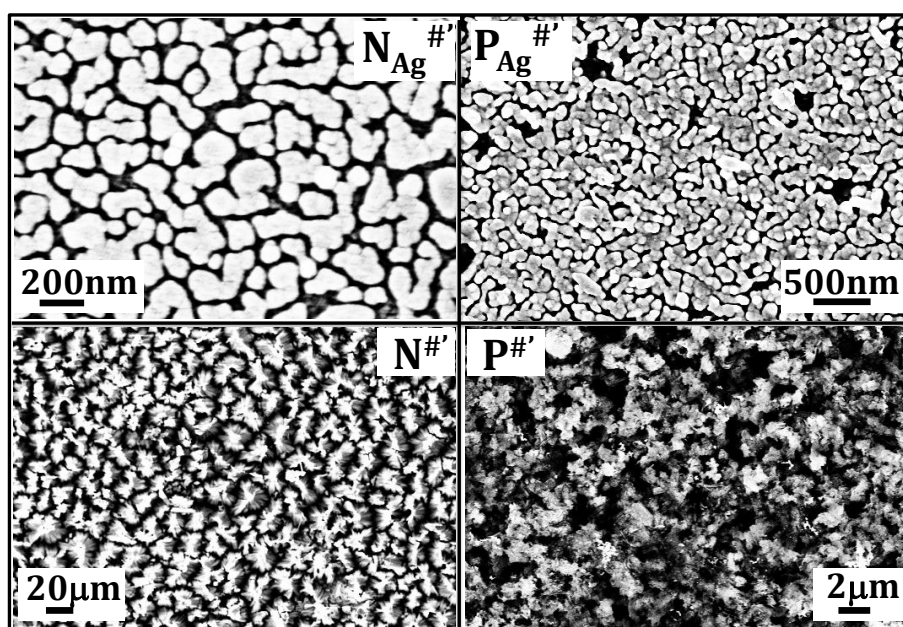


Figure 4.8: The top panel images are surface morphologies of AgNPs deposited n- and p- type Si wafers (sample $N_{Ag}^{\#}$ and $P_{Ag}^{\#}$) and bottom panel shows the top view SEM images of sample $N^{\#}$ and $P^{\#}$ respectively.

Figure 4.8 shows the SEM images of AgNPs deposited surfaces and its corresponding etched Si wafers. The images in top panel are surface morphologies of AgNPs deposited Si wafer whereas bottom panel

shows the top view SEM images of sample $N^{\#}$ and $P^{\#}$ respectively. It can be observed from Figure 4.8 (bottom panel) that the top view surface morphology of etched n-type and p-type Si wafer shows different surface morphologies, by keeping the other parameters constant (deposition and etching time), possibly due to the nature of junction between Ag with n- and p-type Si wafer. In case of sample $N^{\#}$ some tent like structures are apparent in the top view (as will be discussed in detail later) and on the other hand, for sample $P^{\#}$ the pores like structures are apparent. As it is well known that, since the contact between Ag and n-type Si wafer is different from the contact between Ag and p-type, the surface morphology of both n- and p- type etched Si wafer (top view) may be different and will be validated in later.

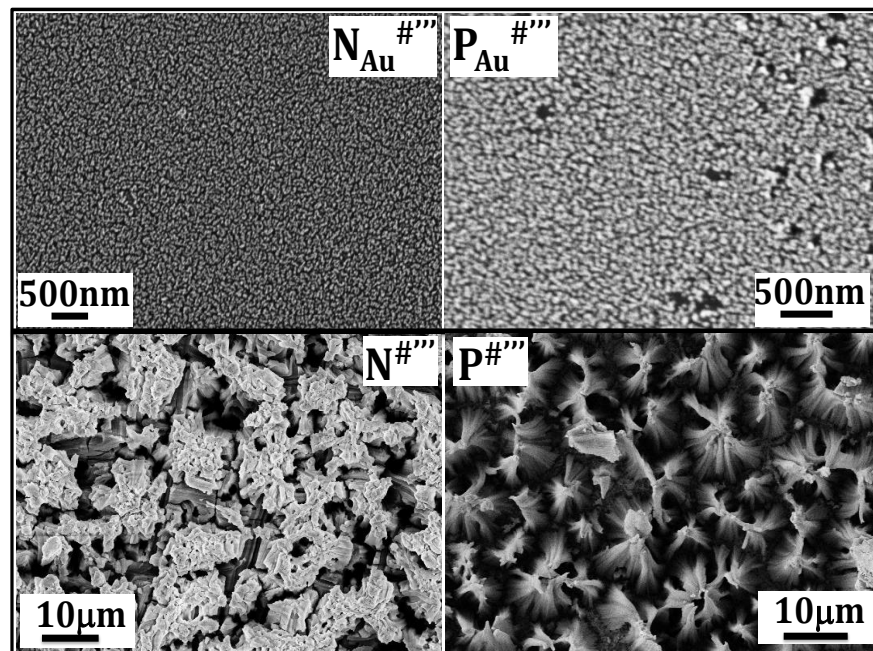


Figure 4.9: The top panel images are surface morphologies of AuNPs deposited Si wafer (sample $N_{Au}^{\#}$ and $P_{Au}^{\#}$) and bottom panel shows the top view SEM images (surface morphologies) of sample $N^{\#}$ and $P^{\#}$ respectively.

To further confirm that the contact between MNPs & Si wafer gives different texturization on porosification another set of samples were

prepared using gold nanoparticles (AuNPs). The top panel images in Figure 4.9 show the surface morphologies of AuNPs deposited Si wafer and bottom panel shows the top view SEM images (surface morphologies) of sample N[#] and P[#] (obtained after porosification) respectively. It is clear from Figure 4.9 (bottom panel) that the surface morphologies of porous n- and p- type Si are different from each other which is likely again due to the nature of junction between Au and n- & p-type Si wafer. It is observed from Figure 4.9 (bottom panel) that the Si NSs fabricated from p-type Si wafer using AuNPs shows similar behaviour (top view surface morphology of SEM images) as the Si NSs fabricated by n-type Si wafer using AgNPs (compare with Figure 4.8 bottom panel). It is worth mentioning here that the junction between Ag and n-type Si wafer is same as the junction between the p-type and Au metal nanoparticles (Ohmic junction).

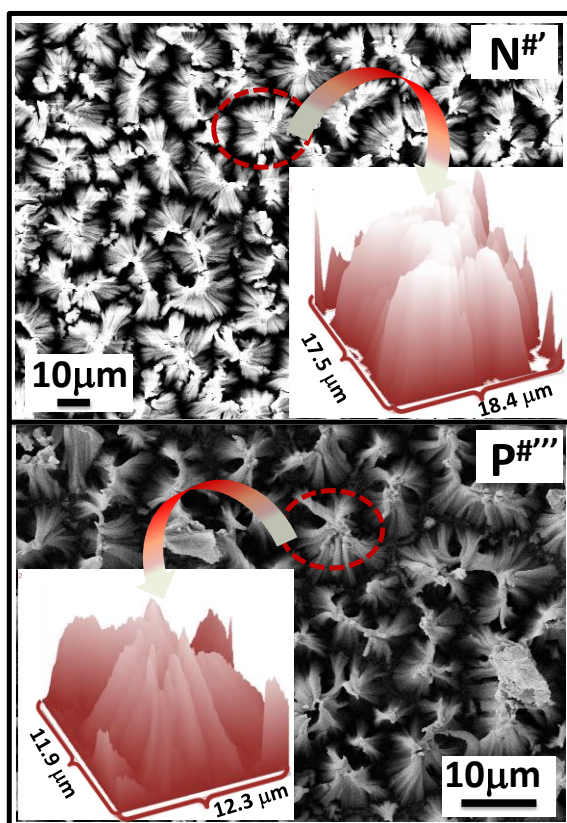


Figure 4.10: SEM images used to analyse (using ImageJ) the tent like structure in samples N[#] and P[#]. Inset shows the selected area (marked by red circle) 3D surface plot.

It is evident from Figure 4.8 & 4.9 that the morphologies of samples $N^{\#}$ and $P^{\#}$ are similar and simultaneously are different from samples $P^{\#}$ & $N^{\#}$ which are obtained after porosification of samples with non-Ohmic contact (non-tent shape top view morphology). To understand the 3D morphology of SEM micrographs ImageJ software is used. The 3D representation of SEM images of a single tent structure has been obtained by appropriately selecting an area of SEM image, converted to grayscale image, and then using “surface plot” option from “Analyze” menu in ImageJ software of the selected area which result in tent shaped 3D image (Figure 4.10). Surface plots obtained from SEM images of sample $N^{\#}$ and $P^{\#}$ have been shown in Figure 4.10 along with the corresponding SEM images where tent-shaped structure is visible clearly [167].

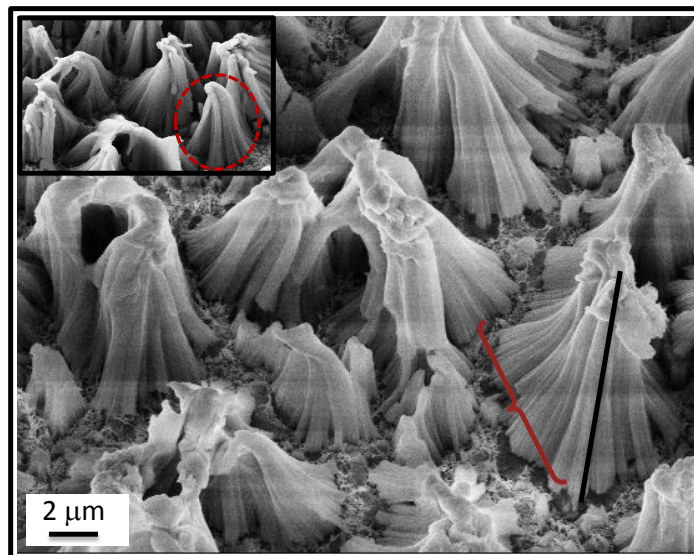


Figure 4.11: SEM image of sample $P^{\#}$ obtained by tilting the sample. The red and black marked line shows the single tent width and height respectively. Inset shows the bending of Si-tent tip.

The tent-shaped morphology has also been observed from sample $P^{\#}$, by using AuNPs as shown in SEM image (Figure 4.11) recorded with tilt angle of 45 degrees. It is evident from Figure 4.11 that tent shaped

morphologies are successfully fabricated in p-type wafer when AuNPs are used. The width of tent shaped Si NSs is of the order of $10\mu\text{m}$ marked with red curve (Figure 4.11) and is confirmed from the surface plot extracted using ImageJ. The surface plot shown in the inset of Figure 4.10 is used to calculate the tent angle which was found to be $\sim 72^\circ$ and 62° for samples N[#] and P[#] respectively. The approximate height of single Si NSs tent is $10\mu\text{m}$ in case of P[#] marked by black line (Figure 4.11) and the spacing between two consecutive tent is of the order of $1\mu\text{m}$.

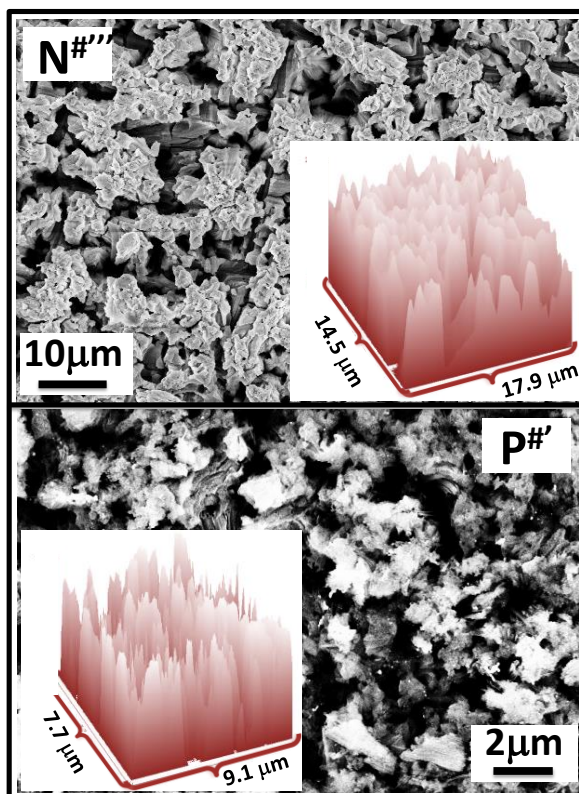


Figure 4.12: SEM images used for the ImageJ to analyse the tent structure in sample N[#] and P[#]. Inset shows the 3D surface plot of corresponding SEM images.

It is also evident from the SEM images (inset of Figure 4.11) that the tip of the tent is bent and looks as a bunch of SiNWs clubbed together indicating that bending of SiNWs on one another result in tent like structure. This kind of texturization can be thought to be originating as an effect of surface tension which will be discussed later. To observe

whether the tent shaped Si NSs are present in the sample where metal/semiconductor Schottky junctions (Ag and Au make non-ohmic junction with p-type and n-type Si wafer respectively) were formed in the pre-porosification stage, ImageJ analyses of sample N^{#''''} and P^{#'} have also been done which is shown in Figure 4.12. It has been observed from Figure 4.12 that the surface plot generated by sample N^{#''''} and P^{#'} does not show any tent-shaped structure on the surface. It is important here to mention that a clear correlation between the nano-metal/Si junction have been observed from the above discussion (from Figure 4.8 to 4.12).

4.3.2 Band Bending and Surface Texturization

To understand the nano-metal/semiconductor junction more clearly the band structure diagrams for Ohmic and Schottky junction have been drawn which is displayed in Figure 4.13 along with corresponding representative SEM micrographs. It is clearly noticeable that the metal Si combination (sample N^{#'} and P^{#''''}) forming Ohmic junction, when etched, results in tent-shaped morphology whereas Schottky junction (N^{#''''} and P^{#'}) nano-metal/Si combination result in wire like morphology. This kind of tent-shaped texturization can be thought to be originating as an effect of surface tension and can be understood as follows.

The fabricated SiNWs may feel the force from the solution are energetically unfavourable and hence will agglomerate to minimize the surface energy which will be very high in case if all the wires are separated [167]. The same has been explained by depicting the texturization of tent shaped Si NSs in Figure 4.14. In first step the metal nano- particles were deposited on the surface of Si wafer by dipping in metal solution and then metal nanoparticle loaded Si wafer were transferred in the etching solution. After etching the well aligned SiNWs have been formed which is shown in step 2. The etching time decides the length of SiNWs i.e., increase the etching time the length

of SiNWs also increases.

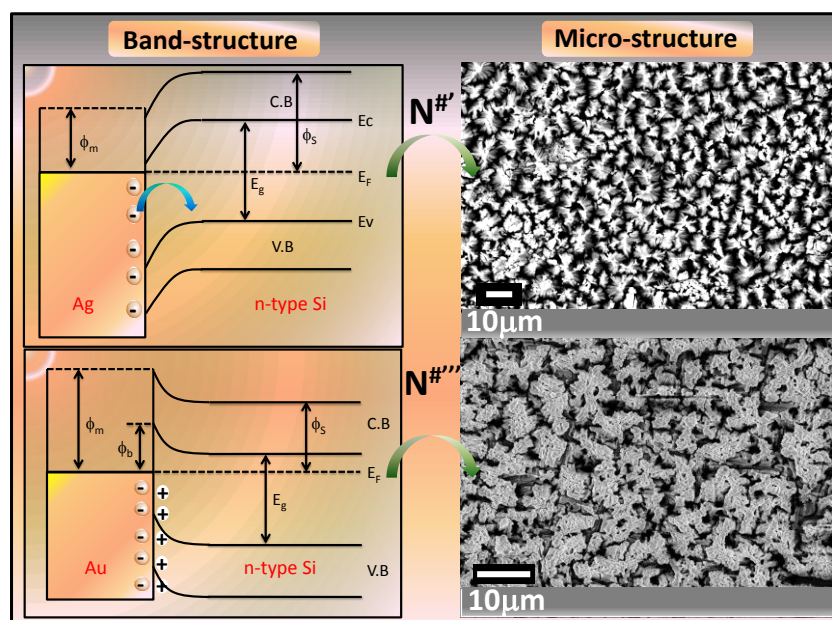


Figure 4.13: Band diagram along with SEM micrographs showing a correlation between band bending and morphology after porosification.

In step 3 the SiNWs start bending on each other as they are unable to sustain on their own due to increased length. This starts during removal of etched Si wafer from the etching solution the red arrow in circle shows the bending of SiNWs in step 3. In the final step the bunch of SiNWs were bent together and form a tent like structure when the etched Si wafer is removed completely from the etching solution.

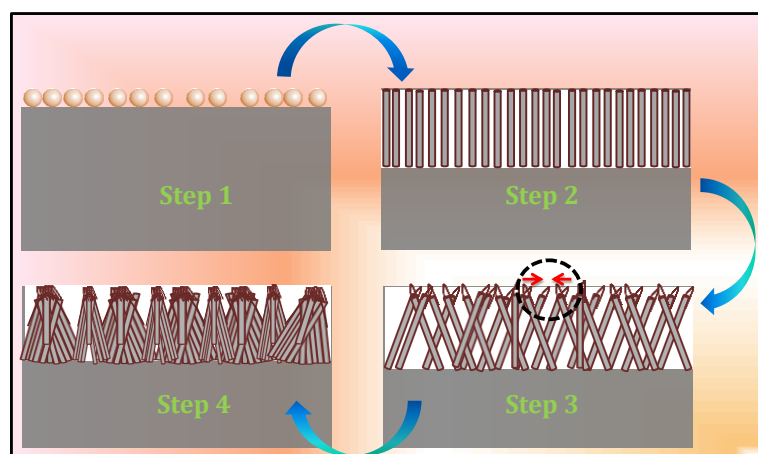


Figure 4.14: Schematic showing mechanism of texturization of Si wafer into nano tent of Si NSs. Red arrows, in step 3, show the direction of force being felt by the wires as a result of surface tension.

It is very likely that the bunch of SiNWs remain well aligned when they are in the etching solution. The base of SiNWs stay attached to the Si wafer. In this way, the SiNWs bend due to the surface tension effect. The surface tension shows the elastic tendency of the solution which forces it to acquire the least surface area possible. Similar to this, if the SiNWs bunch together they will acquire lesser surface area thus is a favourable move when removed from the etchant. This results in bunching of wires on one another and formation of Si tent (step 4).

4.4 Effect of Doping Level on the Porosification

Other parameters which may affect the structural morphology include doping level and type of dopant present in the Si wafer. Figure 4.15 shows the SEM images of samples which have been fabricated from Si wafers having different doping type (n- and p-type Si) as well as different doping level using MIE technique. The surface morphology of sample P^{*}, P[#], N^{*} and N[#] (sample details in Table –3.1 in chapter 3) are shown in Figure 4.15 (a) to (d) where pore like structures are clearly observed which are spread on the whole surface. The exact effect of doping level on structural properties can be understood by X-sectional SEM. The X-sectional SEM images of all sample have been recorded which have been displayed in Figure 4.15 (e) to (h).

It have been observed from X-sectional SEM images that well aligned nanowires, laterally separated by pores of width varying from sub-microns to a few microns, are fabricated in all the samples of n- and p-type Si wafers. Comparison of X-sectional images in right panel (Figure 4.15) indicates that relatively thinner SiNWs are present in sample P[#] as compared to sample P^{*} which has been prepared from low doped p-type Si wafer with respect to sample P[#] [61]. The n-type SiNWs also have been prepared with comparatively lower doping as compared to sample P[#]. It is also evident from Figure 4.15 (e) & (f) that the relatively thinner SiNWs have been present in P[#] as compared

to those in $N^{\#}$ because the doping level is high in $P^{\#}$ sample compare to $N^{\#}$ [168]. However the size estimation of the SiNWs using SEM is not exact because of its resolution limitations and will be estimated using Raman spectroscopy which is found to be a better tool for size estimation especially for Si NSs [85].

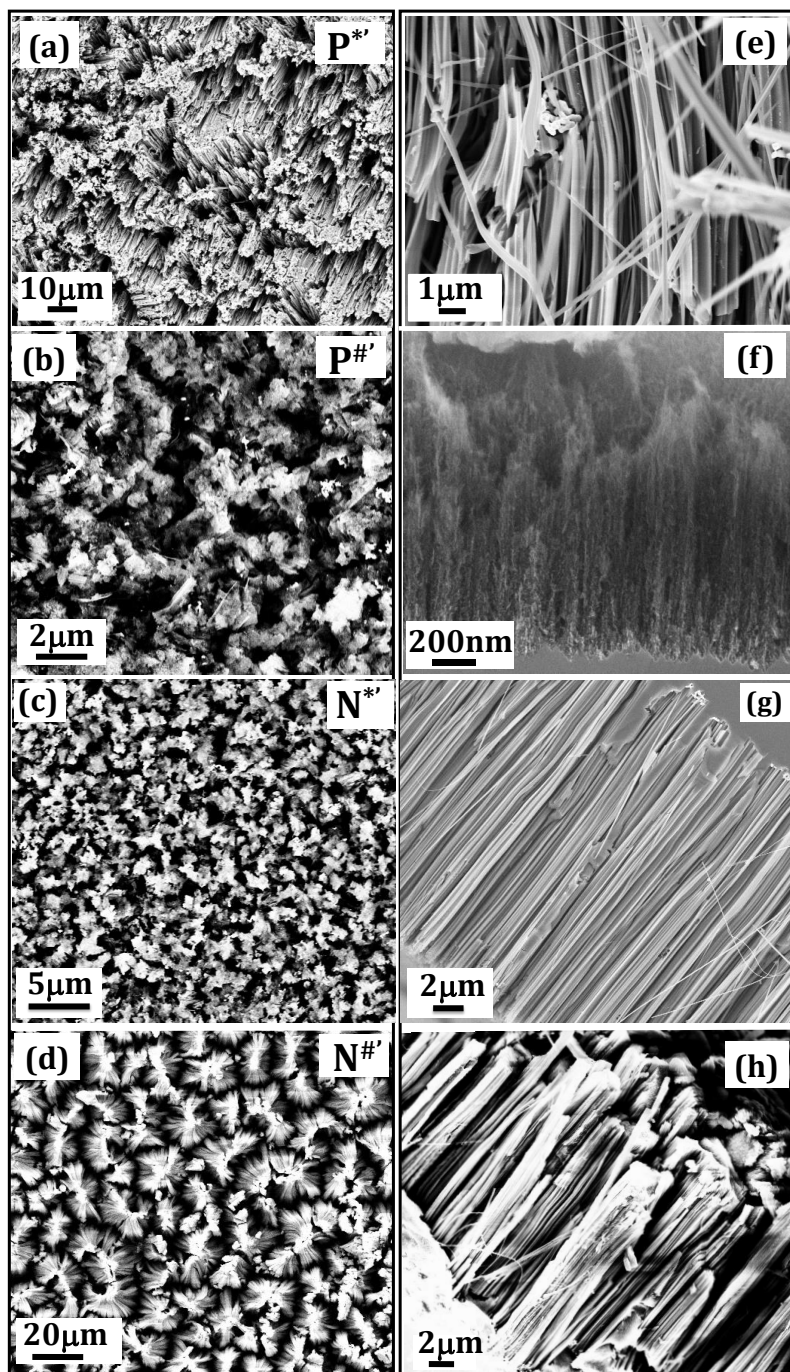


Figure 4.15: The left panel SEM images are surface morphologies whereas right panel images are X-sectional morphologies of sample P^{*} , $P^{\#}$, N^{*} and $N^{\#}$ respectively.

Further for better size estimation, TEM study has been carried out for samples P[#] and N[#] (Figures 4.16). The TEM images in Figure 4.16 suggest that further smaller nanostructures are present on the surface of SiNWs. It can be clearly seen from TEM images that smaller nanostructures of ~3nm are present in sample P[#], whereas sample N[#] contains Si NSs of sizes ~5.5nm. It is confirmed from the above discussion that comparatively smaller sized NSs are present in the highly doped Si wafer.

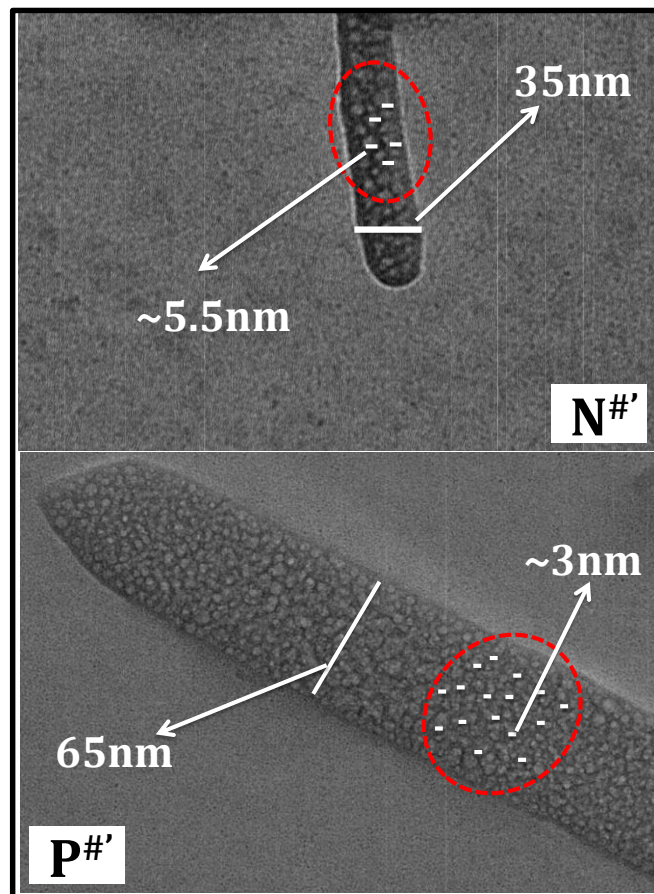


Figure 4.16: TEM images of samples N[#] and P[#].

In order to confirm the presence of these nano structures, and discount presence of any artefact, in the SiNWs one more set of same sample have been fabricated by keeping all the parameters constant (metal nano particle deposition time, etching time etc.). Figure 4.17 shows the TEM images of a portion of samples N[#] and P[#]. A ~50 nm thick

wire of Si can be seen in Figure 4.17. These small nanostructures appear to be of the order of a few nanometers (around ~5nm range) and are present on the surface of SiNWs in both the samples N[#] and P[#].

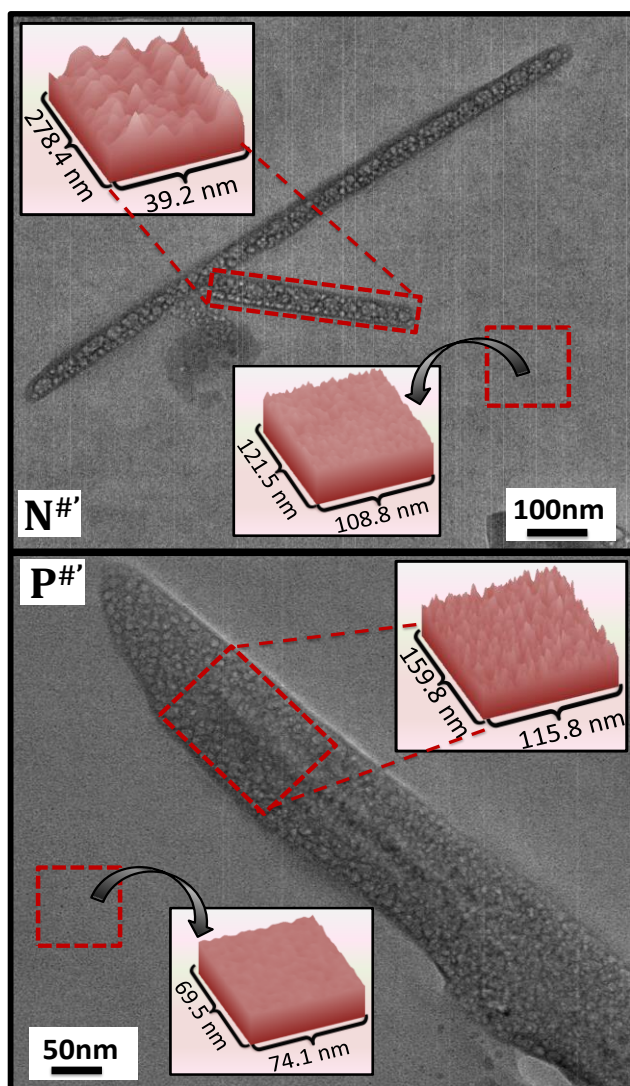


Figure 4.17: TEM image of samples N[#] and P[#], prepared by MIE. Inset shows the selected area (marked by red dotted line) 3D surface plot of TEM image.

For detailed analysis of this unorthodox structure, ImageJ was employed. The obtained surface plots from the wires visible in the TEM images have been shown in the insets along with the background areas also for comparison. It can be appreciated from the surface plots in insets of both the samples that the surface of SiNWs is not smooth rather is porous in nature. It is worth mentioning here that a porous Si

wafer, after MIE, contains nanowires which is also porous which gives a feeling of the fractal nature of porous Si as reported earlier [199] and appears to get revisited here which is a very interesting phenomenon. It is important here to understand the possible origin of the fractal nature of nanowire containing porous Si prepared by MIE. It has been established that the SiNWs fabricated using MIE technique produce nanowires which are well aligned and laterally separated by pores [61,75] giving it the porous nature. Presence of interconnected pores and especially the porous nature of nanowires themselves certainly mean that the path of chemical etching has taken place in non-vertical direction.

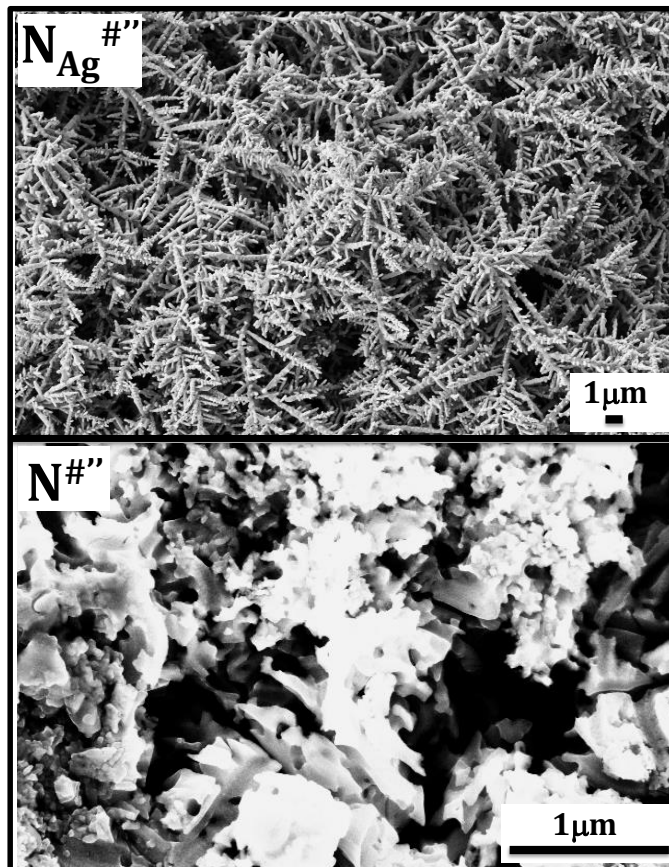


Figure 4.18: Surface morphologies of samples $N_{Ag}^{\#''}$ and $N^{\#''}$, top panel shows the AgNPs decorated Si wafer for 60 min and bottom panel shows the surface morphology of corresponding etched Si wafer (sample $N^{\#''}$).

It is evident from the above discussion that the formation of porous nanowires can take place only if the AgNPs proceed towards the pore

walls in non-vertical direction. In absence of the above, the pores will proceed vertically down and will result in non-porous nanowires on porous membrane. Before verifying the above hypothesis, regarding the non-vertical AgNPs movement, it is worth mentioning here that the material's growth depends on the nature of surfaces involved and are governed by associated surface energies. Keeping this in mind, growth mechanism of AgNPs, i.e. how the MNPs grow when the Si wafer put for long period in the metal solution.

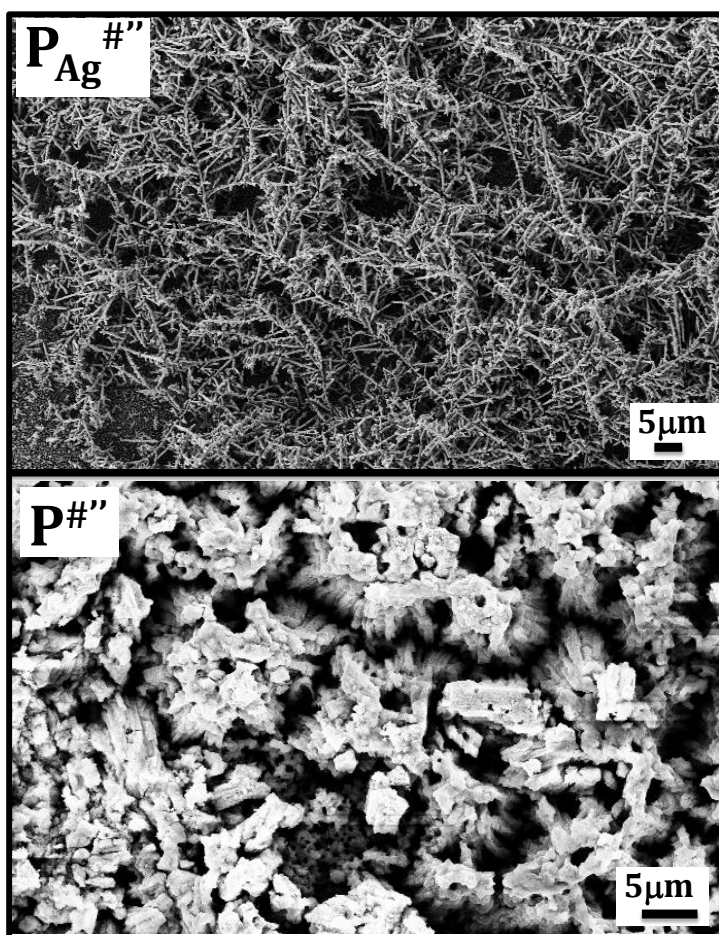


Figure 4.19: Surface morphologies of samples $P_{Ag}^{\#\prime\prime}$ (pre-porosification) and $P^{\#\prime\prime}$ (post-porosification), top panel shows the AgNPs decorated Si wafer for 60 min and bottom panel shows the surface morphology of corresponding etched Si wafer (sample $P^{\#\prime\prime}$).

To understand how AgNPs grows when it is kept in the precursor solution for longer duration, the deposition time of AgNPs has been increased to 60 minutes (as compared to 1 min for usual

porosification). Figure 4.18 shows the surface morphologies of The SEM images of samples $N_{Ag}^{\#''}$ (pre-porosification step) and $N^{\#''}$ (post-porosification step). It is evident from SEM image of sample $N_{Ag}^{\#''}$ that as the deposition time of metal nanoparticles increases the AgNPs growth in the form of dendritic structures. Similarly a p-type Si wafer was also used for growing AgNPs with growth time of 60 min resulting in dendritic growth same as on n-type Si wafer (Figure 4.19) [155]. It is evident from the top panels of Figure 4.18 & 4.19 (SEM images of samples $N_{Ag}^{\#''}$ and $P_{Ag}^{\#''}$, pre-porosification step) that when grown for 60 minutes the AgNPs grow in the form of dendrites rather growing like a wire or rod. It means that an Ag atom can get attached to the already available streak of Ag atoms, resulted after nucleation, at any place and not necessarily at the end of the streak. The latter will end up in the vertically downward proceeding of the AgNPs to result in non-connecting pores on Si wafer as reported being the case in MIE. The dendritic growth of AgNPs confirms the hypothesis that AgNPs can proceed in non-vertical direction and may penetrate the SiNWs resulted after MIE and end up with porous wires [155].

In order to see the effect of dendritic structure of AgNPs on etching of Si wafer, both of the dendritic AgNPs deposited Si wafers (60 min, dendritic AgNPs) have been transferred in the etching solution. The bottom panels of Figure 4.18 & 4.19 shows the etched Si wafers (sample $N^{\#''}$ and $P^{\#''}$). From Figure 4.18 & 4.19 (bottom panel) it is clear that the top view of sample $N^{\#''}$ and $P^{\#''}$ show entirely different morphology with respect to the sample $N^{\#}$ and $P^{\#}$ (bottom panel of Figure 4.8)². The surface morphologies of samples prepared by one minute Ag deposition shows specific pattern in the top view morphology whereas in case of 60 minutes AgNPs deposition the surface morphology shows rather random porosification. The above-

² Obtained after porosification of Si wafer with AgNPs grown only for 1 min.

mentioned correlation, evident from Figure 4.8 (bottom panel) and 4.18 & 4.19 (bottom panel), suggests that for porosification AgNPs act as etching centers which means that the dissolution of Si atoms starts from metal nanoparticles which act as nucleation sites. Previous study [48] reported that when Si wafers are dipped into the solution of AgNO_3 and HF, available Ag^+ ions get deposited on the surface of Si wafer, take one electron from the Si surface and get neutralized to Ag. This is a continuous process ($\text{Ag}^+ \rightarrow$ taking electron from Si \rightarrow desolation of Si \rightarrow Ag move in forward direction) which leads to the porosification.

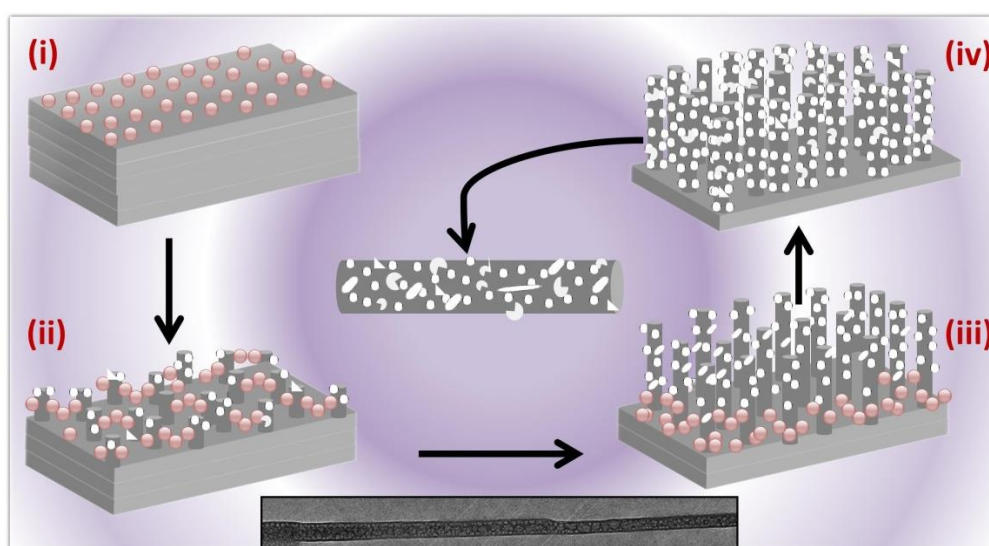


Figure 4.20: Schematic representation showing the formation of fractal porous Si (i) AgNPs deposited Si wafer followed by (ii) etching by MIE followed by (iii) non-vertical etching progress and resulting in (iv) porous nanowires present in porous Si matrix with inset showing the actual TEM image of one SiNWs.

The above discussion can be represented in the form of a schematic as shown in Figure 4.20. It is important to mention here that the formation of nanocrystal on the surface of SiNWs is attributed due to the shape and structure of Ag which can directly be confirmed from top panel of Figures 4.8, 4.18 & 4.19. It is equally important to mention here that, from the top panel images of Figure 4.8 (sample N_{Ag}^{*} and P_{Ag}^{*} , AgNPs deposited Si wafer) the shape of Ag is rather irregular, which

means that when the Ag moves in the forward direction following redox process [48] it corrodes the side walls of SiNWs and due to this process few nano meter sized Si nanocrystals get formed on the SiNWs. This can be elaborated on the basis of formation mechanism, as depicted in Figure 4.20, which is as follows. The AgNPs deposited Si wafer (step (i)) when dipped in etching solution of HF and H₂O₂ results in porous Si consisting of SiNWs (step (ii)) as a result of usual porosification by MIE. When etched for longer, the AgNPs move in non-vertical directions and penetrate through the walls of the pores at several places on the SiNWs which continue to corrode (etch) the wires (step (iii)) to result in a porous SiNWs in step (iv) after the removal of residual Ag. The end result being the porous NWs of Si present in the porous Si wafer matrix.

4.5 Summary

In summary, step by step etching mechanism of MIE has been understood. Surface morphologies of porous n- and p-type wafers obtained from silver- and gold- nanoparticle assisted etching have been studied to observe a correlation between obtained nanostructure and nano-metal/Si contact. A tent-shaped surface morphology is obtained, on porosification, when an Ohmic nanometal/Si junction is formed. The tent-shaped surface morphologies are irrespective of the wafer type (n- or p-) and are resulted as long as an Ohmic junction is formed with nano-metal used as catalyst. It is also observed that porous Si surfaces resulted after MIE ends up in SiNWs which are also porous. The presence of porous nanowires, at microlevel, in the overall porous Si surface, at macrolevel, means fractal type morphology. The SEM and TEM studies have been consolidated to model the growth mechanism for the observed fractal porous Si.

Chapter 5

Confined Phonons in Low Dimensional Silicon

Current chapter reports the behaviour of confined phonons, present in low dimensional Si, using Raman scattering. The Raman spectroscopy has been used to study the identification of the phase such as c-Si, Si NSs and *a*-Si. The effect of phonon confinement on Raman spectra of Si is studied in terms of the way the whole Raman spectral line-shape responds to a given confinement effect. An analytical model for asymmetric Raman line shape, observed from Si NSs, based on PCM is presented here. A theoretical model has also been presented in this chapter which is used to measure the short range order present in *a*-Si. The results presented in this chapter are published in different journals.³

5.1 Raman Scattering from Low Dimension Solids:

Theoretical background

Raman scattering replicates the nature of zone-centered optical phonons in crystalline solids. Theoretical background of Raman scattering from c-Si and *a*-Si has already been discussed in the chapter 2. Raman spectrum obtained from Si NSs shows different nature as compared to that from c-Si because the optical phonon's frequency in the Si NSs is likely to change from its bulk counterpart due to the finite size (confinement effect) of the material. Thus, the Raman spectral line-shape function from the Si NSs must be modified, from a typical

³ Priyanka et al. *J. Phys. Chem. C*, 2017, 121 (9), 5372–5378,
Priyanka et al. *J. Phys. Chem. Lett.* 2016, 7 (24), 5291–5296,
Priyanka et al., *Anal. Chem.* 2018, 90 (13), 8123–8129

Lorentzian function for c-Si, in accordance with the change in optical phonons frequency. At nanoscales, the breakdown of translational symmetry of (nano)crystalline materials at its grain boundaries, results in the deviation of vibrational contributions in the Raman spectra of that material [169,170]. As the size of materials is reduced to the order of its Bohr exciton radius, the effect of confinement of optical phonon vibration is more pronounced [91,171,172] which is reflected in Raman scattering.

With no exaggeration, Raman spectroscopy is said to be one of the most important tools which categorize the phase (crystalline, amorphous or nanocrystalline) [90,170,173]. Different models exist to illustrate the Raman line-shape resulting from the Si NSs [118,173,174]. The first-order Raman spectrum provides a fast and convenient method to analyze both the vibrational properties of crystalline as well as amorphous semiconductors. Since NSs of semiconducting material are quasi-crystalline, their Raman spectra are expected to be present in the intermediate range between the spectra of the corresponding crystalline and amorphous nature of the material.

Lot of research have been done in order to understand the vibrational properties in Si NSs [175,175,176], confined in one or more dimensions, using Raman spectroscopy. All the results usually show a (red-) shift in the peak position of the first-order Raman line of crystalline semiconductors along with a spectral broadening [177–179] which results in asymmetric Raman spectrum from Si NSs. Figure 5.1 shows the typical phonon dispersion and corresponding Raman line-shape of Si, where left hand side and right hand side display Raman active optical mode for c-Si and Si NSs, respectively. Raman scattering is used to estimate the Si NSs size using PCM proposed by Richter *et al.* [91], which was further modified by Campbell *et al* [173].

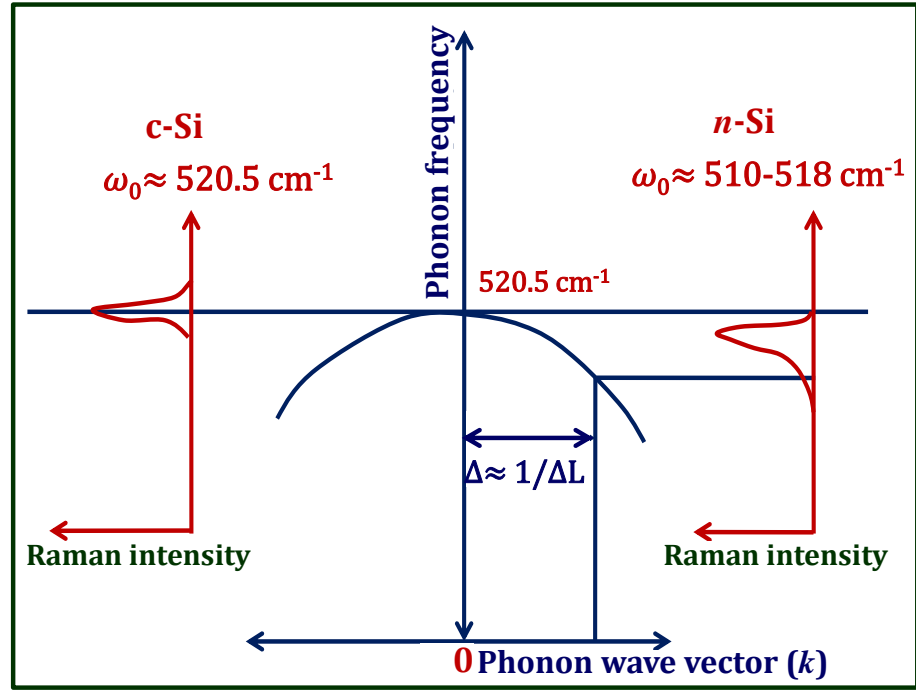


Figure 5.1: Schematic diagram showing the phonon dispersion and Raman line-shape of Si, where left hand side and right hand side display Raman active optical mode for c-Si and Si NSs, respectively.

5.2 Phonon Confinement Model

In a single crystal, only zone centered optical phonons contribute to Raman spectrum (near the Brillouin-zone center i.e, $k = 0$) due to the momentum conservation rule. The PCM [102,202] accounts well for the observed Raman line-shape from the Si NSs. Richter *et al.* [91] proposed a very harmonious PCM for confined phonons in the Si NSs of spherical shape with diameter L . The plane wave function of the phonon is restricted within the finite sized NSs. The wave function of a phonon with wave vector k_0 , in a crystal is defined in polar coordinates as [173]:

$$\Phi(k_0, r) = u(k_0, r)e^{-i\vec{k}_0 \cdot r}, \quad (5.1)$$

where $u(k_0, r)$ is the periodicity of the lattice. In case of a finite crystal of dimension L , the phonons are restricted to its volume. Phonons inside the Si NSs can be described by the following weighting functions $W(\vec{r}, \vec{L})$ [173].

$$\Psi(\vec{k}_0, \vec{r}) = W(\vec{r}, \vec{L})\varphi(\vec{k}_0, \vec{r}), \quad (5.2)$$

Using Eq. (5.1) in the Eq. (5.2)

$$\Psi(\vec{k}_0, \vec{r}) = \Psi'(\vec{k}_0, \vec{r}) u(\vec{k}_0, \vec{r}), \quad (5.3)$$

where,

$$\Psi'(\vec{k}_0, \vec{r}) = W(\vec{r}, \vec{L})e^{-i\vec{k}_0 \cdot \vec{r}}, \quad (5.4)$$

Richter *et al.*[102] chose the $W(\vec{r}, \vec{L})$ to be a Gaussian of the form $\exp(-2r^2/L^2)$, with a phonon amplitude of $1/e$ at the boundary of the finite crystal. For line-shape of the Raman spectrum, $\Psi'(\vec{k}_0, \vec{r})$ might be expanded in a Fourier series as:

$$\Psi'(\vec{k}_0, \vec{r}) = \int C(\vec{k}_0, k)e^{i\vec{k}_0 \cdot \vec{r}} d^3k, \quad (5.5)$$

where the corresponding Fourier coefficient $C(k_0, k)$ is given by[102]

$$C(\vec{k}_0, k) = \frac{1}{(2\pi)^3} \int \Psi'(\vec{k}_0, r) e^{-i\vec{k} \cdot r} d^3r, \quad (5.6)$$

Thus, the phonon wave function in a finite crystal is no longer an eigen function of the phonon wave vector k_0 but rather a superposition of the eigen functions with k vectors around $k = 0$. For a spherical finite crystal, the Fourier coefficients are given as $|C(\vec{k}_0, k)|^2 \sim \exp(-k^2L^2/4)$, where k_0 is assumed to be 0. Thus intensity of the first-order Raman scattering, $I(\omega)$, can be written as [173].

$$I(\omega) = \int \frac{|C(\vec{k}_0, k)|^2}{\left[\omega - \omega(k)\right]^2 + \left(\frac{\gamma_0}{2}\right)^2} d^3k, \quad (5.7)$$

where $\omega(k)$ is the phonon dispersion function for the optical branch of c-Si and γ_0 is natural line width of Raman spectrum of c-Si. This assumption is justified owing to the fact that only a small portion of the Brillouin-zone centered at the γ point contributes to the scattering. Different weighting functions, namely *sinc* [Eq. (5.8)], *exponential* [Eq. (5.9)] and *Gaussian* [Eq. (5.10)] respectively have been proposed for the Fourier coefficients [204] as given below.

$$|C(0, k)|^2 \approx \frac{\sin\left(\frac{KL}{2}\right)}{(4\pi^2 - q^2L^2)^2}, \quad W(r, L) = \frac{\sin\left(\frac{2\pi r}{L}\right)}{\left(\frac{2\pi r}{L}\right)}, \quad (5.8)$$

$$|C(0, k)|^2 \approx \frac{1}{(16\pi^2 - k^2L^2)^4}, \quad W(r, L) = e^{-4\pi^2 r/L}, \quad (5.9)$$

$$|C(0, k)|^2 \approx \frac{e^{-k^2L^2}}{16} \pi^2, \quad W(r, L) = e^{-8\pi^2 r/L^2}, \quad (5.10)$$

Figure 5.2 shows the confined NSs in three, two or one dimension (sphere, column and thin film, respectively). Effect of the size on the position and shape of the Raman band is strongest for a sphere whereas marginal for ultra-thin films. Many research groups [172,180–182] have established theoretical formalisms for calculating first-order Raman scattering from NSs. Shape and size distribution in an ensemble of small NSs have also been incorporated in their calculations along with the effect of the reduced size [102,214].

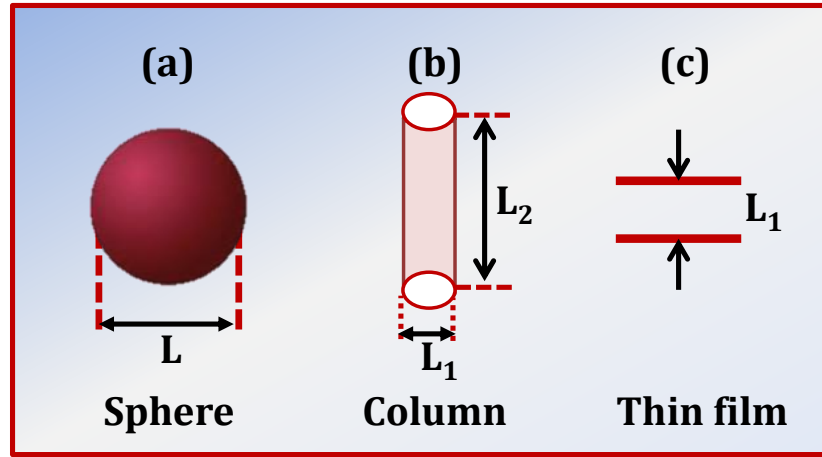


Figure 5.2: Confined NSs in (a) three (sphere), (b) two (column) and (c) one (thin film) dimension.

It is found that the Raman line-shape from Si NSs are explained very well using the relation $|C(0,k)|^2 = \exp[-(k^2L^2/4a^2)]$ [173]. For two dimensional confined system the volume integration (d^3k) in Eq. 5.6 needs to be replaced by the area integration (d^2k). Therefore the Raman line shape for a given size L for one dimensional confinement is:

$$I(\omega, L) = \int_0^1 \frac{e^{-\frac{k^2L^2}{4a^2}}}{[\omega - \omega(q)]^2 + \left(\frac{\Gamma}{2}\right)^2} d^2k, \quad (5.11)$$

It is possible that all the NSs may not have the same size. To incorporate the effect of this distribution, a Gaussian function of the form $N(L) \cong [\exp\{- (L-L_0)/\sigma\}^2]$ can be included in Eq. 5.11. Here ‘ L_0 ’ is the most probable or average size of the NSs and σ defines the width of distribution. It causes an additional broadening in the Raman line-shape described by Eq. 5.11. Incorporating these two modifications,

Eq. 5.11 is modified to Eq. 5.12:

$$I(\omega, L) = \int_{L_1}^{L_2} N(L) \left[\int_0^1 \frac{\exp\left(\frac{-k^2 L^2}{4a^2}\right)}{[\omega - \omega(k)]^2 + \left(\frac{\Gamma}{2}\right)^2} d^n k \right] dL, \quad (5.12)$$

Here, ‘ n ’ shows the degree of confinement and may take value 1, 2 or 3 for 1D, 2D or 3D confinement respectively. This equation will be used in section 5.3 for Raman line-shape analysis of Raman scattering data of Si NSs samples fabricated using MIE.

5.2.1 Evolution of Asymmetric Raman Line-Shape for Nanostructures

As discussed in the above section, due to momentum conservation law, only zone centered ($k=0$) phonons participate in Raman scattering for crystalline materials. As a result, symmetric, sharp peak is observed in the case of crystalline material centered at frequency corresponding to the zone centered phonon frequency. The formulation of Raman line shape has been started from phonon dispersion relation of respective material. In the present study phonon dispersion relation of Si, given by Eq. 5.13, is used while analyzing Raman spectral line-shape using Eq. 5.11 & 5.12. It is evident from Figure 5.3 that Raman line shape shows a typical symmetric Raman line-shape for bulk Si represented by a Lorentzian line-shape and can be written as Eq. 5.14. Inset of Figure 5.3 shows the longitudinal optic (LO) branch of phonon dispersion relation for Si (Eq. 5.13). The discrete points shown in inset of Figure 5.3 shows the data reported in literature for the same [103].

$$\omega(k) = \sqrt{171400 + 100000 \cos\frac{\pi k}{2}}, \quad (5.13)$$

The equation of Raman line shape for a crystalline bulk material is written as:

$$I(\omega) = \frac{1}{[\omega - \omega_0]^2 + (\gamma/2)^2}, \quad (5.14)$$

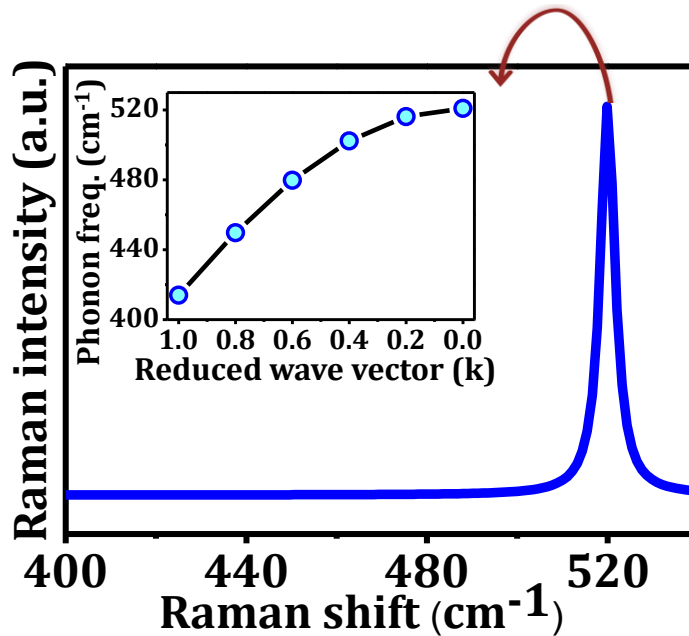


Figure 5.3: Symmetric Raman line shape for c-Si calculated using Eq. 5.14 and inset shows the dispersion curve for Si evaluated using Eq. 5.13.

where, ω_0 is $\omega(0)$ (Eq. 5.13) which is equal to 521 cm^{-1} for c-Si, γ is the full width at half maximum (FWHM) of the spectrum. As an example, symmetric Raman peak in the case of bulk Si is observed at $\sim 521 \text{ cm}^{-1}$ with FWHM of 4 cm^{-1} . But in the case of its nanostructured form, this selection rule gets relaxed and phonons other than the zone centered ones also contribute in a crystallite of finite dimension [72,171].

This results in a change in the first order Raman spectrum which is typically Lorentzian for crystalline materials. Line-shapes of Raman spectra from nanostructures are expected to be intermediate between those of the corresponding crystalline and amorphous materials. For example, a broad band around 480 cm^{-1} can be observed in the Raman spectra from amorphous Si [183,184] whereas at the other extreme of c-Si, a sharp symmetric Lorentzian peak is observed at 521 cm^{-1} corresponding to the zone-centered phonon (Figure 5.3) [90]. The change in the Raman line-shape parameters (peak position and FWHM) is useful in determining the size, shape and size distribution of NSs, since phonon softening and broadening of Raman lines are related to the size of nanostructures.

5.2.2 Effect of Size on Raman Line Shape

As discussed above, an asymmetrically broadened and red-shifted Raman line-shapes, represented by Eq. 5.11, are observed from Si NSs [39,185]. It is important here to mention that, there are three key observations, which are used to identify presence of confinement effect in Si, first, red-shifted Raman line-shape with respect to the c-Si, second, the non-unity asymmetry ratio (the ratio of half width towards lower energy side to the half width towards higher energy side) and third the broadened Raman line shape as compared to its c-Si counterpart. Asymmetry ratio is the measure of asymmetric broadening of Raman line shape and will be discussed later. It is clear from Eq. 5.11 that Raman line shape depends on the size of NSs (L).

Figure 5.4(a) shows the calculated Raman line shapes using Eq.5.11 by putting different crystallite sizes for a nano-system which is confined in one dimension only. The exponential term in Eq. 5.11 also takes care of the size dependence of the Raman line-shape by taking weighted average of contribution from each phonon present on the phonon dispersion curve [90]. Equation 5.11 can be understood as the basic Raman line-shape function for semiconductors nanostructured in particular and nanostructured materials in general. It is evident from Figure 5.4(a) that as the size of Si NSs decreases from 10 nm to 2 nm the broadening and asymmetry of Raman line shape increases along with spectral red-shift with respect to the c-Si. It is also evident from the Raman line shape generated using Eq.5.11 that the peak position is more redshifted for 2nm size as compared to the same for 10nm size.

To discuss quantitatively about the nature of these Raman line shapes, it is important to define the parameter called asymmetry ratio which is the ratio of the half widths towards lower energy side (γ_L) and higher energy side (γ_H) at $I/2$ *i.e.* at 50% of the total intensity respectively of the Raman peak (*i.e.* $\alpha_R = \frac{\gamma_L}{\gamma_H}$) as shown in Figure 5.4(b) which also defines the pre-maximum and post-maximum regions in a Raman spectrum.

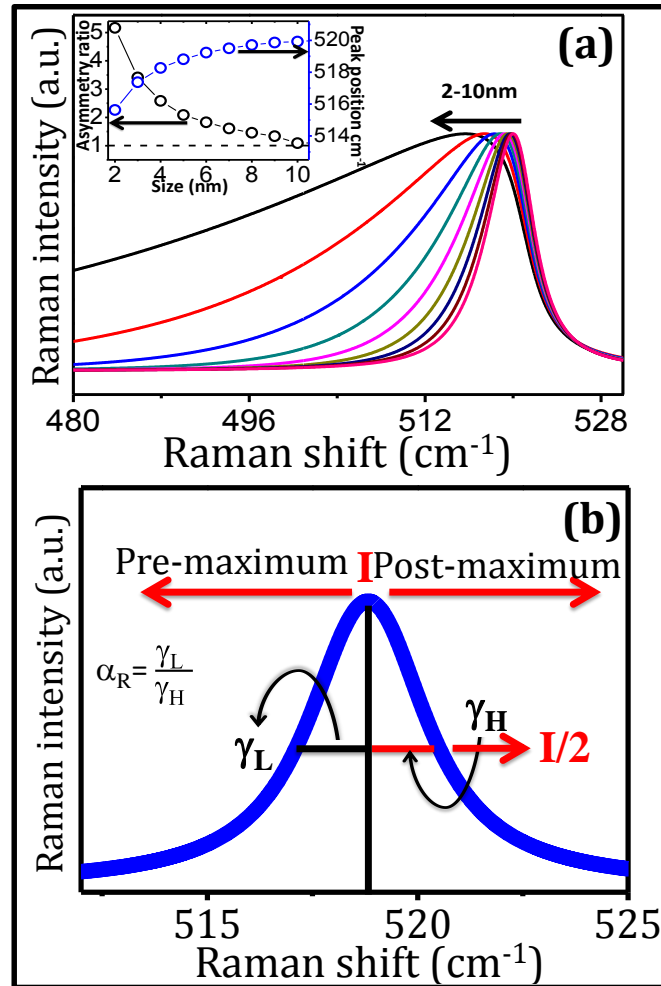


Figure 5.4: (a) Raman line-shapes theoretically generated using PCM Eq. 5.11 for different Si NSs sizes. Inset shows the asymmetry ratio (left Y-axis) and peak position (right Y-axis) with respect to size of Si NSs.(b) depicted pre-maximum & post maximum sides in Raman line shape and the half widths in lower energy side (γ_L) and higher energy side (γ_H) at $I/2$ i.e. at 50% of the total intensity I .

To further confirm the asymmetric line shape and shift in peak position the asymmetry ratio and peak position have been calculated using Figure 5.4(a) and plotted as a function of size of Si NSs which is displayed in inset of Figure 5.4(a). It is evident from inset of Figure 5.4(a) that as the size of Si NSs decreases from 10nm to 2nm then the value of α_R increases or the Raman line shape become more asymmetrically broadened with respect to its bulk counterpart. It is also appreciated from the same inset of Figure 5.4(a) (blue data points)

that the peak position get more red shifted for smaller Si NSs. The peak is shifted gradually from 520 cm^{-1} to 515 cm^{-1} for 10 to 2nm Si NSs respectively [62,63]. However most widely used, the PCM, discussed above, is not the only model used for Raman analysis. A modified phonon confinement model [174] is also used in this context though with limited acceptability due to its demerits as discussed below.

5.2.3 Modified Phonon Confinement Model

To understand the Raman scattering of NSs more closely a comparative analysis of two Raman line-shape functions has been carried out to validate the true representation of Raman line shape attributed from semiconductor NSs. It is the well-established framework that the origin of the asymmetry in Raman line-shape in low dimensional materials is the relaxation in the zone-center phonon selection rule and confinement induced uncertainty in the wave vector of phonons. This is done by appropriately choosing weighing functions and integration limits on the wave-vector (Eq. 5.11). Due to limited information regarding the exact shape, size and size-distribution it is not always easy to use an unambiguous weighing function thus result in discrepancy between theoretical Raman line-shape and experimentally observed Raman scattering spectra. Besides certain disadvantages, the PCM has been used as the most widely used formulation when it comes to the interpretation of the Raman scattering results obtained from low dimensional semiconductors especially elemental ones.

In recent attempts to simplify complicated nature of the PCM, Jia *et al.* [174,186] proposed a different approach to estimate size from Raman scattering data. However, Faraci *et al.* [174] argued that the approach used in PCM is only observing a single phonon wave vector, which was not convincing and they proposed a wave packet which covers the entire size of NSs. Therefore in a modified model, a confinement function which is a weighted superposition of sinusoidal waves, is considered [174,186] which is given in Eq. 5.8 and

represented it as following Eq. 5.15.

$$C_n(r, D) = \begin{cases} \sum_n \frac{\sin(k_n r)}{k_n r}, & r \leq \frac{D}{2} \\ 0, & r > \frac{D}{2} \end{cases}, \quad (5.15)$$

where $k_n = \frac{n\pi}{D}$, $n = 2, 4, 6, \dots, n_{max} < \frac{2D}{a}$; D is diameter of semiconductor nanowire ; a =lattice constant of the material. The corresponding Fourier coefficient is given in Eq.5.16:

$$|C_n(\vec{k})|^2 = \left| 3 \frac{\sin(\frac{kD}{2})}{\pi^3 D^3 \vec{k} (k_n^2 - \vec{k}^2)} \right|^2, \quad (5.16)$$

The form in Eq. 5.15 has components centered at $r = 0$, which vanishes at the boundary of nanocrystals. Furthermore only first component of Eq. (5.15) (i.e $n = 2$) is appropriate for simulation of Raman active mode in semiconductor NSs [187]. The range of phonon contributing to the scattering process lie only in the range of $[\frac{n\pi-1}{D}, \frac{n\pi+1}{D}]$, in case of new model used for the semiconductor NSs, due to momentum conservation [174,187]. The modified phonon dispersion relation used for the above condition is given by Eq.5.17.

$$\omega'(q) = 521 \left(1 - 0.23 \left(\frac{q a}{2\pi D} \right)^2 \right), \quad (5.17)$$

The resultant Raman line-shape in the MPCM is given as following Eq. 5.18.

$$I(\omega) \propto \rho(\omega) \frac{1}{\pi D^3} \times \int_{\frac{2\pi-1}{D}}^{\frac{2\pi+1}{D}} \frac{4\pi(qD)^2 \left| 3 \frac{\sin \frac{qD}{2}}{\pi^3 q D \{4\pi^2 - (qD)^2\}} \right|^2 \left(\frac{\gamma}{2}\right)}{[\omega - 521(1 - 0.23 \left(\frac{qa_{sl}}{2\pi D}\right)^2)]^2 + \left(\frac{\gamma}{2}\right)^2} dq, \quad (5.18)$$

where $\omega'(q)$ is the new dispersion relation which covers the entire size range of the NSs (Eq. 5.17) and $\rho(\omega) \sim \frac{n(\omega)+1}{\omega} = \frac{(\exp(h\omega/kT)-1)^{-1}+1}{\omega}$ is the Bose-Einstein occupation function.

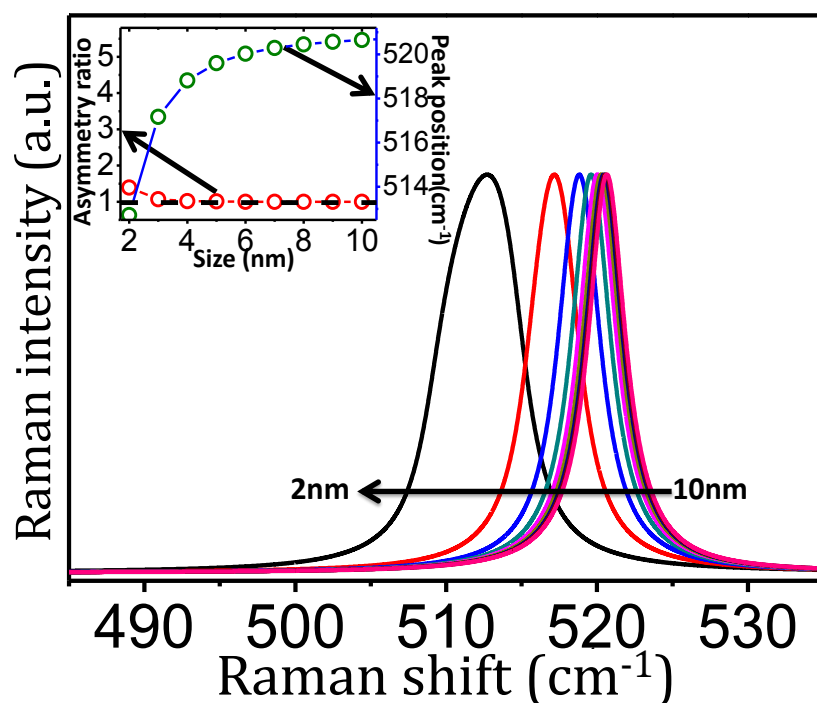


Figure 5.5: Raman line-shapes obtained using modified PCM(Eq. 5.18) for different nano crystallite sizes. Inset shows the variation of asymmetry ratio (left Y-axis) and peak position (right Y-axis) with respect to size of Si NSs.

The theoretical Raman line shape have also been generated using the MPCM (Eq. 5.18) for Si NSs as shown in Figure 5.5 [174,186,188], for different crystallite size of Si by considering one dimensional confinement. It is evident from Figure 5.5 that as the size of Si NSs decreases the Raman peak shows red-shift. From above discussion it is clear that there are three key observations, which are used to identify presence of confinement effect in Si, are red-shift, the non-unity value of α_R and the broadened Raman line shape as compared to its c-Si counterpart. It is evident from Figure 5.5 that as the size of Si NSs decreases from 10 nm to 2 nm the Raman line shapes do exhibit red shift with respect to the c-Si. However, this observation is a must for systems with confinement effect but may also arise from other effects like stress and temperature [189,190]. if these are not accompanied by other two additional observations, the broadening and asymmetry. The broadening of the Raman line-shape is also increasing with decreasing

size but no apparent change in asymmetry is observed with decreasing size (inset of Figure 5.5, right Y-axis). The symmetry of the Raman line-shape remains intact even for NSs size of 2 nm which is far below from the Bohr's exciton radius of Si. This is very unusual Raman spectral line-shape from Si NSs of sizes less than 10 nm. Thus Eq. 5.18, though has merits, does not seem to be the true representative of a typical Raman spectral line-shape for Si NSs.

5.3 Raman Spectroscopy from Si NSs Prepared by MIE

Raman spectroscopy has been used to understand the phonons' behaviour in Si NSs prepared by MIE as reported in chapter 3 (Table 3.1). The analysis has been done within the framework of PCM-

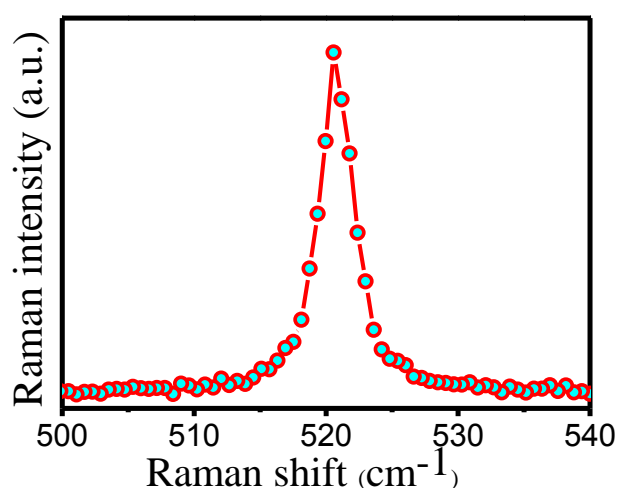


Figure 5.6: Raman spectrum from c-Si recorded using photon energy of 2.54 eV.

including estimation of size of the Si NSs. Figure 5.6 shows first order Raman spectrum from the c-Si recorded, for reference, using 2.54eV excitation energy. Figure 5.6 show a sharp, symmetric Raman spectrum with peak position at 521 cm^{-1} and FWHM of 4 cm^{-1} corresponding to the zone centered optic phonon. Raman spectra of Si NSs samples N^{*} and $N^{\$}$ (n-type Si, Table 3.1) are shown in Figure 5.7. These Raman spectra (discrete points) are asymmetrically broaden and red shifted as compared to the Raman spectrum of c-Si (Figure 5.6) giving an indication of presence of phonon confinement effect.

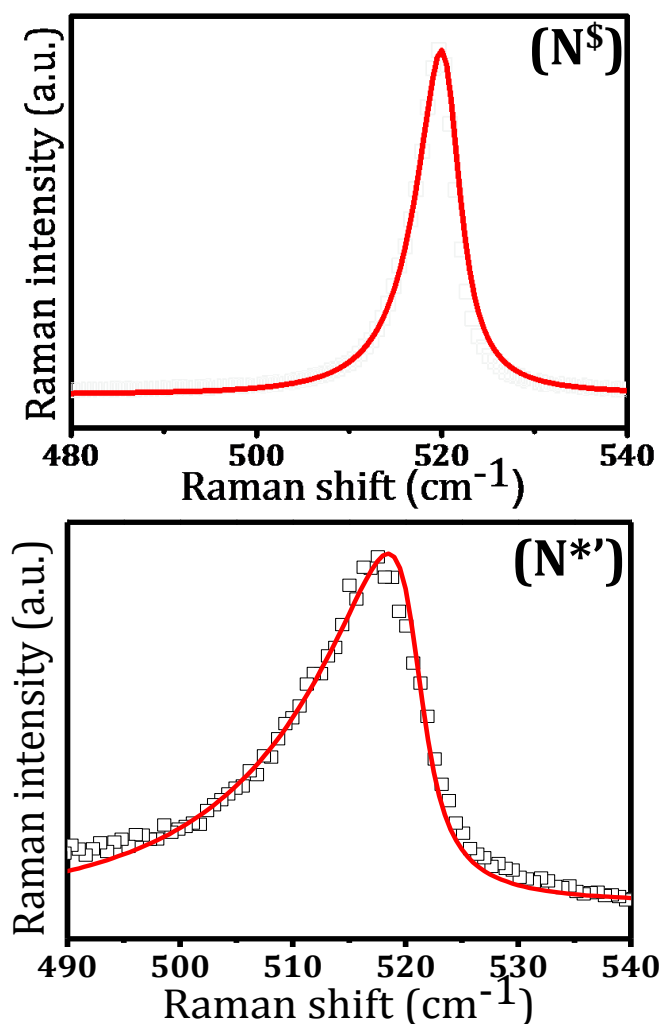


Figure 5.7: Raman spectra of Si NSs of sample N^{\$} and N^{*'} for etching time 60 minutes. The experimental data are shown by discrete data points whereas theoretical fitting using Eq. 5.11 is shown as continuous solid lines.

In order to validate the presence of phonon confinement in the Si NSs the Raman spectra (experimental data) have been fitted by the PCM model using Eq.5.11 by varying the value of L (try to minimize the deviation of theoretical line from experimental data i.e. for minimum error). The solid lines in Figure 5.7 show the theoretical Raman line shape corresponding to the best fit. It is evident from Figure 5.7 that the theoretically generated Raman line shape using PCM model shows good agreement between experimental data and theoretical data. The size (L) obtained by fitting of Raman spectra using PCM is given in the Table 5.1 (first two rows shows the size calculated from Figure

5.7).

Table-5.1: Sizes obtained by fitting the experimental Raman scattering data of Figure. 5.7 and 5.8 .

Sample name	Etching time (minute)	L(nm)
N [*]	60	3nm
N [§]	60	10nm
P [*]	60	6nm

Similarly, experimental and theoretical Raman spectrum from sample P^{*}, prepared from p-type Si wafer is shown in Figure 5.8 which is also asymmetrically broaden and red shifted as compared to the Raman spectrum of its bulk counterpart i.e. c-Si.

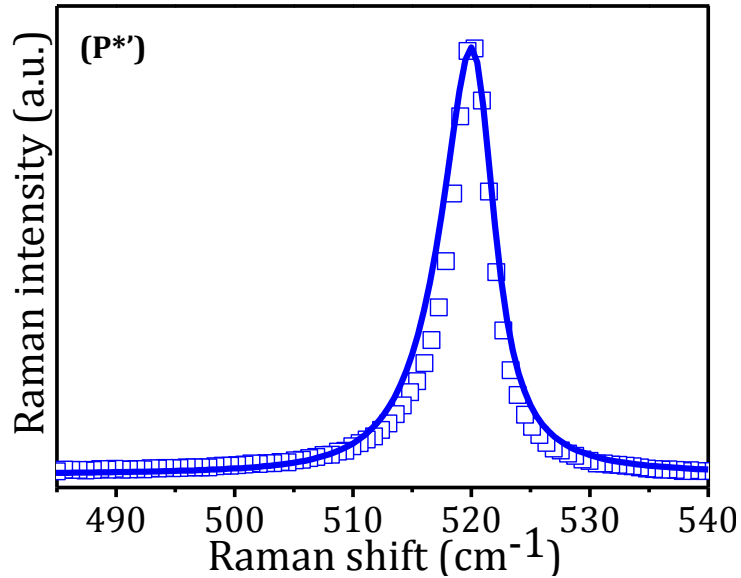


Figure 5.8: Raman spectrum from sample P^{*} (p-type Si NSs, etching time 60 min). The experimental data are shown by discrete data points whereas theoretical fitting using Eq. (5.11) is shown as solid lines.

These findings and good agreement between theoretical (Eq. 5.11) and experimental line-shapes confirms the presence of phonon confinement effect in p-type Si NSs too. The particle size and fitting parameters obtained by fitting the Raman line shape (solid lines in Figure 5.8) using Eq. 5.11 is given in the last row of Table 5.1 for p-type Si NSs. The size of Si NSs obtained using theoretical fitting for all samples is in consonance with the sizes estimated using TEM images. Figures 5.7

and 5.8 clearly show an agreement of experimentally observed Raman scattering data with the line-shape function predicted by PCM (Eq. 5.11). In contrary, the Raman line-shape predicted by MPCM (Eq.5.18) fails completely to explain the experimentally observed Raman data from Si NSs samples as big mismatch between the two can be seen in Figure 5.9.

It is very clear from above discussion that the MPCM does not represent the actual Raman scattering phenomenon taking place from low dimensional Si whereas PCM still appears to be the most generalized form for representation of the Raman line-shapes. The reasons for the incompleteness of Eq. 5.18 include the non-consideration of the participation of absolute zone-centre phonons in the Raman scattering from Si NSs. Rather MPCM considers that the zone centre of the phonon dispersion gets shifted due to finite size similar to the shifting of the band edge as discussed in the context of size dependent band gap enhancement in Si NSs.

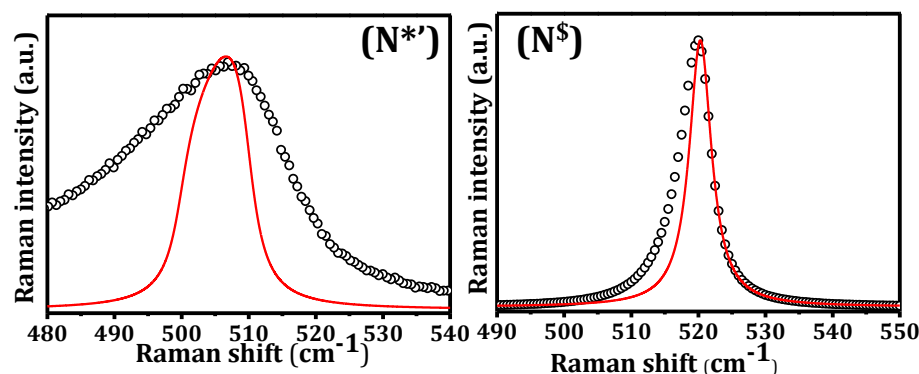


Figure 5.9: Raman spectra of Si NSs of sample N^* and $N^\$$ for etching time 60 minutes. The experimental data are shown by discrete data points whereas theoretical fitting using MPCM (Eq. 5.18) is shown as continuous solid lines.

It is worth mentioning here that, considering the shift of the phonon dispersion zone centre all-together sounds a nice approach for explanation of Raman line-shapes at nanoscale but at the same time appears incomplete. Another interesting observation with respect to MPCM is the resemblance of generated Raman line-shape with Raman spectra observed from *a*-Si. A close analysis for suitability of MPCM

for explaining *a*-Si Raman spectra can be carried out and the same has been discussed below.

5.4 Raman Spectroscopy for Quantification of Short Range order in Amorphous Si

The Raman spectrum of *a*-Si, very different from that of c-Si [62], shows a broad peak around 480 cm⁻¹ which is also accompanied by another small peak near 150 cm⁻¹ [184,191] making the spectrum a distribution of Raman scattering signal spread asymmetrically across a wide range of energies. It happens because the order of crystallinity becomes really short and is restricted in each of the grain boundaries. Due to this the vibrational modes of the Si has an influence from a density of the phonons instead of a single phonon as in the case of c-Si. Another typical nature of Raman spectrum from *a*-Si is inconsistency in its peak position as it can appear between anywhere between 475-490 cm⁻¹ [184,192,193] depending on the method of preparation giving rise to a different, and unknown, phonon arrangement at microscopic level in a given sample.

Different amorphous material samples are different from one another by means of their extent of short-range order thus give different Raman signature. It would be interesting to know the connection between the Raman spectral behaviour and the short range present, if any. Keeping this mind, Raman spectra from three different *a*-Si samples have been studied (sample details available in Table 3.4, chapter 3). Figure 5.10 shows Raman spectra from *a*-Si sample reported by Al-Salman R. et al [184], Lopez T. et al. [183] and Kumar et al. [150] (discrete points) named as samples AS1, AS2 and AS3 respectively.

The common broad band around 480 cm⁻¹ dominates in Raman spectra of *a*-Si in all the samples with Raman peaks and observed FWHM summarized in Table 5.2 below along with other parameters as will be discussed later. For comparison, typical Raman line-shapes from c-Si and nanocrystalline Si are shown in the insets (Figure 5.10). It can be appreciated from the insets that a well-defined Raman line-shape functions can define the Raman scattering profile from crystalline and

nanocrystalline Si as discussed in section 5.2.1 and 5.2.2. Just to mention, a pure Lorentzian function (Eq. 5.14) represents the Raman line-shape from c-Si whereas, a rather comprehensive equation, obtained by incorporating various factors that affect the Raman scattering including nanocrystallite size, is used to explain the asymmetric Raman line-shape for Si NSs.

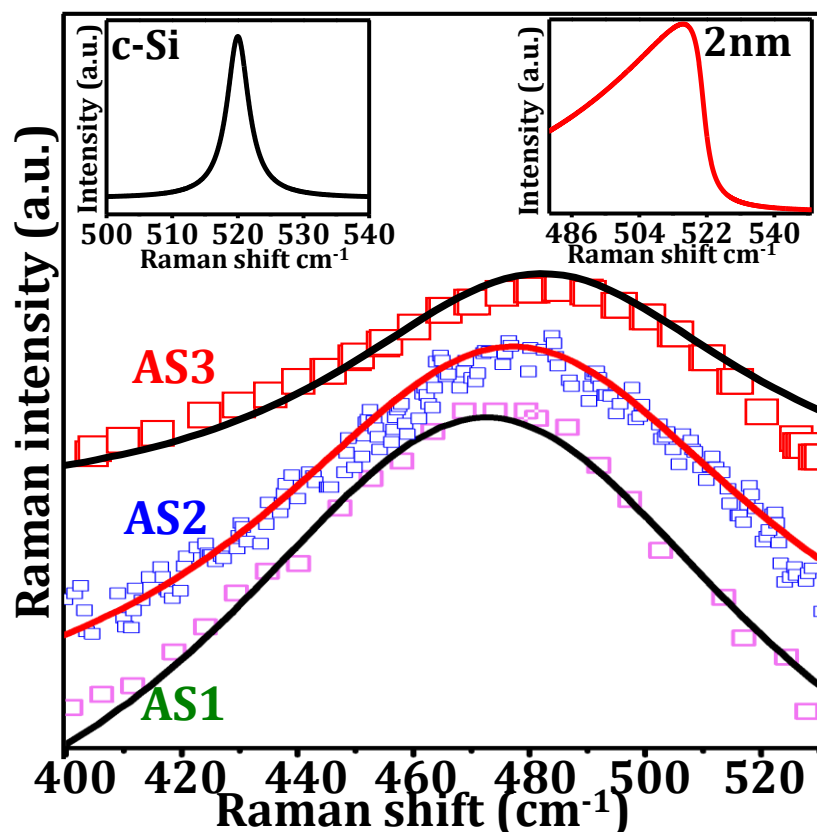


Figure 5.10: Raman spectra of *a*-Si samples AS1, AS2 and AS3. Left and right insets show the theoretical Raman line shapes of c-Si and Si NSs respectively.

To understand the line-shape of the broad Raman spectrum from *a*-Si (Figure 5.10), following approach can be adopted keeping in mind how photon will scatter from available phonons in a material. Unlike c-Si or Si NSs, *a*-Si does not contain phonons with well-defined wave vectors and thus the phonons are not ordered rather are random with no assigned momentum vector to it. This disorder is expected to get reflected in Raman scattering and the corresponding spectral line-shape will be a manifestation of the average sum of all these random phonons

present in *a*-Si. This process is represented pictorially in Figure 5.11(I) where ‘ ω_a ’ represents the summation (all random phonons available) sign. In contrast, phonons in crystalline & nanocrystalline Si can be considered to be organized. The case of c-Si has been represented pictorially in Figure 5.11(II) where a photon of frequency ‘ ω_i ’ results in another photon of frequency ‘ ω_s ’ after undergoing Raman scattering from single frequency (ω_c) phonons corresponding to zone center phonon of frequency ‘ ω_0 ’. On the other hand, a nanocrystalline material allows all phonons, arranged throughout the phonon dispersion curve[99], to participate in Raman scattering thus resulting in a line-shape as shown in right inset of Figure 5.10.

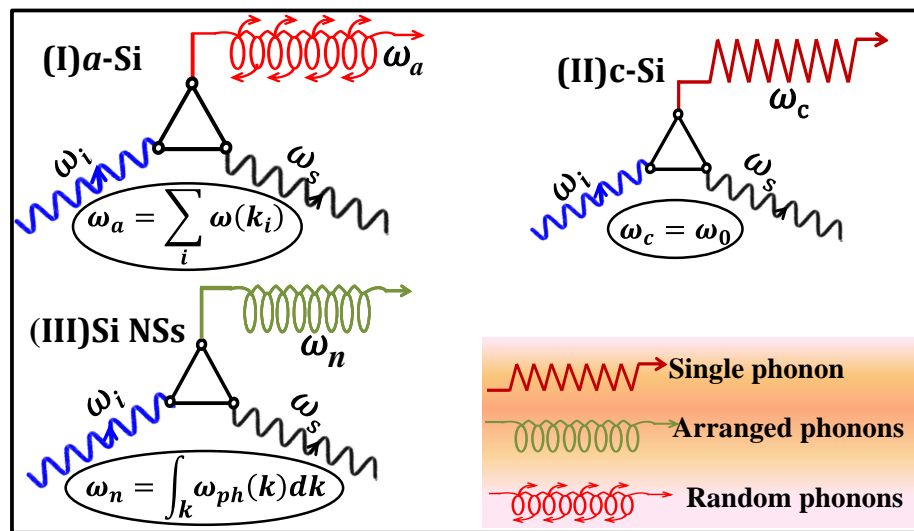


Figure 5.11: Illustration for depicting various Raman processes involving the scattering from c-Si, Si NSs and *a*-Si.

Raman scattering of a photon from these arranged phonons in a poly/nanocrystalline Si is shown pictorially in Figure 5.11(III) where ‘ ω_n ’ represents the integral sum of all phonons available on the phonon dispersion curve with all possible wave-vectors (k) [90,91,173]. So far there is no such theoretical model to explain the features of Raman line shape from *a*-Si. Also the variation of peak position in the different samples of *a*-Si might have some underlying physics which is not yet been explained appropriately. One of the most important aspects for *a*-Si is the study of its short range order.

However, phonons can be thought of being confined in *a*-Si like the

ones in Si NSs, but this hypothesis driven line-shape equation obtained using PCM (Eq. 5.11) does not explain the broad asymmetric Raman line-shape from *a*-Si thus requiring an alternative line-shape function as it fails to yield a broad asymmetric Raman line-shape even for very low sizes of nanoparticle. Alternatively, the modified PCM or MPCM [174,188] was tried for the same as given in Eq. 5.18. It is worth mentioning here that the MPCM is not correct enough to explain the Raman spectra from nanocrystalline Si as it fails completely to explain the size dependent asymmetry [62,182]. A size dependent spectral behaviour obtained using Eq. 5.18 has been used to fit the Raman scattering data for samples AS1 to AS3.

The theoretical fitting have been done by suitably choosing the value of 'D' in Eq. 5.18 is shown as solid lines (Figure 5.10). The best fit lines in Figure 5.10 are obtained by varying the size D. Values of D corresponding to best fit has been summarized in Table 5.2 below along with other Raman spectral parameters. A good agreement between the experimental data and theoretical line-shape indicates that Eq.5.18 may be used for spectral line-shape representation for Raman scattering data from *a*-Si. Another very significant advantage of using Eq. 5.18 is related to the quantification of disorder in the sample and will be discussed later. It is very conclusive from Table 5.2 and Figures 5.10 that Eq. 5.18 can successfully represent three different Raman data sets obtained from three *a*-Si samples prepared by three different methods by three different researchers.

It can be appreciated from Table 5.2 that the Raman peak shifts as a function of the size parameter D [194]. One should be very cautious in interpreting the term 'D' by saying it the "nanocrystallite size", as it is traditionally named, may be a misleading term in the context of amorphous materials. Since the amorphous materials are characterized by the term short range order and the Raman spectrum obtained is a resultant of scattering from the phonons existing within this short range order distance it would be appropriate to use the term D for this distance. In other words, the term D, obtained from Raman spectral analysis, can be used to quantify this short range order in *a*-Si.

Table 5.2: Raman parameters calculated from fitting of Raman spectra of AS1, AS2 and AS3 with Eq. 5.18. Values of D in the bracket in last column are the sizes estimated using Eq. 5.19.

Sample	Raman peak position (cm ⁻¹)	FWHM (γ) (cm ⁻¹)	Short range order D (Å)
AS1	477	108	8.3, (8.5)
AS2	480	100	8.8, (8.8)
AS3	482	80	9.3, (9.0)

Another important observation from the above analysis is the dependence of Raman peak position on the size parameter D as evident in Table 5.2. This behaviour is similar to the size dependent red shift observed from Si NSs when analyzed within the framework of BPM [178] as given by Eq. 5.19. Figure 5.12 shows the theoretically generated curves using Eq. 5.19 showing the Raman shifts due to the confinement for different Si structures as a function of size of Si.

$$\Delta\omega = -\xi \left(\frac{a}{D}\right)^\delta, \quad (5.19)$$

where ‘*a*’ is the lattice parameter and D is the nanocrystallite size for Si NSs and δ governs the size dependence of red shift in term of peak position as compared to the c-Si counterpart and depends on the shape of the nanoparticles. Zi *et al.* [178] proposed a δ value of 1.08 and 1.44 for columnar and spherical Si nanoparticles respectively. The parameter, ξ , is used to explain the confinement of phonons and takes the value of 20.92 cm⁻¹ and 47.41cm⁻¹ for columnar and spherical nanocrystals respectively [178]. The behaviour of Eq. 5.19 is shown in Figure 5.12 for the columnar (red curve) and spherical (green curve) nanoparticles whereas the dotted straight line is shown to represent a Raman shift value of 480 cm⁻¹ around which the typical Raman peak lies for *a*-Si.

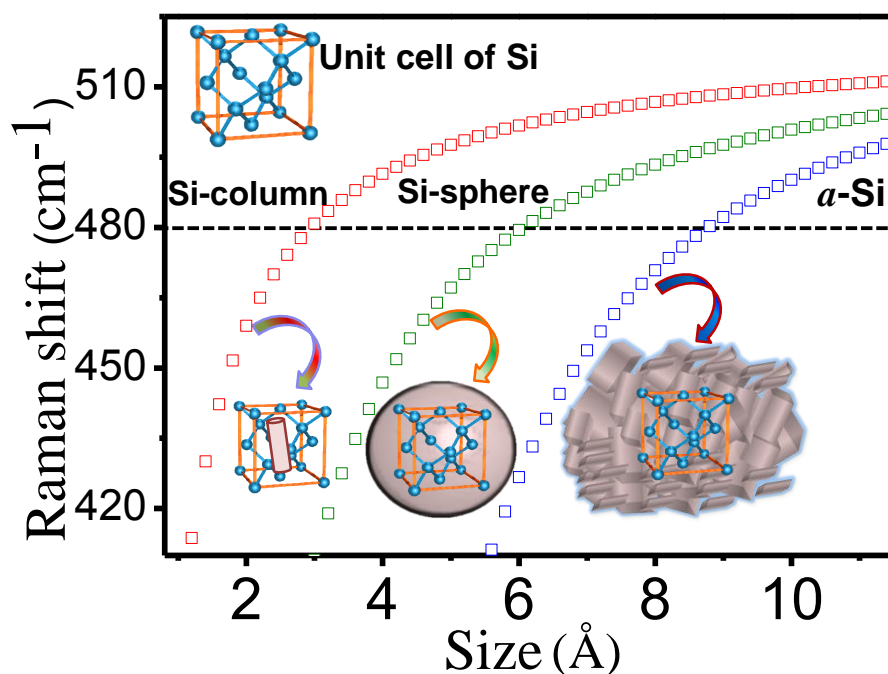


Figure 5.12: Theoretically simulated curves of Raman shift vs size for Si sphere, column and *a*-Si. The red, green and blue data points correspond to the calculated results for column, sphere and *a*-Si respectively. The pictorial representation corresponds to the shape used to calculate the curve of *a*-Si.

If one hypothesizes that the short range order is having a spherical or columnar shape, a (pseudo-)crystallite size of 6.1 Å and 2.9 Å respectively will be obtained. It means that if this (pseudo-)crystallites are columnar in shape, its size will be only 2.7 Å which will only be able to fit couple of Si atoms (nearest distance \sim 156 pm) whereas for spherical crystallite the size will be 5.6 Å which is only sufficient to fit a single unit cell of Si (lattice constant \sim 5.43 Å). Both of these situations lead to a thermodynamically impossible conclusions thus proving the hypothesis wrong [187]. It means that the ξ and δ values proposed by Zi *et al.* [178] can't be used if one wants to estimate the size of (pseudo-)crystallite, or the distance of short-range order, present in *a*-Si using Raman peak position.

Looking at the similarity between the size dependent peak shift behaviours of Si NSs and *a*-Si, a third set of ξ and δ value is proposed here to be used exclusively for *a*-Si. The size dependent Raman shift

function (Eq. 5.19) with $\xi = 117 \text{ cm}^{-1}$ and $\delta = 2.21$ is also plotted in Figure 5.12 (blue curve). The estimated size using these values comes out to be 8.5 \AA for Raman spectrum centered at 477 cm^{-1} which is approximately equal to the size obtained by fitting for sample AS1. This size is reasonable as it may contain more than 160 unit cells of Si making it thermodynamically viable. Similarly, sizes have been estimated for samples AS2 and AS3 and obtained to be 8.8 and 9.0 \AA respectively which is in the same range as obtained using the fitting (Table-5.2) [194]

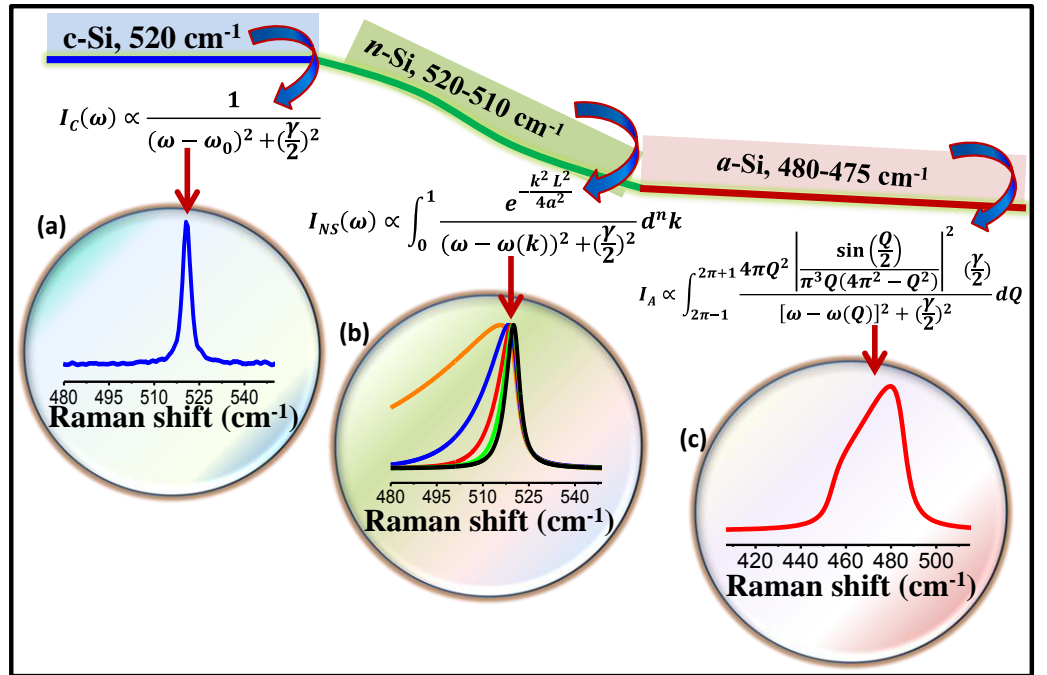


Figure 5.13: Theoretically obtained Raman line shapes for (a) c-Si, (b) SiNSs and (c) *a*-Si displayed in the different circles. The schematic (blue, green and red line on the top of Raman line shape) shows the abrupt transition from c-Si to *a*-Si.

A comparison between the sizes estimated using the two approaches, the fitting with the line-shape and the empirical equation, reveals that Eq. 5.19 can be used universally to estimate short range order present in *a*-Si by looking at the peak position of the Raman spectra. This will help in quantifying the disorder present at microscopic level in *a*-Si prepared by any method. The above mentioned discussion can be summarized in a nutshell by consolidating the line-shape representations for Si in its crystalline, nanocrystalline and amorphous

phases as follows.

Raman line-shape from *c*-Si is a typical Lorentzian function and represented by one to result in a sharp symmetric line-shape centered at zone centered phonon frequency and show no size dependent peak shift as represented in Figure 5.13(a) along with the Eq. A shape and size dependent Raman line-shape asymmetry, red-shift and broadening is a typical behaviour of Raman spectra obtained from Si NSs as represented by a spectral line-shape functioned worked out within the framework of PCM (Eq. 5.11) as shown in Figure 5.13(b). Above mentioned two regimes of Si phases are well discussed in contrast to the *a*-Si phase in the context to Raman spectral line-shape representation. An asymmetric Raman line-shape obtained from *a*-Si can be successfully represented by MPCM and can be used to estimate short range order distance using Eq. 5.18 as shown in graphics in Figure 5.13(c). A spectral line-shape (Eq. 5.18) and empirical relation (Eq. 5.19) is capable of quantifying the distance upto which the order of crystallinity is intact in *a*-Si.

5.5 Summary

In summary, the PCM and MPCM have been discussed here in the context of observed asymmetrically broadened and red-shifted Raman spectrum from Si NSs prepared by MIE. The PCM, was found to be most suitable framework to estimate the size of Si NSs. The Si NSs fabricated using the MIE technique were found capable of showing quantum confinement effect. The MPCM fails to explain the observed asymmetry in the Raman scattering data of Si NSs but it can be used to represent experimental Raman spectrum obtained from *a*-Si. The line-shape obtained using MPCM is validated by fitting three different sets of *a*-Si Raman scattering data obtained by three different research groups from *a*-Si samples prepared by three different methods. The Raman peak position is observed to be depending on a size parameter and has been used to quantify the distance of short range order present in *a*-Si. As an extension, an empirical relation between the short range order and Raman peak position has been proposed to be used as a

handy tool for quantification of short range order. This relation, obtained based on BPM, seems to be universal in nature for quantification of short range order and can be used for *a*-Si prepared by any method.

Chapter 6

Fano Resonance and Fano-Scattering in Silicon Nanostructures

In this chapter, interaction of electronic continuum with optic and acoustic phonons is investigated in crystalline as well as nanocrystalline Si using Raman spectroscopy. Raman spectral asymmetries induced by electron-optic phonon interaction (Fano resonance) and its interplay with quantum confinement has also been discussed for Si NSs. A phenomenon, named as Fano scattering, where acoustic phonons were found to interact with appropriate electronic continuum is also reported using Raman spectroscopy. A recipe has been proposed to extract contribution of the electronic Raman scattering from Raman scattering spectrum of Si NSs. Results presented in this chapter are published in the literatures.⁴

6.1 Electron-Optical Phonon Interaction: Fano Resonance

Generally, a resonance is thought to be an improvement of the response of a system to an external excitation at a specific frequency. It is referred to as the resonant frequency or natural frequency of the system. In many classical textbooks a resonance is introduced by the means of a harmonic oscillator with periodic forcing. When the frequency of the driving force is close to the natural frequency of the

⁴ Priyanka et al. *J. Phys. Chem. C*, 2017, 121 (9), 5372–5378,
Priyanka et al. *J. Phys. Chem. Lett.* 2016, 7 (24), 5291–5296,
Priyanka et al. *Phys. Chem. Chem. Phys.* 2017, 19 (47), 31788–31795

oscillator, the amplitude of the latter is growing toward its maximal value. Often many physical systems may also exhibit the opposite phenomenon when their response is suppressed if some resonance condition is met (this result to term named as *antiresonance*). The Lorentzian formula has been used as fundamental resonance line shape for many years, which is given by symmetric line profile and known as Breit-Wigner resonance [195]. The second resonance is characterized as asymmetric line profile and is of interest in the present chapter. In 1961, in a quantum mechanical study of the autoionizing states of atoms, Ugo Fano discovered a new type of resonance which now bears his name i.e. Fano resonance [121,196] (second resonance). In contrast to a Lorentzian resonance, the Fano resonance exhibits a distinctly asymmetric shape [197,198].

Fano resonance is the universal property of a physical system[236] which takes place in a system where a discrete energy state lies within a continuum of energy states [199–201]. Fano resonance is generally the interference of the waves associated with transitions of discrete states (lying in the continuum) and the continuum of states. As a result of Fano resonance, a characteristic asymmetric line shape is observed. As it is well known that the Fano effect is caused by interference of waves, and interference may be constructive as well as destructive, therefore resonance (due to constructive interference) and antiresonance [121] (due to destructive interference) both are simultaneously observed in the Fano spectrum. The schematic diagram in Figure 6.1 makes it easy to qualitatively visualize the Fano resonance.

This type of phenomenon may be observed in variety of systems including atoms [202], solid materials [203], molecules [204,205] as well as in nanostructure [198]etc. Semiconductors can be a typical example to see this Fano resonance because in semiconductors phonons, having discrete energies, can interact with continuum of states, which may be provided by the electronic states under special conditions like heavy doping on quantum confinement effect. Fano used a perturbation method to explain the appearance of asymmetric

resonances. Fano obtained the general formula for the shape of the resonance profile [206] of a scattering cross section, which is given by Eq 6.1.

$$I_F(\omega) = \frac{(q+\epsilon)^2}{(1+\epsilon^2)}, \quad (6.1)$$

where q is the phenomenological shape or Fano parameter and ϵ is the reduced energy which is the ratio of difference in frequency to the half width of the line shape and is given by Eq. 6.2. The amplitude of ‘ q ’ provides the measure of electron phonon interaction with a smaller value of ‘ $|q|$ ’ meaning strong electron-phonon interaction.

$$\epsilon = \frac{\omega - \omega_0}{\gamma/2}, \quad (6.2)$$

Raman as well as IR spectroscopies are amongst various techniques [207–209] to study the possible Fano interaction in a system. In the present study Raman spectroscopy has been used to study the Fano resonance in c-Si and Si NSs.

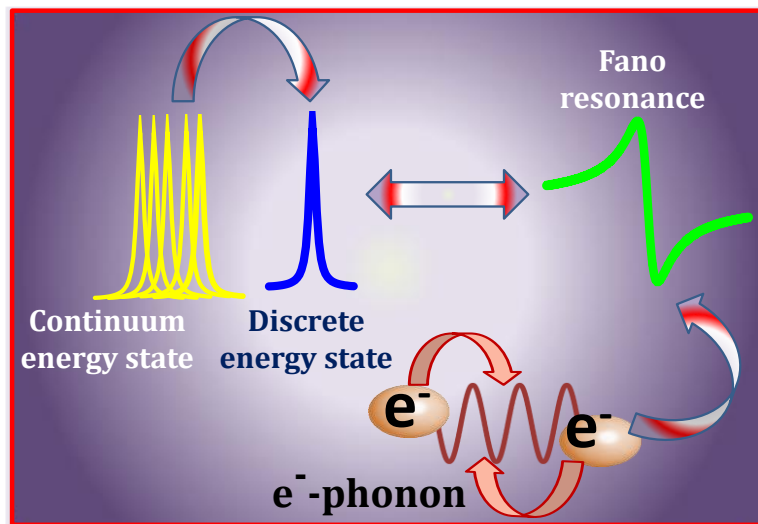


Figure 6.1: Schematic diagram representing Fano resonance.

6.1.1 Fano Resonance in Crystalline Si

In well-tailored c-Si, the electron-phonon coupling in terms of interference between electronic continuum and optic phonons results in an asymmetric Raman line-shape. Manifestation of the Fano interference is one of the well-studied properties in the heavily doped

($>1 \times 10^{19} \text{ cm}^{-3}$) Si wafer [210]. The origin of Fano resonance in semiconductors is the phonons interference with continuum of states created due to heavy doping [211,212] or photoexcitation [213]. The asymmetry of Raman line-shape depends on the doping type if induced by Fano resonance. In heavily doped p-type semiconductor, electronic continuum is created in valence band due to transition of light hole to heavy hole [120] while created in conduction band in case of heavily doped n-type [97]. Fano resonance resulting from interference between discrete phonon and valence band electronic continuum (in n-type system) produces asymmetric broadening in a way that lower half width (γ_L) is more than the higher half width (γ_H) in the Raman spectrum while in p-type (interference between phonon and valence band continuum) it is other way round.

As a result, any of the spectral half widths, towards lower- or higher-frequency side, of the Raman peak may dominate over the other. Figure 6.2 shows the Fano Raman line shapes expected from heavily doped (Figure 6.2a & 6.2b) and undoped c-Si (Figure 6.2c). The Raman line-shape asymmetry, often characterized by asymmetry ratio $\alpha_R = \frac{\gamma_L}{\gamma_H}$ (Figure 6.2c), can be observed for doped Si whereas a unit value of α_R results when the line is symmetric as in the case of c-Si. A Fano Raman line-shape from heavily doped p- and n- type c-Si gives an α_R value of less than one (<1) and more than one (>1) respectively as the lower half width is less than the higher half width for a p-type semiconductor whereas it is other way round for an n-type system. It is also important to mention here that Fano resonance is an interference which must possess constructive as well as destructive interference. In Fano Raman line-shape it is manifested as an antiresonance dip (destructive interference, minimum spectral intensity) which is not observed in Raman line-shapes where Fano resonance is absent or very weak (Figure 6.2). This is an important signature of presence of Fano resonance in a system. As a characteristic of Fano effect, the antiresonance dip and the wider half-width are observed in the opposite sides of the Raman peaks position [168].

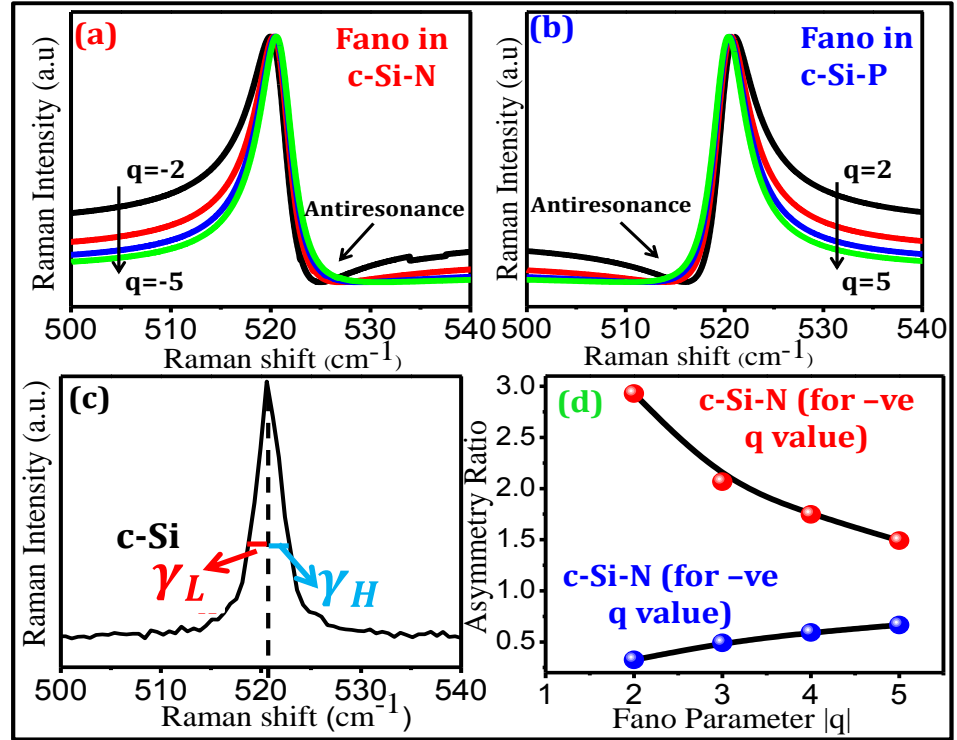


Figure 6.2: Theoretical Raman line shapes obtained using Eq. 6.1 for (a) heavily doped n-type c-Si (c-Si-N) (b) heavily doped p-type c-Si (c-Si-P) (d) Fano parameter dependent α_R for heavily doped n and p-type Si.

The theoretical Raman line-shapes, shown in Figure 6.2, have been generated using well established general Fano-Raman line shapes equation (Eq. 6.1) which takes care of Fano resonance for both n- and p-type semiconductor by appropriately choosing the sign of Fano parameter (q). Figure 6.2 (a) & (b) show the Raman line-shapes, obtained using Eq. 6.1, for different negative and positive values of Fano asymmetry parameter, q , representing a heavily doped n- and p-type c-Si system whereas Figure 6.2 (c) shows the theoretical Raman line shapes from c-Si. The variation of Fano-Raman line-shape α_R as a function of absolute values of q has been shown in Figure 6.2(d). An increase in lower (or higher) half width can be seen on decreasing the negative (or positive) value of q .

In both the cases, a deviation from symmetry is evident on increasing the Fano coupling (decreasing $|q|$ value) and α_R approaches asymptotically towards unit α_R value for infinitely large values of $|q|$

(Figure 6.2 d). It can clearly be observed that the value of α_R increases with $1/|q|$ for n-type Si and decreases for p-type Si because of the different nature of electronic continuum in n- & p-type Si [212,214]. An accompanied antiresonance dip can also be seen very clearly in Figure 6.2(a) & (b) by slanted arrow sign. To validate above mentioned theoretical predictions, Raman line-shape analyses have been done from heavily doped n- & p-type Si wafers and compared with their intrinsic counterparts. Both the Si wafers have been chosen, in terms of doping levels, so that it qualifies the condition (having sufficient doping level) to exhibit Fano effect. Figure 6.3 shows the Raman scattering from heavily doped n- and p-type c-Si along with the low doped c-Si of both the types. The black dotted curve in Figure 6.3 shows the Raman scattering from intrinsic Si wafer (c-Si) showing the typical Lorentzian Raman line shape with peak position at $\sim 520.5 \text{ cm}^{-1}$ & FWHM of $\sim 4 \text{ cm}^{-1}$.

The Raman spectra of both the Si wafers of n-type (sample c-Si-N) and p-type (sample c-Si-P) have been recorded to check the presence of Fano resonance. Raman spectra from c-Si-N & c-Si-P are displayed in Figure 6.3. Figure 6.3(a) shows that the Raman spectrum for c-Si-N is redshifted and asymmetrically broadened where lower half width is more than the higher half width ($\Gamma_L > \Gamma_H$). On the other hand, Figure 6.3(b) shows the Raman spectrum for the c-Si-P which is asymmetrically broadened where higher half width is more than the lower half width ($\Gamma_L < \Gamma_H$).

Though the asymmetry of the Raman line-shapes from samples c-Si-N & c-Si-P are clearly evident, the α_R values has something more to say than to just show the asymmetric nature. The α_R are 1.2, which is more than one, and 0.58, which is less than one, for samples c-Si-N & c-Si-P respectively. The asymmetric Raman line shape from c-Si-N ($8.2 \times 10^{19} \text{ cm}^{-3}$ Arsenic doped; n-type; resistivity $\sim 0.001 \text{ }\Omega\text{cm}$) & c-Si-P ($1.3 \times 10^{20} \text{ cm}^{-3}$ Boron doped; p-type; resistivity $\sim 0.001 \text{ }\Omega\text{cm}$) can be attributed to Fano resonance because the doping levels are sufficiently high in these samples as this is also consistent with the available

reports.

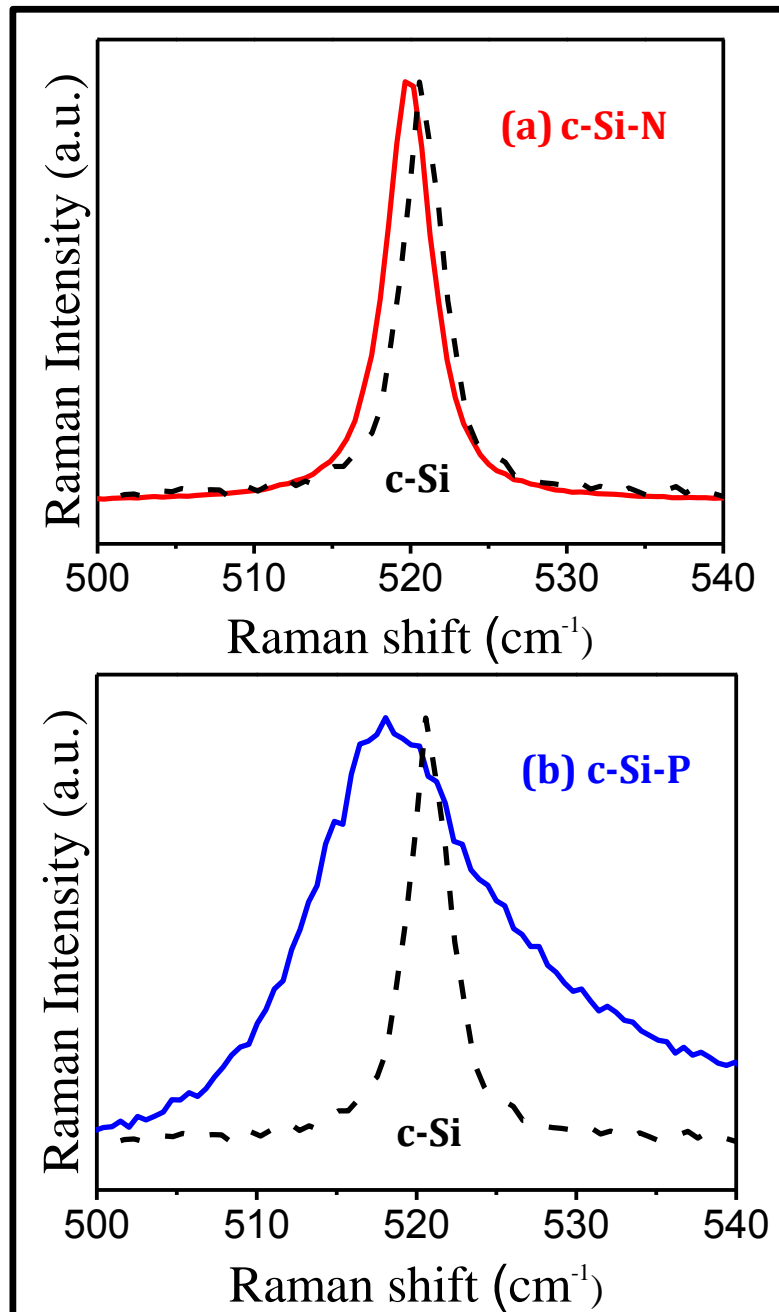


Figure 6.3: Raman spectra for heavily doped crystalline Si samples (a) c-Si-N and (b) c-Si-P along with intrinsic c-Si (dotted black line).

It has been well established from the above discussion that the Fano resonance is present in samples c-Si-N & c-Si-P. The Fano Resonance may be present in the Si NSs, fabricated from highly doped wafers which show Fano resonance. It will be interesting to see how the Fano resonance induced asymmetric Raman line-shape superimposes itself

on the already asymmetric Raman line-shape from Si NSs due to confinement effect.

6.1.2 Fano Resonance in Quantum Confined Si

As discussed above, asymmetric Raman spectral line-shapes are observed from discrete optical phonons due to quantum confinement effect. It would be interesting to see how this asymmetry is affected by the introduction of Fano resonance in the same system where quantum confinement effect is already present. Fano resonance has been observed due to inter-sub-bands transitions in semiconductor quantum wells [215]. In such systems, the phonons and the electronic excitations, participating in the Raman scattering, have discrete quantized levels due to spatial confinement. In appropriately designed semiconductor superlattices, Fano resonance of intra sub-band electronic transitions with optical phonons has also been studied. In super lattices, the conduction sub-band can be easily tailored to make it wide enough so that the contribution from the optical phonons overlap. There are several reports on laser-induced Fano resonance in the SiNWs of diameter 5-15 nm [213]. Gupta et al. [215] fitted their experimental Raman scattering data using the asymmetric Fano line-shape of the c-Si (Eq. 6.1) without considering any quantum confinement effect. This is not possible for low dimensional materials where quantum confinement is inherent in the system. The interplay between Fano and quantum confinement effects is debatable unless it is investigated clearly. All the reports on Fano interaction in the Si NSs lack a clear theory as well as experiment on the mechanism of electron-phonon interaction. There are attempts to investigate the presence of Fano interaction in low dimensional systems. Still an in-depth study is required regarding the issues related to Fano interaction in the Si NSs, its implications and dependence on other parameters like size of the NSs, excitation laser power density and temperature etc. An attempt has been made to understand the interplay between Fano and nano combine effect. A suitably designed low dimensional semiconductor to observe nano-effect with appropriate doping to

observe Fano resonance can be investigated by Raman spectroscopy. First a comprehensive theoretical Raman line shape function has been generated with appropriate modification in the general Fano line-shape to incorporate the size effect and weighting function, which have been extensively used to study this type of effect.

To see the combination of Fano and nano effects (quantum confined system) (F-C) on Raman line shape the following equation has been used, which is a well-accepted approach for this purpose [70,220,258].

$$I_{FL}(\omega) = \int_0^1 \exp(-k^2 L^2 / 4a^2) \frac{(q+\varepsilon')^2}{1+\varepsilon'^2} d^n k, \quad (6.3)$$

where $\varepsilon' = [\omega - \omega(k)]^2 / (\gamma/2)^2$ the $\omega(k)$ is the phonon dispersion relation representing optic phonons in Si and is given by $\omega(k) = [A + B \cos(\pi k/2)]^{0.5}$ with $A = 171400 \text{ cm}^{-2}$ and $B = 100000 \text{ cm}^{-2}$. 'q' is the Fano asymmetry parameter. The γ , 'L' and 'a' are the spectral width, particle size and lattice constant respectively. The theoretical Raman line-shapes represented by Eq.6.3 can be used as a general line-shape as it takes care of both the effects (Fano and nano combined effect) for both n- and p-type semiconductor nanomaterial by appropriately choosing the sign of Fano parameter (positive q for p-type material and negative q for n-type material) for a fixed value of L (size of NSs), displayed in Figure 6.4.

To study these effects, first Raman line shapes have been obtained only for nano effect in Si NSs of size 3 nm followed by inclusion of Fano resonance contribution by using three different |q| values of 5, 4 and 3. Negative values of q in Figure 6.4(a) represent how Fano resonance affects the quantum confinement effect for n-type Si NSs. When finite negative value of q is introduced, the α_R increase with $1/|q|$ (i.e, deviating away from symmetric nature) because in n-type semiconductors Fano resonance and nano-effect increases pre-maximum half width (Γ_L) without changing the post-maximum half width (Γ_H) (see Figure 6.2(c)). This results in increase of α_R more rapidly with $1/|q|$ in n-type confined system (Figure 6.4(c)).

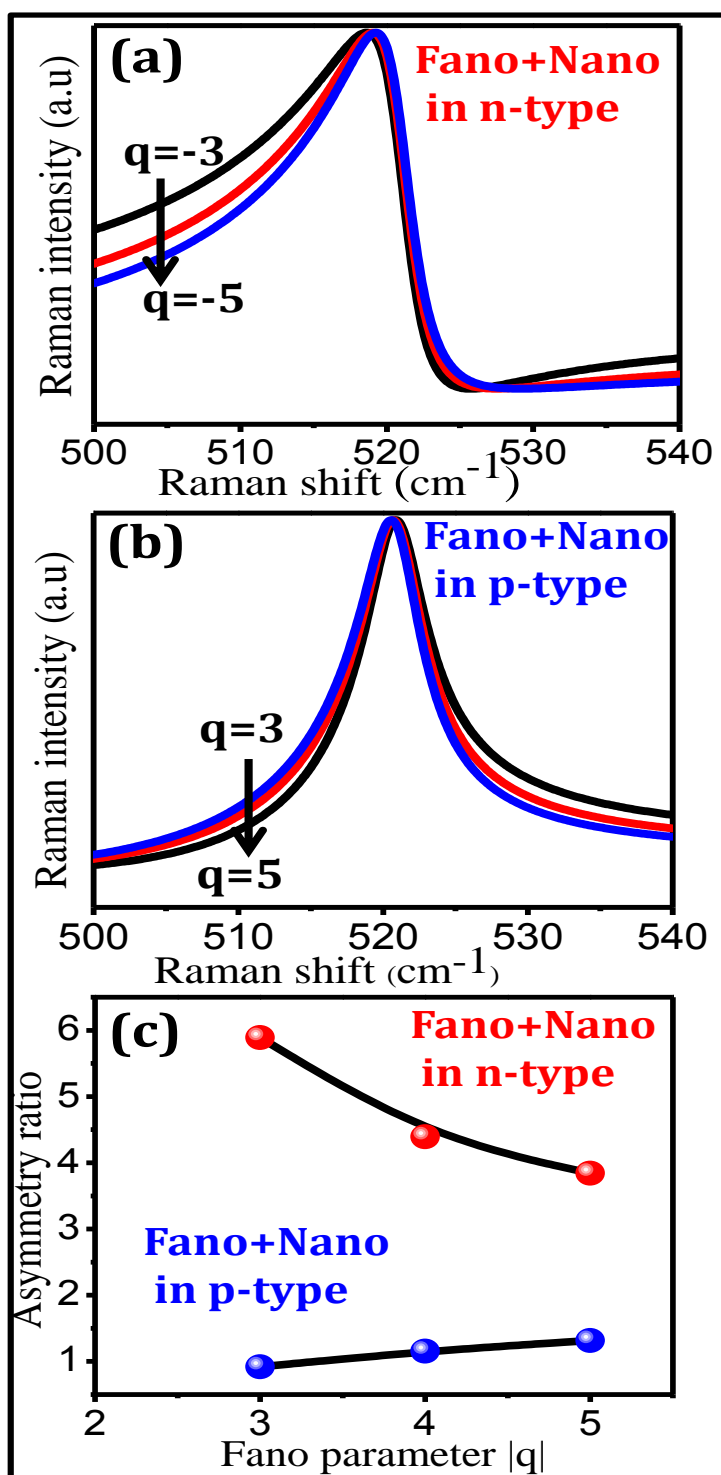


Figure 6.4: Theoretical Raman line shapes obtained using Eq. 6.3 for (a) heavily doped n-type low dimensional Si (b) heavily doped p-type low dimensional Si (c) Fano parameter dependent α_R for heavily doped low dimensional n and p-type Si.

It means that the Fano resonance adds to the already existing asymmetry for a low dimensional n-type semiconductor system. On the

other hand, Fano effect in p-type confined system induces an increase in the post-maximum half width (γ_H) without changing the pre-maximum half width (γ_L) as decided by the nanocrystallite size.

The γ_H keeps on increasing with increasing Fano coupling or decreasing $|q|$ and eventually may completely compensate the nano-effect induced lower half width. Due to this compensatory nature, the α_R approaches unity, as can be seen in Figure 6.4(c), with decreasing $1/|q|$ to result in a near symmetric Raman line-shape from a system consisting of appropriate nano-effect and Fano resonance contributions. This observed near-symmetric Raman line-shape may mislead one to be interpreted in terms of absence of either of the effect or at best to be originating due to temperature or stress effect [168].

Furthermore, disappearance of antiresonance dip (Figure 6.4b) makes the detection of Fano effect even worse and virtually impossible to be identified when present in a low dimensional p-type system. Thus Fano resonance plays a dual role for addition and compensation depending on the doping type in low dimensional semiconductor systems and hence need careful analysis of the Raman line-shape to be conclusive. In order to understand the anomaly present in the p-type highly doped semiconducting nanostructures more closely. The theoretical Raman line shapes have been generated using Eq. 6.3 for various combinations of +ve q and L value that yield unit α_R and listed in Table 6.1. The corresponding line-shapes are plotted in Figure 6.5a [61].

Table 6.1: Raman parameters calculated from the theoretically developed Raman line-shape

Size of nanostructures (nm)	Fano parameter q	Asymmetry Ratio
3	3.4	1.01
4	4.0	1.01
5	4.7	1.00
6	5.7	1.00
7	6.9	1.00

Figure 6.5(b) shows a variation of α_R as a function of Fano parameter for different NSs size calculated from Figure 6.5(a). As discussed earlier, low dimensional systems show Raman line-shape asymmetry with smaller half width in the pre-maximum side as compared to the post-maximum side irrespective of the doping type (p- or n- type). On the other hand heavily doped p-type material show Raman line-shape asymmetry with higher half width in post-maximum side when only Fano effect is present. This implies that both the effects are inducing the half widths in the opposite sides of the spectral maximum for a low dimensional p-type semiconductor.

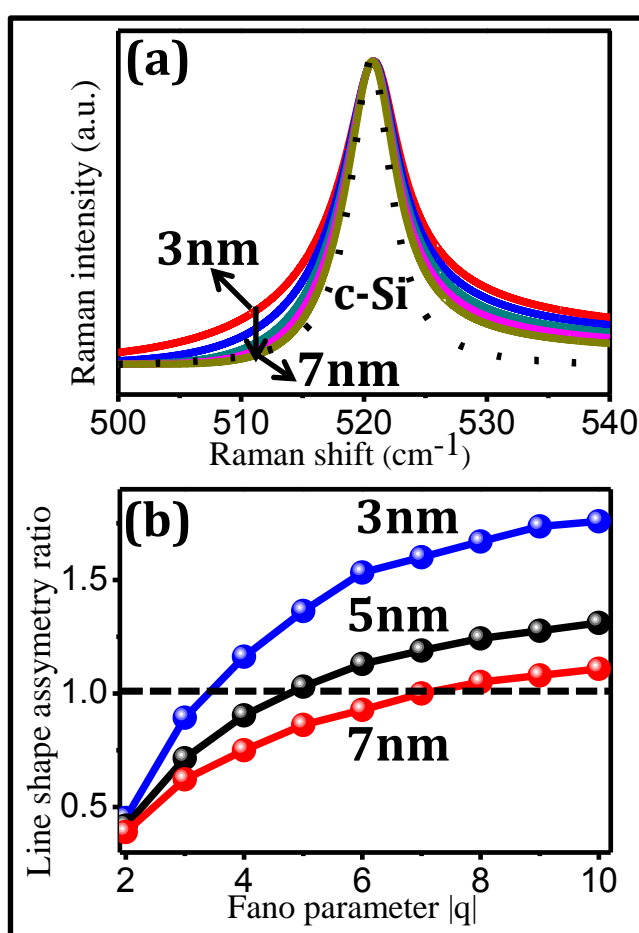


Figure 6.5: (a) Theoretically obtained Raman line shape for various combinations of q and L using Eq 6.3 (b) the variation of α_R as a function of Fano parameter q for different nanostructure sizes.

In other way the induced asymmetry (by Fano effect) in the post-maximum side is compensating the induced asymmetry in the pre-

maximum side (by quantum effect) as long as the α_R are concerned. In a situation where both the induced half widths are equal, a unit α_R will result. The combined effect in p-type SiNWs shows the strange Raman line shape, though the α_R of the Raman line shape is equal to one but still the Raman line shapes are deviated from true symmetric nature. The Raman line-shapes corresponding to these q-L pairs may be termed to be pseudo-symmetric as the half widths on either sides of the peak is not equal for other than half maximum intensity values.

From Figure 6.5(b) it can be observed that Fano effect dominates over confinement effect in smaller q region irrespective of nano crystallite size. From Figure 6.5(b) it is also observed that the variation in α_R range is not consistent as a function of size of SiNWs. For L=3 nm the value of α_R varies from 1.75 to 0.45 for q= 1 to q=10 respectively but in case of L=7 nm variation is from 1.1 to 0.38 for the same q range. This is consistent with the fact that Fano effect is strongly dependent on the size of the Si NSs [216].

6.1.3 Fano Resonance in Si NSs: Raman Scattering

The theoretical framework of Fano resonance has been discussed for c-Si and Si NSs in section 6.1.1 and 6.1.2. The constructed framework of Fano resonance for Si NSs has been validated by comparing the predicted above-mentioned Raman line-shapes with the experimentally observed Raman scattering from suitably designed Si NSs samples prepared from heavily doped n- and p-type Si wafers. It has been already discussed that the c-Si-N and c-Si-P wafers exhibit Fano effect (Figure 6.3). In order to study the Fano and Nano combined effect together the SiNWs samples (sample N[#] and P[#]) have been fabricated for this purpose mentioned in Table 3.1 in chapter 3. The samples under study must contain sufficiently thin SiNWs to show quantum confinement effect (which is confirmed from Figure 4.16 TEM images of sample N[#] and P[#]) so that any perturbation induced by Fano effect can be investigated.

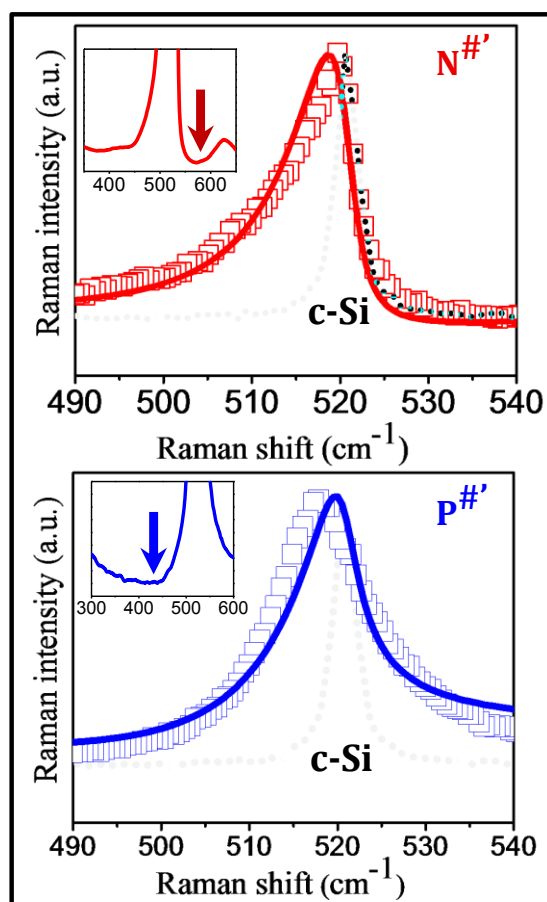


Figure 6.6: Raman spectra for sample $N^{\#}$ and sample $P^{\#}$ along with intrinsic c-Si (dotted line). Discrete points represent experimentally observed data while solid lines represent the theoretical Raman line shapes (Eq.6.3). Inset shows the corresponding Raman spectra in wider spectral range to show antiresonance (arrow marked).

The Raman spectra from samples $N^{\#}$ and $P^{\#}$, shown as discrete points in Figure 6.6, are redshifted and asymmetrically broadened as compared to the Raman spectrum of c-Si (undoped Si wafer). The α_R of Raman spectra for samples $N^{\#}$ and $P^{\#}$ are found to be 2.78 and 0.78 respectively. This trend of α_R greater than unity and lesser than unity for n-type and p-type SiNWs respectively is accompanied by presence of antiresonance dips (insets of Figure 6.6) for $N^{\#}$ and $P^{\#}$ both which signifies the presence of Fano resonance in both the samples.

Above discussion establishes that the SiNWs is suitable to show Fano resonance as well as nano-effect. Thus it will be interesting to analyze

the asymmetry in Raman line-shapes in Figure 6.6 in terms of relative contribution from the two phenomena. For complete analysis of these Raman spectra of samples N[#] and P[#], it is also necessary to compare the Raman line-shape of SiNWs with their heavily doped crystalline counterparts. Raman spectrum of sample N[#] (Figure 6.6, top panel) is more red shifted and more asymmetric as compared to Raman spectrum of c-Si-N (Figure 6.3a). This can be understood from PCM because phonon confinement produces asymmetric broadening with $\alpha_R > 1$. Therefore in N[#] nano-effect as well as Fano resonance both increases the lower half widths of the Raman line-shape. This way the Fano resonance contribution adds up to the already existing asymmetry due to nano-effect. This is quantitatively evident from the α_R value which increases from 1.2, when only Fano resonance is present, to 2.78 when Fano resonance is present along with nano effect. In contrast to this, Raman spectrum of sample P[#] is less asymmetric with $\alpha_R = 0.78$ as compared to Raman spectrum of its bulk counterpart with $\alpha_R = 0.58$. This seems to be in contradiction to the above trend hence needs careful explanation and theoretical framework, developed in the above section (Figure 6.5), may prove to be useful in this attempt. It has already been analyzed in theoretical section above that in p-type system, Fano resonance and nano effect induces additional half widths in opposite energy sides of the Raman peak. The Fano resonance in sample P[#] induces extra half width on the post-maximum side of the peak position by keeping the pre-maximum half width unchanged. This way the Fano resonance induced half width increase compensates the nano-effect induced half width to help the α_R of the line-shape approach unit value. Therefore the value of α_R caused by Fano resonance in c-Si-P is 0.58 but when SiNWs have been fabricated from c-Si-P, nano effect comes in P[#] which produces broadening in lower energy side hence value of γ_L/γ_H increases to 0.78 i.e., it comes closer to unity. The observed anomaly in the Raman line-shape can be explained based on compensatory and additive nature of nano-effect

and Fano-resonance with each other for p-and n-type SiNWs. It is also worth mentioning here that the sufficiently low excitation laser powers were chosen to avoid any heating related effects which will further complicate the analysis.

Furthermore, to quantitatively validate these observations, the experimental Raman scattering data obtained from SiNWs samples of $N^{\#}$ and $P^{\#}$ have been fitted by a theoretical Raman line shape given in Eq.6.3 which takes care of the nano-effect as well as Fano resonance with nanocrystallite size. The value of 'q' can be obtained by the best fitting of the observed Raman line shape from the samples. The negative value of q is used to fit for $N^{\#}$ (n-type samples) while positive value of q is used to fit for $P^{\#}$ (p-type system) [61].

The fitting parameters are summarized in Table-6.2 and the line-shape corresponding to these values are represented by solid lines in Figure 6.6. It is notable here that bit difference between peak position of experimental and theoretical Raman line shapes is observed. It could be possible due to stress present in the system as the SiNWs have been prepared from heavily doped Si wafers, which contain stress. It is worth mentioning here that presence or absence of stress in the system does not affect the Fano resonance. Obtained fitting parameters confirm the presence of Fano resonance and nano-effect together.

Table 6.2: Raman parameters estimated from Raman spectra of SiNWs samples of $N^{\#}$ and $P^{\#}$ by theoretical fitting of experimental data (discrete points in Figure 6.6) with Eq.6.3.

Sample	Raman Peak position	FWHM	Asymmetry ratio	Fano asymmetry parameter 'q'	SiNWs size
$N^{\#}$	518.5 cm^{-1}	10 cm^{-1}	2.38	-9	6 nm
$P^{\#}$	517.5 cm^{-1}	14 cm^{-1}	0.78	+4	3 nm

It is clear from Table 6.2 that the average size of SiNWs formed in

sample P[#] is ~3 nm while the average size of SiNWs formed in sample P[#] is ~6 nm. Presence of thinner SiNWs in sample P[#] as compared to sample N[#] is consistent with TEM images shown in Figure 4.16 (TEM images of sample N[#] and P[#]). Additionally, the absolute value of Fano parameter q is smaller $|q| = 4$ in case of sample P[#] than $|q| = 9$ in case of sample N[#] because the doping level is higher in sample c-Si-P than c-Si-N. On the whole, the combination of Fano resonance and nano effects may be compensatory or incremental to each other, to be reflected in Raman line-shape, for a p-type and n-type system respectively in the absence of heating related perturbations. After complete analysis of electron optic phonon interaction both experimentally as well theoretically, the electron acoustic phonon interaction also have been studied using the low frequency Raman scattering of Si NSs and discussed in following section.

6.2 Electron-Acoustic Phonon Interaction: Fano Scattering

The Fano resonance (interference of electron-optic phonon) have been extensively studied in both n-type and p-type heavily doped Si wafers and the Si NSs fabricated using these wafer in the previous sections both theoretically and experimentally. An attempt has been made to extend the study of Fano resonance when a quantum interference taking place between a low energy discrete state i.e. low frequency phonons with an appropriate continuum of energy states. It means that two conditions are required to exhibit Fano effect i.e. presence of discrete state and suitable energy continuum. It is well known from the dispersion curve of Si that at the zone center low frequency phonons (acoustic phonons) are absent in case of Si (see Figure 2.2 in chapter 2) but as the size of Si approaches towards its Bohr exciton radius (~5nm) the acoustic phonons, with finite frequency, corresponding to finite wave vector (k) may be available for scattering.[96]

To study the interference of electron and low frequency phonons, first it is important to check the possibility of interaction between the two i.e. whether they meet the necessary requirements for interaction or not. It is well established fact that Fano interaction between optic phonons and electronic continuum (e.g, in Si and its NSs) can be seen if width of the continuum is more than the phonon energy [216]. In Si NSs, due to absence of a clear band structure, a quasi-continuum of electronic states [217] are available to interact with optic phonons mediated by interferons [217]. Acoustic phonons, having energies lower than the optic phonons, by default full fill the above-mentioned criteria. Thus Fano effect resulting due to acoustic phonon-electron interaction is technically possible but such reports are very limited and needs further careful investigation about its observation and nature.

In order to understand the above mentioned discussion regarding the interference between electron and phonon first the schematic diagram has been drawn just to check the possibilities of interaction. Figure 6.7 represents the possibility of interaction between Interband (marked with * in Figure 6.7a) and intraband (marked with # in Figure 6.7a) energy continuum with both optic and acoustic phonons. From the above discussion it is clear that the width of the interband continuum matches with the energy of optic phonons hence the interference is possible in this combination and results in the Fano interference (Figure 6.7b).

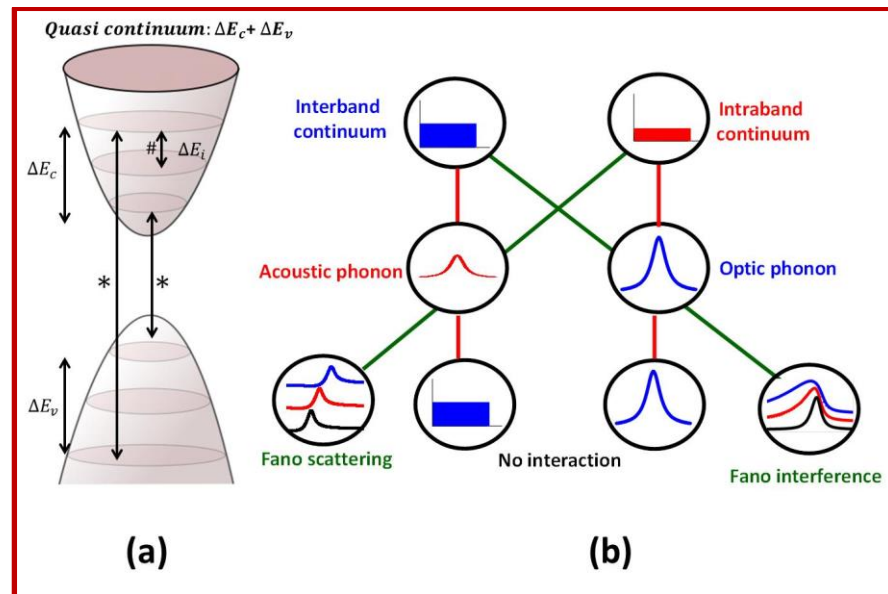


Figure 6.7: (a) Schematic representation of inter- and intra-band transitions. (b) Graphics to explain various combinations of electronic-discrete energies where Fano interaction is possible.

On the other hand, the energy of acoustic phonons is very less as compare to the energy of interband continuum, due to this it does not meet the necessary prerequisite and does not show the interaction resulting in no Fano resonance (Figure 6.7b). It is evident from Figure 6.7 that the energy of intraband continuum (# mark in Figure 6.7a) is very less as compared to the energy of the optic phonons means it automatically qualify the possibility of interaction, but the interaction is very weak due to which it will not be visible in the respective spectrum. Similar to the all interaction discussed above the energy of intraband continuum is of the order of few meV and the energy of acoustic phonon is also in the same range in case of Si (2-3 meV), means they may interact with each other the way optic phonon interact with inter band continuum.

Observation of low frequency Fano resonance has been predicted in low dimensional Si to be visible through Raman scattering to yield an asymmetric Raman line-shape for which a line-shape function has been modelled. Further the same has been validated experimentally from Si NSs samples prepared by different technique, the laser induced etching

or LIE. Sample details are given in Table 3.3 in chapter 3. It is proposed that due to relaxation of selection rule ($k=0$) low frequency phonons are available for Raman scattering in the Si NSs. It is worth mentioning here that observation of Raman scattering from nanomaterials at low frequency has been reported [218,219] but little information is available about the asymmetry of the observed Raman line-shapes. The current analysis will also help in understanding it using the developed framework of Fano interaction/scattering.

Observation of low frequency phonons using Raman scattering in Si NSs and its asymmetric nature hints at a possible connection between the Fano resonance, Raman scattering and quantum confinement effects. It means that a phenomenon, similar to Brillouin scattering, is possible at nanoscale in low frequency regime thus may be called “Fano scattering” in general. Three samples (namely N25, N45 & N60 given in table 3.3 in chapter 3) of Si NSs, with varying sizes between 3 to 5 nm, were fabricated using LIE technique. To study Fano scattering, Raman spectra of these samples have been recorded. Raman spectra from samples N25, N45 and N60, displayed in Figure 6.8(a), shows asymmetric Raman spectra with peaks centered at 22.5 cm^{-1} , 27.5 cm^{-1} and 33.5 cm^{-1} respectively.

The discrete data points in Figure 6.8(a) shows the experimentally observed Raman scattering data and solid line shows the theoretically calculated Raman line shapes which will be discussed later. Figure 6.8(b) shows the Raman parameter calculated from Raman spectra shown in Figure 6.8(a). It is evident from Figure 6.8(b) that as the size decreases the α_R increases and the same trend is observed for FWHM. The observed Raman spectra correspond to the acoustic phonons in Si NSs due to relaxation in Raman selection rule as a result of quantum confinement effect [90]. Acoustic phonons cannot be observed from its crystalline counterpart because no acoustic phonons are present at zone center of phonon dispersion curve (γ -point, shown in Figure 2.2) [105] which are the only ones that can participate in Raman scattering due to $k=0$ selection rule.

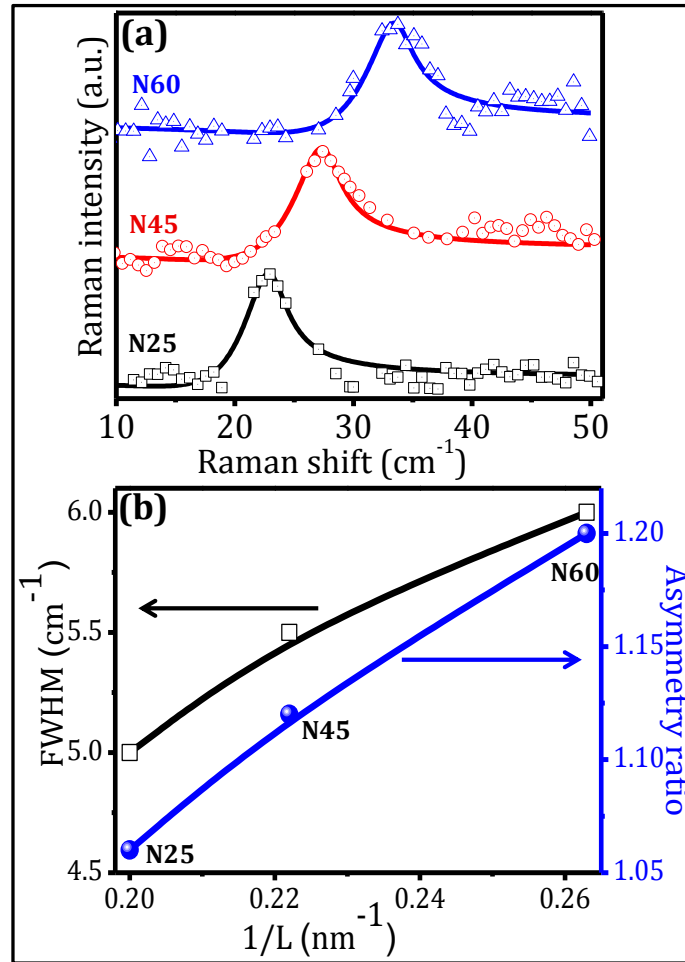


Figure 6.8: (a) Raman spectra from sample N25, N45 and N60 containing Si NSs. (b) Size-dependent variation in FWHM and α_R obtained from Raman scattering data shown in (a).

Quantum confinement effect, when considered alone, can explain observation of low frequency Raman spectrum but the asymmetry as observed by many researchers [218,219], is not obvious thus requires additional investigation and preferably a theoretical modelling. In quantum materials, like Si NSs, the electronic energy levels gets quantized and different inter- and intra-band transitions (these are non-radiative transitions) are possible and can be observed using Raman spectroscopy. Width of such an electronic continuum [213] (~650 meV) resulting from inter-band transitions are much higher than the intra-band continuum. Acoustic phonons, having energies of only a few meV can interact with the intra band electronic transitions taking place within the modified conduction band giving rise to quasi-continuum

and provide a platform for Fano interaction.

In order to study the Fano interference by low frequency phonons a theoretical framework have been developed by appropriately modify the Fano-Raman line shape (by incorporating the two effects quantum confinement and electron-phonon interaction given in Eq. 6.3) to result in the following Eq. 6.4.

$$I_{AF}(\omega) = \int_0^{k_f} \left[\frac{(\epsilon' + q)^2}{(1 + \epsilon'^2)} \right] C(k) d^2 k, \quad (6.4)$$

where

$$\epsilon' = \frac{\omega - \omega_A(k)}{\frac{\gamma}{2}}, \quad C(k) = k^8 e^{-\frac{k^2 L^2}{4a^2}},$$

$$\omega_A(k) = 761.9 \sin\left(\frac{\pi k}{2}\right) e^{-\frac{5\sqrt{k}}{0.6}}$$

Term in square bracket in Eq. 6.4 takes care of the effect of Fano interaction & quantum confinement effect on Raman line-shape. $C(k)$ is a weighing function which provides the information about the weighted contribution of a phonon corresponding to a given wave vector 'k'. The abovementioned weighing function has been used here so that the experimental Raman data fits well with Eq. 6.4. $\omega_A(k)$ represents the phonon dispersion relation corresponding to acoustic phonons for c-Si and 'a' is lattice constant of Si and $k_f = (a/L)^\vartheta$ is proposed as Fano's scattering coefficient which is a function of crystallite size 'L' and a coupling factor 'ϑ' which are fitting parameters along with 'q' the well-known Fano asymmetry parameter (where, 1/q is referred as Fano coupling strength).

The parameters obtained by fitting the Raman data from samples N25, N45 and N60 using Eq.6.4, has been listed in Table 6.3. To validate the sizes obtained by fitting the experimentally acquired low frequency Raman scattering data of sample N25, N45 and N60, the optical Raman spectra of these samples also have been recorded and fitted using Eq. 6.3 to calculate the size of NSs. Figure 6.9 shows the optical Raman spectra of sample N25, N45 and N60 with discrete data points representing the experimentally obtained Raman spectra and solid line

shows the theoretically calculated Raman line shape using Eq. 6.3.

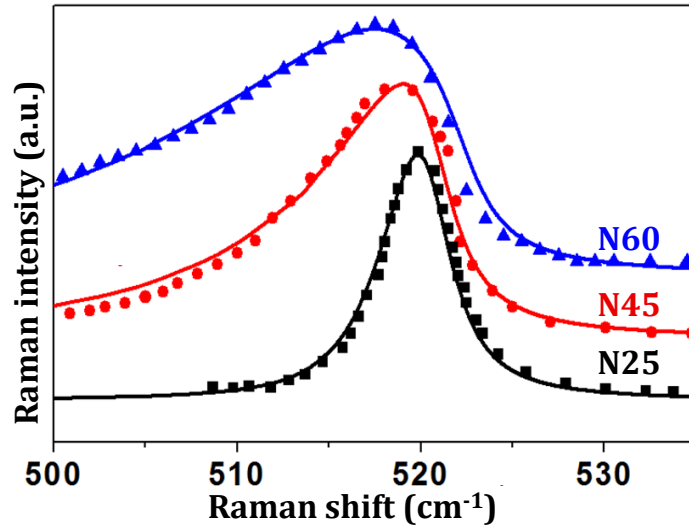


Figure 6.9: Raman spectra from samples N25, N45 and N60. Discrete points correspond to the experimental data whereas the solid lines corresponding to the theoretical line-shape calculated using Eq.6.4.

Table 6.3: Various fitting parameters obtained using Eq.6.4 with experimentally observed Raman spectra. Values in bracket in column 2 represent the nanocrystallite size estimated from optical Raman spectra shown in Figure 6.9.

Sample	Si NSs Size(L) (nm)	ϑ	q	k_f	Raman Peak position(ω) (cm ⁻¹)	$\omega(k_f)$ (cm ⁻¹)
N25	5.1 (5.3)	1.38	4	0.046	22.5	22.2
N45	4.5 (4.5)	1.33	3.5	0.060	27.5	27.8
N60	3.8 (4.0)	1.30	3	0.078	33.5	34.0

The size of NSs calculated using optical Raman spectra are written in bracket in column 2 in Table 6.3. The estimated sizes from acoustic and optic phonons are in well agreement with each other. It is evident from Table 6.3 that in order to achieve best fitting in case of low frequency Raman spectra (Figure 6.8(a)) of sample N25, N45 and N60 the used Fano parameters' values are 4, 3.5 and 3 respectively, where q

is the measure of Fano interaction. From the above discussion it is clear that the Fano interaction is present (presence of finite value of q) in the low frequency phonon when it interacts with the intraband energy continuum. The electron-acoustic phonon interaction (Fano Scattering) has been explained pictorially by giving a “snake–food” analogy through graphics and provided as Figure 2A.1 in Appendix 2.

6.3 Study of Non-Radiative Transition in Si Nanostructures by Fano Scattering

As discussed above, the Fano Scattering contains the intraband electronic continuum and acoustic phonons. If any how the phonon contribution is extract from the Fano scattering then, only the electronic part i.e. intraband continuum remain in the spectrum and the intraband continuum is nothing but the non-radiative transition present in the Si NSs. The schematic diagram has been sketched (Figure 6.10) to understand such procedure.

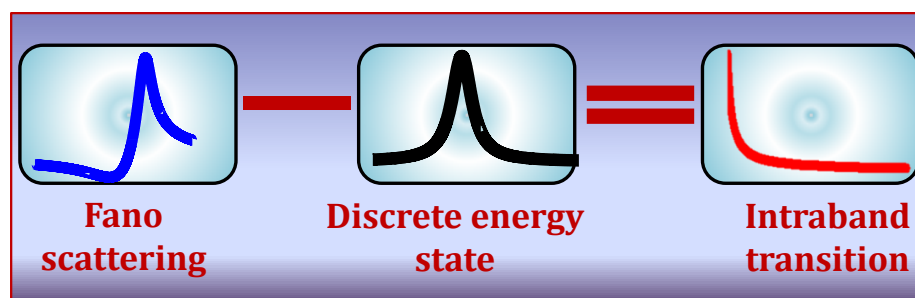


Figure 6.10: Schematic representation of non-radiative intraband transitions can be extracted using Fano scattering.

The detailed recipe to obtain this continuum is as follows. For a given sample, information about Raman peak position and half width (towards lower energy side of the peak) of the line-shape are already available. A Lorentzian line-shape generated using these Raman line-shape parameters will be a true representative of the discrete component alone. This Lorentzian component can then be subtracted from the corresponding Fano scattering line-shape to obtain the continuum. It is evident from Figure 6.10 that the discrete energy state

when eliminated from the Fano Scattering Raman line-shape results in the electronic continuum i.e. non-radiative intra-band transitions [60].

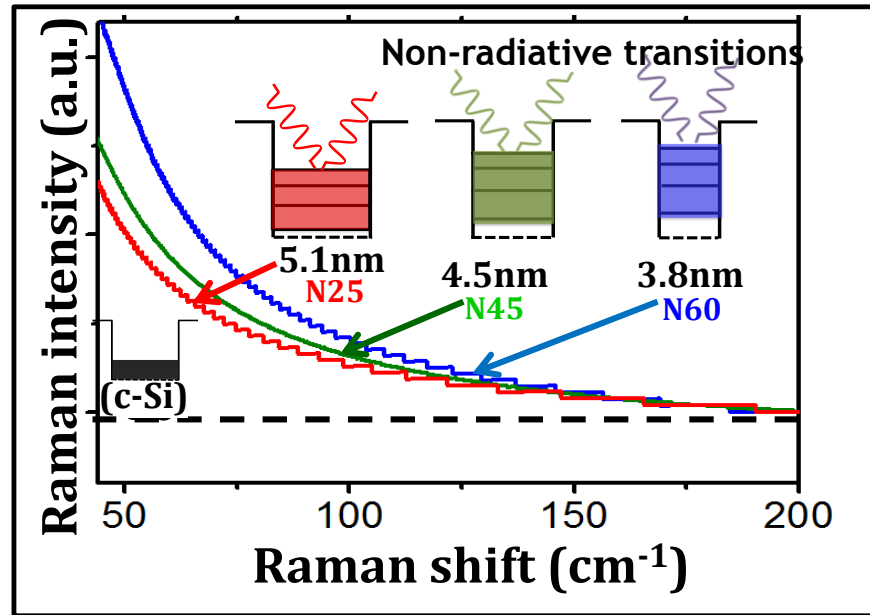


Figure 6.11: Nonradiative continuum obtained from Fano scattering data corresponding to Si NSs of different size. Dotted line shows constant continuum for c-Si for comparison.

Figure 6.11 shows the estimated continuum obtained using the above-mentioned method, for samples N25, N45 and N60 having Si NSs of different sizes. It is evident from Figure 6.11 that the continuum varies with Si NSs size with spectra becoming steeper with decreasing size. This can be explained using quantum confinement effect due to which the energy levels get more and more discretized with increasing separation between energy levels for smaller sizes. The unequal separation between these quantized energy levels induces unequal transition probabilities which is reflected as the obtained intensity profile as shown in Figure 6.11. This is explained using the band picture in the inset of Figure 6.11. For c-Si the continuum is rather constant as expected due to absence of separation of energy levels at all which is also shown in inset of Figure 6.11 for comparison. It is important here to mention that these continua are present due to intra-band transitions which are non-radiative transitions. Thus the proposed method gives a method to observe non radiative transitions

experimentally which is not possible to see otherwise.

6.4 Summary

In summary, a two-fold approach (theoretical as well as experimental) has been adopted to understand the effect of perturbations induced by electron-optic phonon (Fano resonance) and electron-acoustic phonon (Fano Scattering) interaction on Raman scattering from crystalline and nanocrystalline Si. The doping and size dependent Fano effect have been understood using Raman scattering from heavily doped bulk Si and SiNWs fabricated from n- and p-type Si wafers. Fano resonance in n-type confined system enhances the asymmetric broadening of Raman line shape as reflected by increased asymmetry ratio with respect to its bulk counterpart (highly doped n-type c-Si). In contrary, Fano resonance in p-type confined system compensates the asymmetry of the Raman line shape, already induced by confinement, and results in decreased asymmetry with respect to the p-type c-Si wafer. However line-shape asymmetric broadening increases irrespective of the doping type as long as the system is in the quantum regime. It means that the asymmetry in the Raman line-shape gets amplified in n-type and gets cancelled in heavily doped p-type low dimension Si system when Fano resonance and quantum confinement effect are present together. Low frequency Raman scattering from Si NSs (Fano scattering) gives a method to estimate intraband continuum. This provides an experimental way to measure non-radiative transitions which is not observable otherwise.

Chapter 7

Optical Properties of Silicon

Nanostructures

Change in the optical properties due to quantum confinement of electrons in Si NSs is studied in the present chapter. Diffuse reflectance absorption spectroscopy has been employed to quantify the band gap energies in different Si NSs samples fabricated by MIE. PL and its origin in Si NSs samples are discussed. Section 7.1 deals with Kubelka-Munk theory of band gap calculation from diffuse reflectance. The band gap estimation of different Si NSs samples fabricated by MIE is given in section 7.1.1 and 7.1.2 while the results of PL measurement from Si NSs are discussed in section 7.2. Origin of room temperature PL is discussed on the biases of lifetime measurement in section 7.3. The major conclusion of this chapter is summarized in section 7.4. Some of the results presented in this chapter are published in the literature⁵.

⁵ Priyanka et al., *Superlattices Microstruct*, 120,141-147, (2018),
Priyanka et al., *Communicated*

7.1 Band Gap Estimation from Diffuse Reflectance using Kubelka-Munk Function

Kubelka-Munk model allows the band gap estimation of unsupported materials like powder or rough films. Due to scattering the band gap estimation of powder and rough film is not possible by typical UV spectroscopic techniques. Basically Kubelka-Munk function is directly proportional to the absorption coefficient of the material [156]. Diffuse reflectance spectra (DRS) of the samples are converted to equivalent absorption using Kubelka-Munk function $F(R_\infty)$ for infinitely thick samples which is given by [220]

$$F(R_\infty) = \frac{K}{S}, \quad (7.1)$$

$$K = (1 - R_\infty)^2, \quad (7.2)$$

$$S = 2R_\infty, \quad (7.3)$$

where, $R_\infty = R_{\text{sample}}/R_{\text{standard}}$. R_{sample} is the diffuse reflectance of the sample and R_{standard} is diffuse reflectance of the standard sample (BaSO₄ in the current study). K and S are the Kubelka–Munk absorption and scattering functions, respectively. After getting Kubelka-Munk absorption, the band gap estimation can be done by well know method, Tauc plot [158] , in the following manner:

The following relational expression proposed by Tauc [221], Davis, and Mott is used.

$$(h\nu\alpha)^{1/n} = A(h\nu - E_g), \quad (7.4)$$

where, h is Planck's constant, ν is frequency of incident photon, α is absorption coefficient, E_g is band gap and A is proportionality constant. The value of the exponent n denotes the nature of the sample transition.

For direct allowed transition..... $n = 1/2$

For direct forbidden transition..... $n = 3/2$

For indirect allowed transition..... $n = 2$

For indirect forbidden transition..... $n = 3$

Since $F(R_\infty)$ is proportional to the absorption coefficient. Therefore α in the Tauc Eq. 7.4 is substituted with $F(R_\infty)$. Thus, the modified expression becomes:

$$\{h\nu \times F(R_\infty)\}^{1/n} = A(h\nu - E_g), \quad (7.5)$$

Now using the Kubelka-Munk function, the $[h\nu \times F(R_\infty)]^{1/n}$ plotted against the $h\nu$. The curve that plots the value of $h\nu$ on the horizontal axis and $[h\nu \times F(R_\infty)]^{1/n}$ on vertical axis is drawn. Further a line is drawn tangent to the point of inflection on the curve and the $h\nu$ value at the point of intersection of the tangent line and the horizontal axis provides value of band gap (E_g).

7.1.1 Band Gap Estimation of Si NSs Samples

It is well known that the band gap of a material will increase if the dimension of a material is reduced to sizes comparable to the Bohr exciton radius. In order to establish the quantum confinement effect present in the samples fabricated by MIE, diffuse reflectance absorption (DRA) spectroscopy [222,223] have been employed on the samples mentioned in Table 3.1. The reflection of size dependent change in band gap (E_g) is one of the strongest signatures which can establish the existence of quantum confinement effects in low dimensional semiconductor systems in general and in Si in particular [224]. Band gap measurements have been carried out from Si NSs fabricated using both n and p-type Si wafer using DRA as displayed in Table 3.1.

In order to calculate the band gap of sample P* and P#, the DRA spectra have been recorded for these samples using the spectrometer of Agilent Cary 60 UV-Vis. Figure 7.1 shows the DRA spectra of sample P* and P#. Discrete data points show the experimentally obtained DRA spectra while the solid line correspond to theoretical fitting. The

qualitative analysis of Figure 7.1 have been done using Kubelka-Munk (KM) method which is a well-established mode employed for this purpose for solid samples [223] such as SiNWs prepared using Si wafer.

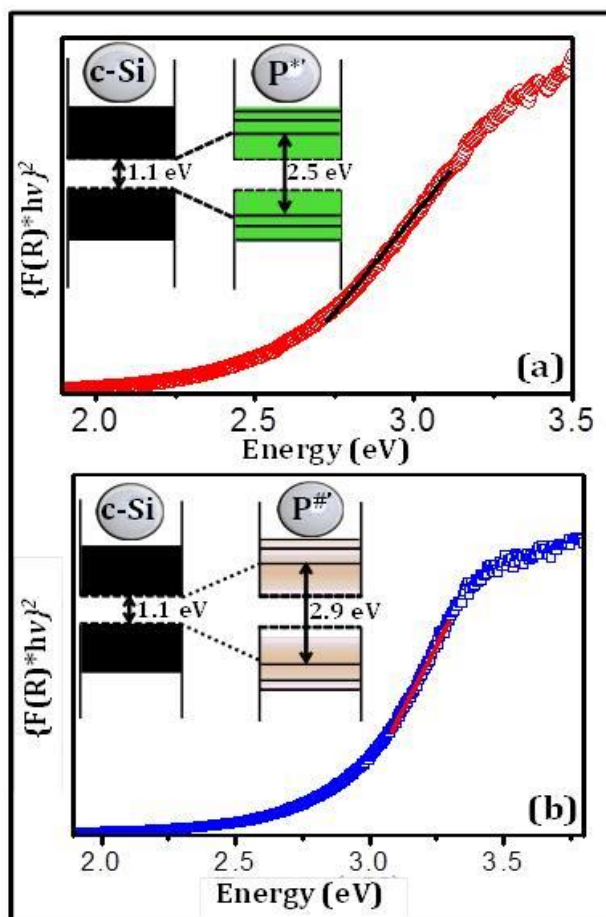


Figure 7.1: DRA spectra of sample P* and P#, discrete data points show the experimentally obtained DRA spectra whereas solid line corresponds to theoretical fitting. Inset (a) & (b) shows the schematic representation of energy band gap of P* (along with c-Si) and P# (along with c-Si) samples respectively.

The calculated values of E_g using KM function are 2.5 eV and 2.9 eV for sample P* and P#, respectively which are much higher than the c-Si band gap of ~ 1.1 eV. Inset of Figure 7.1 shows the schematic representation of energy band gap in c-Si, P* (inset of Figure 7.1a) and P# (inset of Figure 7.1b) sample. However the E_g for c-Si is 1.1 eV which is much lesser than the E_g of sample P* and P#, which fabricated by MIE technique. As from the above calculation of E_g of

sample P*’ and P[#]’ shows significant increase in E_g , which has been explained on the basis of quantum confinement effects that take place in semiconductors having sizes of the order of the equivalent Bohr radius [225].

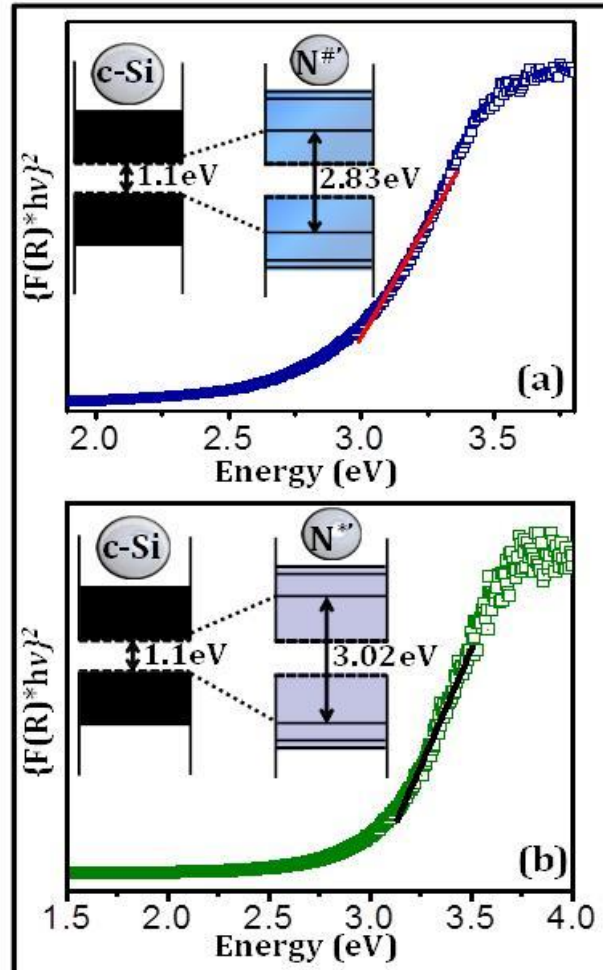


Figure 7.2: DRA spectra of sample N[#]’ and N*’’, discrete data points show the experimentally obtained DRA spectra whereas solid line corresponds to theoretical fitting. Inset (a) & (b) shows the schematic representation of energy band gap of N[#]’ and N*’’ (along with c-Si) samples respectively.

Hence this increase in E_g clearly shows the size of SiNWs in sample P*’ and P[#]’, is comparable to the Bohr exciton radius (i.e. 5 nm) of Si.

In order to further confirm the presence of quantum confinement the band gap measurement of sample prepared by n-type Si wafer (N*’ and N[#]’) also have been carried out. The discrete data points in Figure 7.2 shows the experimentally obtained DRA spectra of sample N*’ and N[#]’.

and solid line corresponds to theoretical fitting. The quantified values of E_g is 2.83 and 3.02 eV for sample N[#] and P[#] (using theoretical fitting). The E_g of sample prepared by n-type Si wafer also shows enrichment in E_g with respect to its bulk counterpart (c-Si 1.1 eV). It is clear from these E_g measurements the Si NSs fabricated using both n- and p-type Si wafers indicates presence of quantum confinement effect.

7.1.2 Doping Dependent Band Gap of n-& p-type SiNWs

As from Figure 4.16 (TEM images of sample N[#], P[#]) in chapter 4 that the sizes of Si NSs present in sample P[#] is smaller with respect to the sample N[#]. It is clear from Table 3.2 that the sample P[#] having comparatively high doping as compare to sample N[#] which shows some connection of size and doping effect i.e. the size of Si NSs may depends on the doping level present in the Si wafer. As it is well known that if the size of Si NSs is less and comparable or equal to its Bohr exciton radius (5 nm) then the system shows strongly or weakly confined system respectively. As the size becomes smaller than its Bohr exciton radius then the system shows strong confinement effect. To differentiate between weak confined, and strong confined system the band gap measurement is one of the best techniques in all available.

It is evident from Figure 4.16, the TEM image which suggests that the size of Si NSs in sample P[#] and N[#] is ~3 nm and ~6 nm respectively [226]. As from the above discussion if the size of NSs is less compared to Bohr radius it is a strongly confined system and its E_g will be more with respect to the weakly confined system. In order to confirm the increase in E_g the DRA spectra of sample N[#] and P[#] have been recorded and analysed theoretically to calculate E_g . Figure 7.3 shows the DRA spectra (discrete data points show theoretically obtained DRA spectra and solid line shows the theoretical fitting) of samples P[#] and N[#]. The calculated values of E_g are 2.90 eV and 2.83 eV for sample P[#] and N[#] respectively.

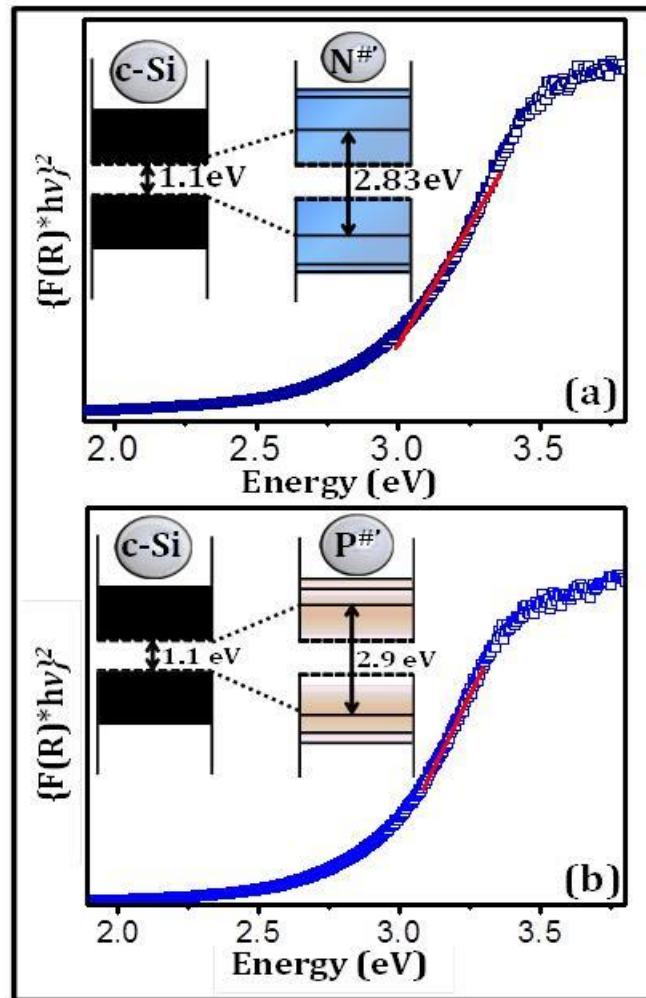


Figure 7.3: DRA spectra of sample $N^{\#}$ (low doped) and $P^{\#}$ (highly doped) Si NSs. Discrete data points show the experimentally obtained DRA spectra and the solid line corresponds to theoretical fitting. Inset (a) & (b) shows the schematic representation of energy band gap of $N^{\#}$ and $P^{\#}$ (along with c-Si) samples respectively.

It is clear from the quantification of band gap in both the samples that the strongly confined system having more E_g with respect to the weaker one. The consistency of TEM and DRA results established the doping level decides the size of NSs. As from the previous literature, if the size of Si becomes of the order of its Bohr exciton radius then it behave as a direct band gap material and can show the emission of light (PL). To check the possible emission of light from Si NSs samples (mentioned in Table 3.1) fabricated using MIE, PL spectra have been measured by exciting the samples with 405 nm wavelength

using diode laser.

7.2 Photoluminescence of Si Nanostructures.

In order to confirm that whether the Si NSs fabricated using MIE shows emission of light (PL) or not, the PL measurements have been carried out. Figure 7.4 shows the RT PL spectra of sample N^{*}, N[#], and P^{*}. The Si NWs exhibit an orange colour emission of light which is revealed by the photograph (after blocking the 405 nm illuminating light) of sample under 405 nm illumination shown in the inset of Figure 7.4. A broad band emission in the range of 625 nm to 750 nm (1.65 eV to 2 eV) is observed in all the three samples. The PL spectra of the samples could be fit well with two Gaussian peaks for samples N^{*} and P^{*}, whereas an additional third Gaussian peak is required to get the best fit for sample N[#] (Figure 7.4).

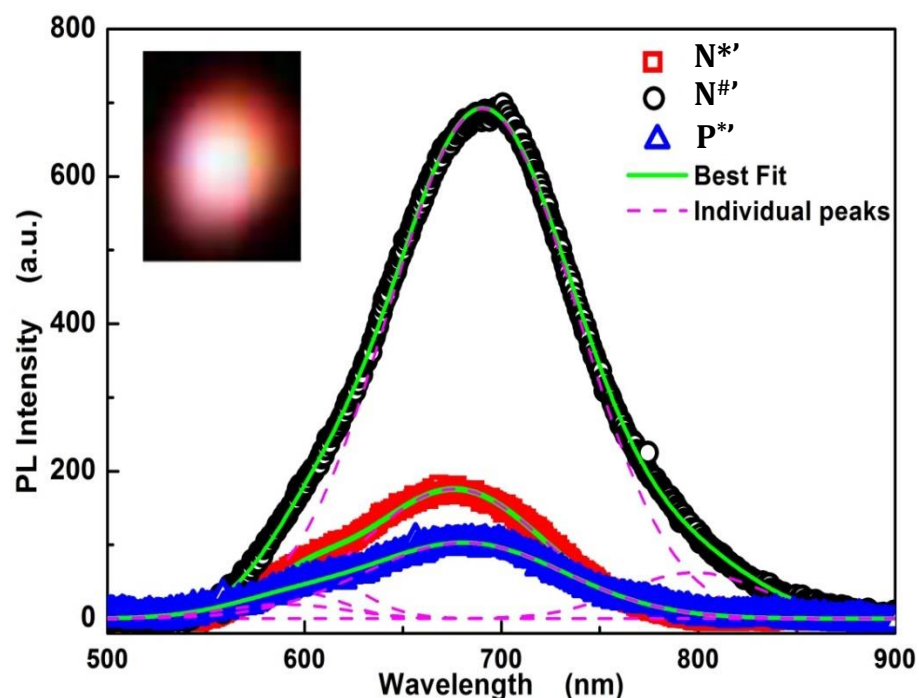


Figure 7.4: PL spectra of sample N^{*}, N[#], and P^{*}, at RT. Green line over the corresponding experimental points is the best fit to the data with sum of multiple Gaussian peaks. The isolated individual peaks are shown in pink color for all the samples. The inset shows a representative actual photograph of PL emission from the sample N[#], when excited using 405 nm source.

The strongest peaks that contribute to the PL have its peak at wavelengths 676 nm, 690 nm and 681 nm for N*['], N[#]' and P*['] respectively. In addition to this strong peak, all the samples have a weaker peak towards the blue side centered at 598 nm, 601 nm and 590 nm for N*['], N[#]' and P*['] respectively. It is evident that all the samples show a nearly similar behaviour except for the sample N[#]' which has an additional weak peak on the red-side of the PL centered at 798 nm.

7.3 Time Resolved PL Study of Si NSs.

In order to understand the emission of PL spectra more closely, time-resolved PL studies have been carried out using TCSPC system at RT on sample N*['], N[#]' and P*[']. The PL decay measurements have been done by collecting the full emission spectrum to understand the mechanism of PL in Si NSs of sample N*['], N[#]' and P*[']. Figure 7.5 shows the time dependence of the PL intensity for sample N*['], N[#]' and P*['] zoomed in three different time domains, sub-ns, few ns and in few tens of ns. The instrument response function (IRF) is also shown along with the experimental PL intensities (cyan curve). Just after the arrival of exciting femtosecond pulse (~100 fs) the PL intensity from the sample increases. Since the excitation pulse is much shorter, initial rise nearly follows the IRF. From the time dependence shown in different time scales one can clearly see the existence of three different decay times thus, the experimental data was fitted with a PL function given by following Eq. 7.6:

$$I_{PL} = A_1 e^{-t/\tau_1} + A_2 e^{-t/\tau_2} + A_3 e^{-t/\tau_3}, \quad (7.6)$$

where A_i 's are the amplitudes for the corresponding decay times τ_i . This PL intensity dependence is then convoluted numerically with the experimental IRF and then was fitted to the experimental time dependent PL data. The red solid lines shown in Figure 7.5 correspond to the best fit to the experimental data with Eq. 7.6. Although the

fastest decay in the PL of the samples is very close to the IRF still a short PL lifetime is required for proper fitting of the data. This fast decay time was estimated to be 18, 18 and 15 ps respectively for sample N^{*} , $N^{\#}$ and P^{*} .

The decay times obtained from the best fit for the PL data are much longer than few picoseconds as given in Table 7.1. It is evident that each sample has a decay time one in the order of sub nanosecond and another in the order of a few nanoseconds to tens of nanoseconds. Long PL life times of the order of a few μ s have been reported in literature [83]. To verify the same samples have been excited using second harmonic (400 nm) of 35 fs, 800 nm pulses of repetition rate 1 kHz and detected the PL using a fast photodiode-oscilloscope combination. The signal measured using the ultrafast laser is not more than few tens of nanoseconds which means that long lived PL emission from all the three samples are negligible.

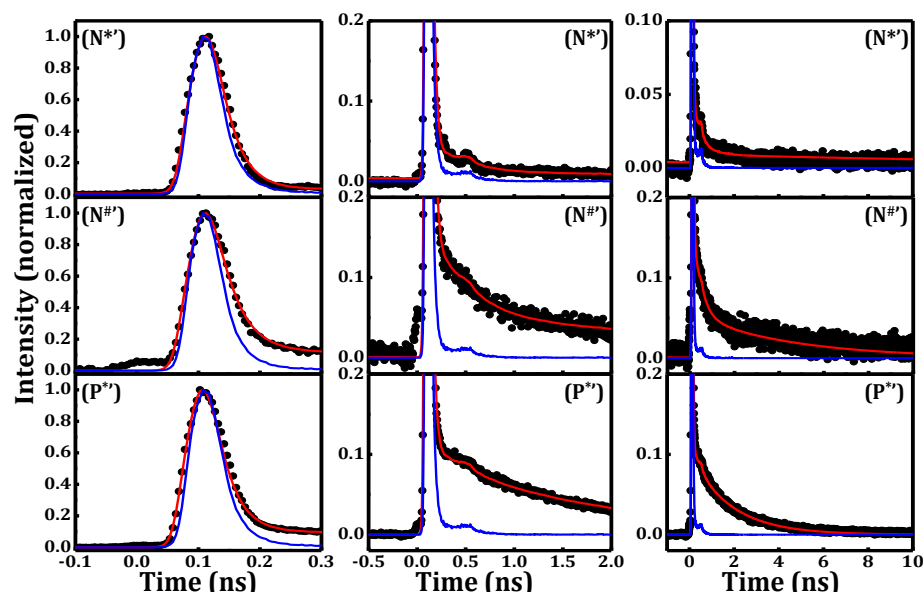


Figure 7.5: The time dependence of the PL intensity of sample N^{*} , $N^{\#}$ and P^{*} measured using TCSPC. The data is plotted in different time range to show existence of multi exponential decay in the PL intensity. Dots represent the experimental data, the cyan line is the IRF and the red lines are the best fit obtained by fitting the data with Eq. 7.6 convoluted with IRF.

Table 7.1: Decay time obtained from the best fit of time dependent PL (Figure 7.5).

Sample name	Size (nm)	τ_2 (ns)	τ_3 (ns)
N [*] ,	3	0.55	12
N [#] ,	6	0.39	4.5
P [*] ,	7	0.36	1.8

Figure 7.6 shows the size dependence of the longer decay times τ_2 and τ_3 . Irrespective of the type of Si (n- or p-type or doping level), clearly a monotonic trend is followed and the decay times decrease with increase in the size of the NSs. It is evident from the PL spectra and PL decay times of all the samples (Figures 7.4 & 7.6) that the type of dopant as well as the doping level is not playing any direct role on PL emission spectra as well as on PL decay in all the three samples (from Table 3.2 that sample N[#], having comparatively higher doping with respect to the sample N^{*}, and P^{*}). In fact, they depend on the size of the Si NSs instead.

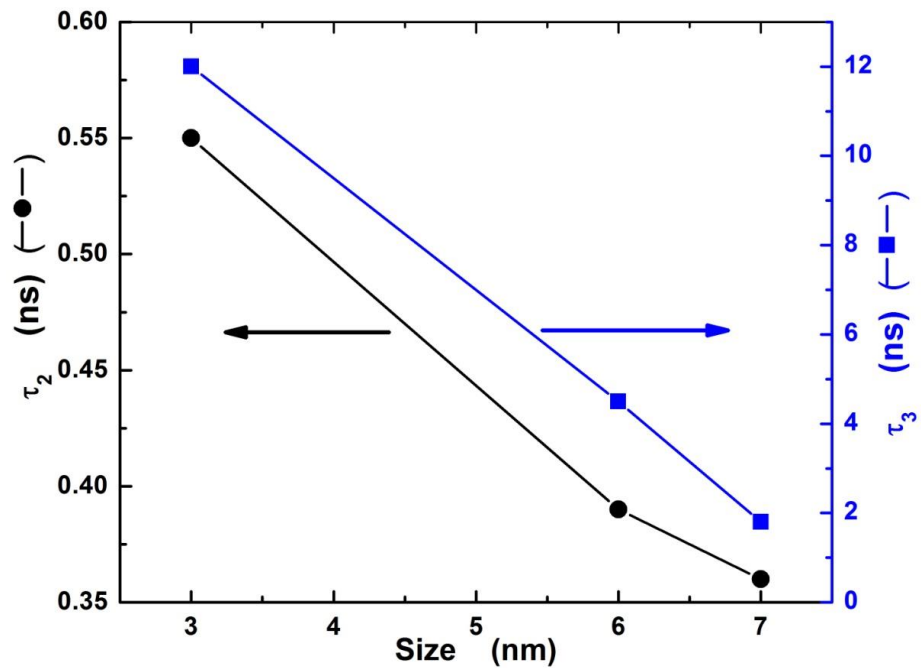


Figure 7.6: The dependence of PL life times (τ_2 and τ_3) on the size of the Si nanostructures present in the sample.

The size dependent change in properties is usually explained within the

framework of quantum confinement effect but the same explanation in the present case may be misleading. A direct attribution of the PL (Figure 7.4) to the quantum confinement is unlikely here since a size confinement should induce a strong blue shift for the sample N*’ [6]. This is because N*’ has Si NSs of size ~3 nm which is very small when compared to the other two samples N[#]’ and P*’, which have NSs of much larger size (6 and 7 nm). It is evident from the results of PL spectra (Figure 7.4) that the PL peak position does not show any direct size dependence.

Although the PL emission strength should depend on the density of Si NSs per unit volume present in the sample, in case of Si NSs since it changes from indirect bandgap to direct therefore an increase in PL emission also expect with reduction in size of the particles. Clearly the PL emission strength does not show any such size dependence (Figure 7.4). It is worth mentioning here that although the substrate used for the preparation of all the samples are different still they show the strongest peak nearly at 680 nm and a next stronger peak at ~600 nm. Thus the PL peak from these samples does not depend on the type of doping and doping concentration. Based on these evidences the origin of PL to such a recombination process which are independent of size, type of doping and doping concentration have been attribute in the present study. The interface between Si and SiO_x, present inherently in the porous Si NWs prepared by MIE [227–229] might come to rescue in explaining the above-said origin of PL. In such cases, the surface roughness, and the porosity, present in the sample should show a direct correlation to the PL lifetime in the samples.

To further understand the dependence of PL lifetime on the NSs’ size the TEM images of sample N*’, N[#]’ and P*’ have been used which is shown in the appendix 3. It has been reported in the previous literatures that the NWs contains few nm sized Si NSs [184,280] on the wires which itself shows porous nature when fabricated by MIE. Figure 1 to Figure 3 (main image) in appendix 3 show the TEM images of NWs (these NWs are scratched out from their substrates into DI

water and dried on TEM grid) present in samples N*’, N#’, and P*’. It is clear from the TEM images (from Figure 1 to Figure 3 of appendix 3) that the material distribution inside and the surface of the nanowire is non-uniform and porous [230]. The non-uniformity in the surface can be clearly seen at the edges of the nanowires in TEM images.

A two-fold approach has been used to specify this roughness or porosity (from now on here call porosity in general) of Si NWs present in TEM images using image data processing. On a gray scale TEM image, the amount of material present at a location corresponds to the darkness of the image. Using this gray scale value the surface plots, acquired from the wires visible in the TEM images, have been shown in the corresponding insets of Figure 1 to Figure 3 (selected area marked by white dotted line, top right in sample N*’ and bottom right and left in sample N#’, and P*’, respectively).

It can be visualized from the surface plots in the insets of all the samples that the structure of the Si NWs has strong surface roughness and variation in the internal material distribution in the wire showing that the Si NWs fabricated are strongly porous in nature. It is also observed from the surface plot of sample N*’ that the porosity of Si NWs is less with respect to other two samples (from surface plot of N#’, and P*’, from Figure 2 & 3 in appendix 3). For clarity, line profile graphs of all three samples have also been plotted as inset in the Figure 1, 2 and 3 of appendix 3. The solid white line shows the selected portion on TEM image used to get the line profile of corresponding samples. The bottom right inset (Figure 1 in appendix 3) shows the line profile graph for sample N*’ and top left and right inset for sample of N#’, and P*’, (Figure 2 and Figure 3 in appendix 3) respectively. For a given length, the plot appears uneven, which is less in sample N*’ in comparison with the other two samples’ line profile graphs.

To quantify the length scales at which the variation in density of material distribution happens the spatial frequencies that exist in the TEM picture of nanowire have estimated using Fourier transform (FT).

The following procedure is adopted for the estimation of the spatial frequencies. First an area on the TEM image inside the nanowire, as large as possible, is selected (similar to the ones that are plotted as surfaces in Figure 1 to 3 in appendix 3). The image was then converted to a matrix of data using gray scale. To increase the number of data points for the FT the matrix of data is converted to a single array by randomly staking all the columns of data in to one column. By this random selection, details of nanostructures in a column are preserved and additional periodicity that can arise due to staking of data in sequence is reduced.

Further to compare between different samples the data for a single sample was normalized after subtracting its minimum value. This will scale the variation in each sample from minimum zero to a maximum of one. The numerical technique fast Fourier transform (FFT) was used for the estimation of distribution of spatial frequencies and the spatial dimensions were converted to appropriate spatial frequencies using the scale bar in the TEM picture. The amplitude of spatial frequencies (I_{SF}) that are present in the nanowire images of samples N^{*} , $N^{\#}$, and P^{*} , are shown in Figure 7.7. The few sharp periodic peaks in the I_{SF} are arising due to the column wise staking of data. One can clearly note that N^{*} has much lower spatial frequencies i.e. it is much smoother in real space than the other two samples ($N^{\#}$ and P^{*}). Note that smaller spatial frequencies correspond to density variation on larger length scale.

For example 10 nm structures are present in case of samples $N^{\#}$ and P^{*} , but are negligibly small in sample N^{*} . Here by negligible, mean that the I_{SF} that becomes comparable to that estimated for TEM image of same sample but outside the NWs. Similarly 5 nm structures are present in P^{*} and are negligible in the other two samples. Clearly increase in the porosity present in the order N^{*} , $N^{\#}$ and P^{*} can be directly correlated to the reduction in the PL decay time τ_2 and τ_3 in sample.

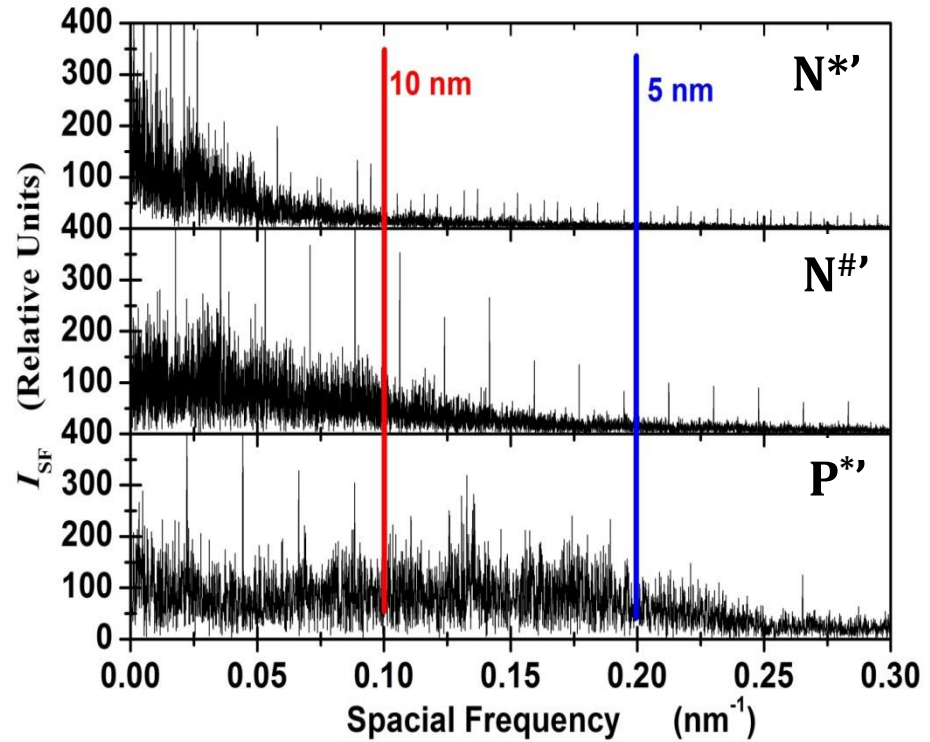


Figure 7.7: The dependence of amplitude of spatial variation in the material on the spatial frequencies for samples N^* , $N^\#$, and P^* estimated from TEM image of NWs. For the reader, the length periodicity in density distribution of material that will give rise to signal (I_{SF}) at two frequencies are also shown as vertical lines.

This means that the PL decays fastest for the most porous sample and decays slowest for least porous one amongst the three. The sample which has large porosity will have higher number of defects and interfaces. Further the higher variation in material distribution also means presence of larger amount of interfaces between Si and SiO_x . This implies that the interface between Si and SiO_x is playing a strong role in the decay process of PL in the samples [227–229].

In order to further understand the PL mechanism present in SiNWs fabricated by MIE technique, temperature dependent PL measurement of sample N^* , $N^\#$ and P^* have been carried out from room temperature (RT) to 100 K. Figure 4 in the appendix 3 shows the temperature dependent PL spectra of sample N^* , $N^\#$ and P^* . It is evident from the Figure 4 of appendix 3 that the PL spectra of all

sample is not showing much change in the peak position as the temperature is reduced from RT to 100 K though the size of Si NSs is very less in the sample N*’ with respect to the other two samples. The temperature dependent PL also validate that the emission of PL from the Si NSs is because of the interface between Si and SiO_x.

7.4 Summary

In summary DRA spectra reveal that Si NSs, fabricated by MIE are capable to show the quantum confinement effect as evident from size dependent band gap variation. The quantification of band gap of Si NSs has been done by Kubelka-Munk function using Tauc relation from DRA data. Effect of doping level on the band gap is studied which show that band gap of Si NSs is increasing with increasing doping level. The Si NSs fabricated using MIE shows a broad visible PL emission at room temperatures. The time dependence of PL intensity has been measured using TCSPC and three different decay times, one in the order of few tens of ps, other in the fraction of ns and another one in ns time scale were observed with almost no dependence on PL peak position. The PL spectra and the time dependence of the PL intensity did not show any direct dependence on the resistivity and dopant present in the Si wafers from which the Si NWs were fabricated. On the other hand the decay times of PL longer than few hundreds of ps increases with reduction in the size of the NSs. A direct correlation between the porosity, directly related with roughness, and PL decay time is observed implying that the PL life time gets affected by the nature of Si/SiO_x interface.

Chapter 8

Conclusions and Future Scope

New scientific findings along with all the conclusions deduced from the results reported in above chapters are listed here. This chapter also discusses future scope of work that can be carried out for further development in this field.

8.1 New scientific Findings in the present Thesis work

- (i) Discovered a subtle phenomenon called “Fano scattering” as a result of manifestation of electron-acoustic phonon interaction in Si NSs using Raman scattering in low frequency regime.
- (ii) Devised a method to quantify the extent of “short-range order” in *a*-Si using Raman scattering.
- (iii) Proposed a way to estimate the nonradiative transitions in the Si NSs.
- (iv) Explained Raman spectral anomaly in p-type SiNWs by successfully accounting for interplay between phonon confinement and Fano effect.
- (v) Fractal nature of porous Si has been revisited and explained the appearance of such nature.

Other important conclusions are summarised as follows:

8.2. Conclusions

The major conclusions of the research work reported in this thesis are the following:

- ❖ Well aligned SiNWs of n- and p-type Si wafer can be Fabricated using MIE technique via porosification.

- ❖ In MIE metal nanoparticles provides sites for porosification to start and more coverage of MNPs result in thinner SiNWs/wider pores.
- ❖ The texturization of Si wafer strongly depends on the junction formed between the metal, used in etching, and semiconductor.
- ❖ The Si nanostructures (SiNSs) have been textured on n- and p- type Si wafers using Ag (silver) and Au (gold) MNPs induced chemical etching. The combinations of Si NSs/Ag as well as p-Si/Au form Ohmic contact and result in the same texturization on the Si surface on porosification, where tent-shaped morphology has been observed consistently in both n- and p-type Si. Whereas, porosification result in different surface texturization for other two combinations (p-Si/Ag and NSs/Au) where Schottky contacts are formed.
- ❖ The SiNWs fabricated using MIE itself shows porous nature (the small Si NSs are present on the surface of SiNWs) i.e. the Si wafer become porous after etching and formed SiNWs and the wires formed after etching also shows porous nature, this is known as Fractal nature.
- ❖ The SEM and TEM studies have been consolidated to model the growth mechanism for the observed fractal porous Si NWs.
- ❖ Raman spectroscopic studies of samples fabricated by MIE are analyzed to estimate the sizes of Si NSs using PCM.
- ❖ Asymmetric, red shifted and broad Raman line shapes are observed for Si NSs due to phonon confinement. The two fold approach has been used to understand the asymmetric nature present in the Raman spectra attributed from Si NSs.
- ❖ The Fano resonance has been modelled first theoretically for both bulk and nano forms. This model was later employed on the Raman spectra of Si NSs for both n- and p-type NSs.
- ❖ An anomalous nature of Raman spectral asymmetry has been studied from SiNWs prepared from heavily doped p-type Si wafer. A theoretical framework for supporting the presence of the combined (“FANTUM”) effect has also been proposed to show

how a system with appropriate Fano and quantum effects' relative contribution may result in near-symmetric Raman line-shape.

- ❖ A dual role of Fano resonance in n- and p- type nano system has been observed to modulate Raman spectra differently and reconcile accordingly to enhance and cease the Raman spectral asymmetry respectively.
- ❖ A theoretical line-shape function has been proposed for representing the observed Raman scattering spectrum from amorphous Si based on modified PCM framework.
- ❖ Additionally, an empirical formula has been proposed using bond polarizability model (BPM) for estimating the short range order making one capable to quantify the distance of short range order by looking at the Raman peak position alone.
- ❖ The experimental asymmetric Raman line-shape has been explained by developing a theoretical model which incorporates the quantum confined acoustic phonons interacting with intra-band quasi-continuum available in Si NSs as a result of discretization of energy levels with unequal separation. A phenomenon, similar to Brillouin scattering, is discovered which is possible at nanoscale in low frequency regime and is called "Fano scattering" in general.
- ❖ A method has been proposed to extract information about non radiative transitions from the Fano scattering data where these nonradiative transitions are involved as intra-band quasi-continuum in modulation with discrete acoustic phonons.
- ❖ Diffuse reflectance spectroscopy (DRS) reveal that Si NSs are capable to show the quantum confinement effect as evident from size dependent band gap variation which is in consonance with conclusions drawn using the TEM and Raman scattering.
- ❖ Visible PL at room temperature from Si NSs samples has been observed.
- ❖ The porosity dependent PL lifetime have been observed in the SiNWs fabricated by MIE.
- ❖ Comparative study of DRS, PL spectra and PL lifetime suggest that PL from SiNWs are observed due to Si/SiO_x interface.

8.3 Future Scope

This work is focused on the spectroscopic investigations of low dimension Si fabricated using MIE technique. There is much scope to extend this work further in future. Some possible studies are described below:

- ❖ The Fano scattering can be extended to study the non-radiative transition in p-type Si NSs fabricated using MIE, because LIE technique is incapable to fabricate the Si NSs of p-type Si wafer.
- ❖ The theoretical model for amorphous Si can be extended and developed for other semiconducting nanowires which can help in improving the efficiency of devices like solar cells.
- ❖ A methodology to clearly distinguish the quantum confinement induced PL from the other source can be worked out.
- ❖ Fano scattering can be extended further to explore whether it is of universal nature.
- ❖ An experimental verification of proposed method for extracting non-radiative transitions can be worked out to validate the method further

Appendices

Appendix 1

Silicon elemental facts

Classification:	Si is a metalloid
Atomic weight:	28.0855 g/mol
Density @ 20 °C:	2.33 g/cm ³
Atomic volume:	12.1 cm ³ /mol

States

State:	solid
Melting point:	1687 K (1414 °C)
Boiling point:	3538 K (3265 °C)

Energies

Specific heat capacity:	0.71 J g ⁻¹ K ⁻¹
Heat of fusion:	50.21 kJ mol ⁻¹
1 st ionization energy:	786.4 kJ mol ⁻¹
3 rd ionization energy:	3231.4 kJ mol ⁻¹
Heat of atomization:	456 kJ mol ⁻¹
Heat of vaporization:	359 kJ mol ⁻¹
2 nd ionization energy:	1577 kJ mol ⁻¹
Electron affinity:	133.6 kJ mol ⁻¹

Oxidation & Electrons

Shells	:	2,8,4
Min. oxidation number	:	-4
Min. common oxidation no.	:	-4
Electronegativity (Pauling Scale):	:	1.9
Electron configuration	:	1s ² 2s ² 2p ⁶ 3s ² 3p ²
Max. oxidation number	:	4
Max. common oxidation no.	:	4
Polarizability volume	:	5.4 Å ³

Appearance & Characteristics

Structure	:	diamond structure
Hardness	:	11.9 GPa
Color	:	silvery

Reactions & Compounds

Reaction with air:	none
Reaction with 15 M HNO ₃ :	none
Oxide(s):	SiO ₂
Hydride(s):	SiH ₄ (silane), Si ₂ H ₆ + more
Reaction with 6 M HCl	:none
Reaction with 6 M NaOH	: mild, ⇒ silicates
Chloride(s)	: SiCl ₄ , Si ₂ Cl ₆ + more

Conductivity

Thermal conductivity:	149 W m ⁻¹ K ⁻¹
Electrical conductivity:	1.2 x 10 ⁻⁵ S cm ⁻¹

Abundance & Isotopes

Abundance earth's crust: 28 % by weight, 21 % ppm by moles
Abundance solar system: 900 ppm by weight, 40 ppm

Isotopes

Silicon has 14 isotopes whose half-lives are known, with mass numbers 22 to 36. Of these, three are stable: ²⁸Si, ²⁹Si and ³⁰Si.

Harmful effects

Si is not known to be toxic, but if breathed in as a fine silica/silicate dust it may cause chronic respiratory problems. Silicates such as asbestos are carcinogenic.

Characteristics

Si is a hard, relatively inert metalloid and its crystalline form is very brittle with a marked metallic lustre. Si occurs mainly in nature as the oxide and as silicates. The solid form of Si does not react with oxygen, water and most acids. Si reacts with halogens or dilute alkalis. Si also has the unusual property that it expands as it freezes (like water).

References

[1]. R.W. Cahn, Si: Child and Progenitor of Revolution., Into The

Nano Era, Springer Series in Materials Science, Volume 106. (2009)
p3.

[2]. John Emsley, Nature's Building Blocks: An A-Z Guide to the
Elements., (2002) p387. Oxford University Press.

[3]. H. R. Huff, U. Gösele, H. Tsuya, Semiconductor Silicon., (1998)
p70, The Electrochemical Society.

Appendix 2

“Snake-food” and “continuum-discrete” analogy

- We have given analogy related to the physical phenomena of Fano interaction in terms of biological entities and their food habits.
- If we have consider Interband and Intraband electronic transitions as a python and a cobra respectively corresponding to the size of continuum, we found good analogy in our propose model.
- As optic phonons have higher energy as compare to acoustic phonon we consider a dear and a rat corresponding to these parameters.

Following facts can be related based on Figure A2.1

1. Python can swallow rat but that will make no difference in its shape & size but if it swallows dear, will make clear change in his body structure and that is observable (red circle).

It's like Interband continuum and acoustic phonon can interfere but not observable in terms of Raman line-shape asymmetry.

2. Cobra can't swallow dear relates to no interaction between intraband transition and optic phonon due to energy mismatch and noncompliance of the interference condition. On the other hand cobra can swallow rat and it will make visible changes in its body (red circle) which make clear correlation with acoustic phonon interaction with intraband transition giving rise to Fano scattering and asymmetry in Raman line-shape as in Figure 1 in main text.

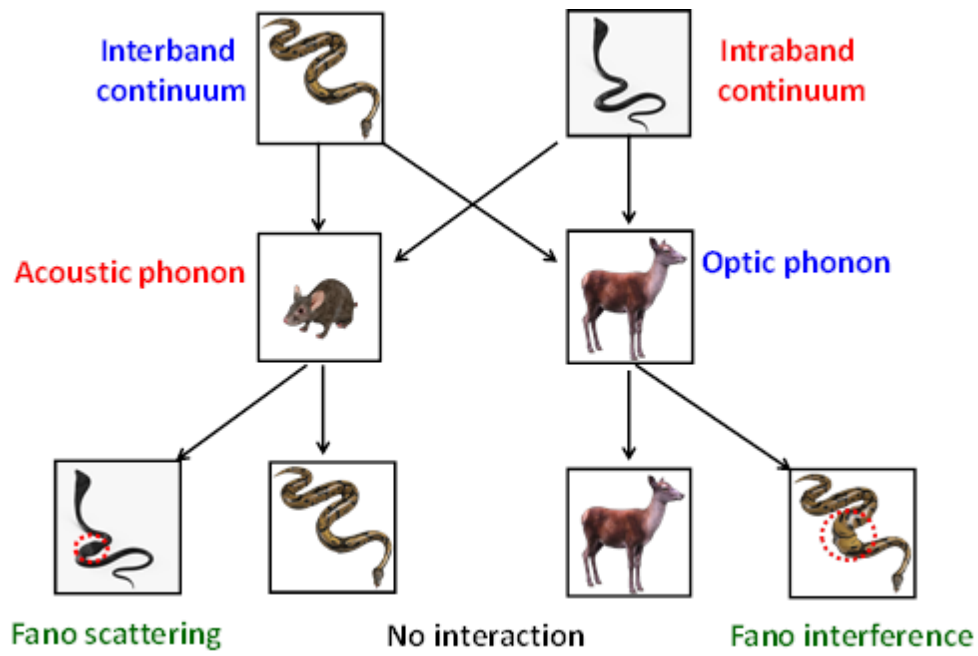


Figure A2.1: Snake-food analogy to explain various combinations of energy continuum-discrete interaction.

Appendix 3

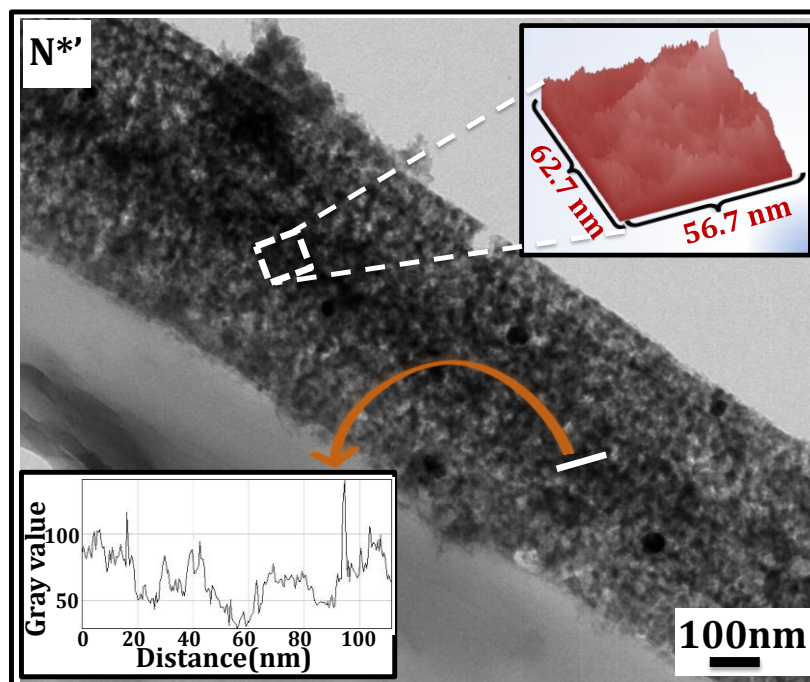


Fig A3.1: TEM image of samples N^{*} prepared by MIE. Inset shows the selected area (marked by white dotted line) 3D surface plot (top inset) of TEM image whereas the solid white line shows the position of TEM used to calculate the line profile (bottom inset) of sample.

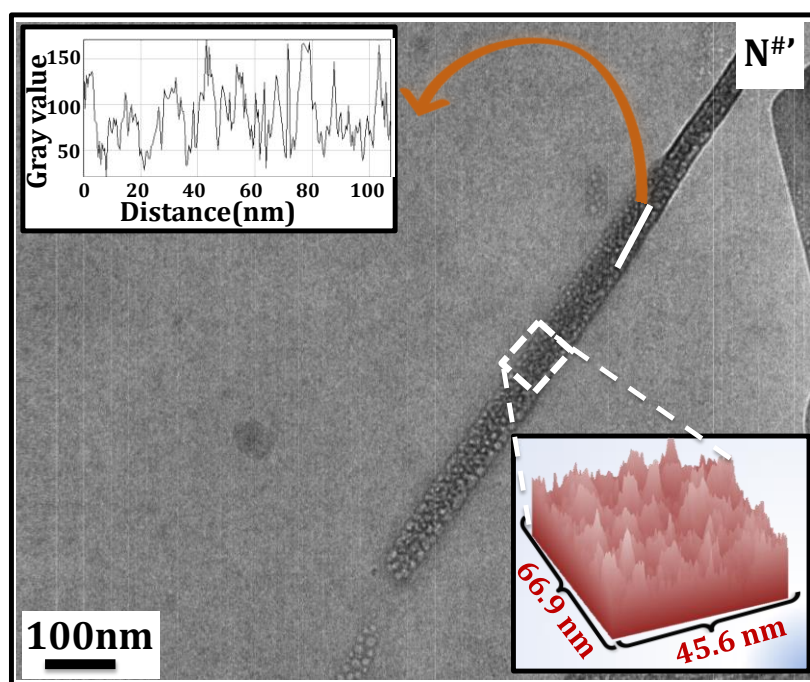


Figure A3.2: TEM image of samples $N^{\#}$ prepared by MIE. Inset

shows the selected area (marked by white dotted line) 3D surface plot (bottom inset) of TEM image whereas the solid white line shows the position of TEM used to calculate the line profile (top inset) of sample.

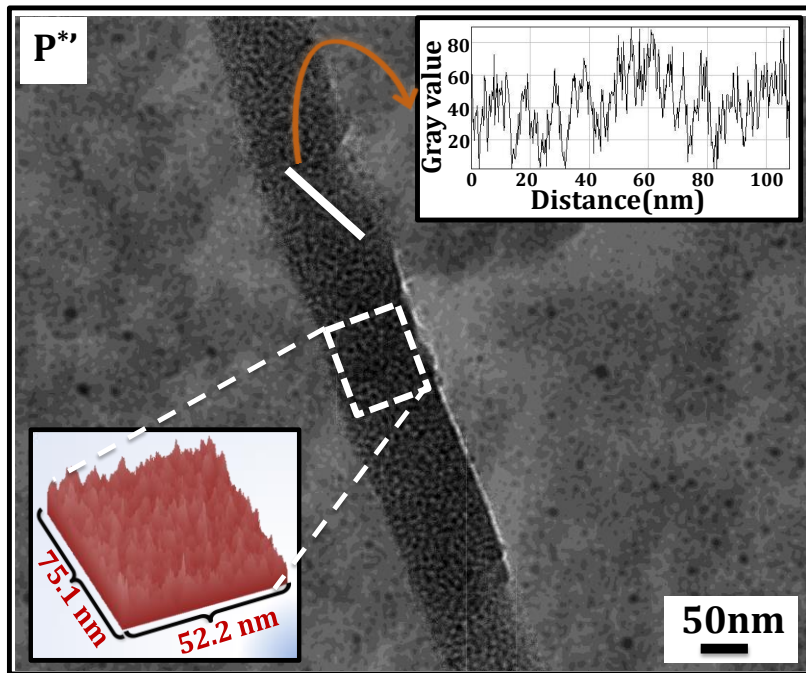


Figure A3.3: TEM image of samples P^* prepared by MIE. Inset shows the selected area (marked by white dotted line) 3D surface plot (bottom inset) of TEM image whereas the solid white line shows the position of TEM used to calculate the line profile (top inset) of sample.

References

- [1] C. Gerber and H. P. Lang, *Nat. Nanotechnol.* (2006).
- [2] A. K. Geim and K. S. Novoselov, *Nat. Mater.* **6**, 183 (2007).
- [3] A. Mnyusiwalla, A. S. Daar, and P. A. Singer, *Nanotechnology* **14**, R9 (2003).
- [4] S. Linic, P. Christopher, and D. B. Ingram, *Nat. Mater.* **10**, 911 (2011).
- [5] C. Toumey, *Nat. Nanotechnol.* (2017).
- [6] F. Priolo, T. Gregorkiewicz, M. Galli, and T. F. Krauss, *Nat. Nanotechnol.* **9**, 19 (2014).
- [7] A. L. Porter and J. Youtie, *Nat. Nanotechnol.* (2009).
- [8] S. Joseph SJ, SR Vol4802 Febr. 2011 (2011).
- [9] S.-E. Cheon, H. Lee, J. Choi, A. R. Jeong, T. S. Lee, D. S. Jeong, K.-S. Lee, W.-S. Lee, W. M. Kim, H. Lee, and I. Kim, *Sci. Rep.* **7**, 7336 (2017).
- [10] V. Narasimhan, R. H. Siddique, J. O. Lee, S. Kumar, B. Ndjamen, J. Du, N. Hong, D. Sretavan, and H. Choo, *Nat. Nanotechnol.* **13**, 512 (2018).
- [11] J. W. Jeong, S. R. Yang, Y. H. Hur, S. W. Kim, K. M. Baek, S. Yim, H.-I. Jang, J. H. Park, S. Y. Lee, C.-O. Park, and Y. S. Jung, *Nat. Commun.* **5**, 5387 (2014).
- [12] H. Weller, *Curr. Opin. Colloid Interface Sci.* **3**, 194 (1998).
- [13] V. H. Grassian, in *Nanoscale Mater. Chem. Environ. Appl.* (American Chemical Society, 2010), pp. 15–33.
- [14] M. L. Brongersma, P. G. Kik, A. Polman, K. S. Min, and H. A. Atwater, *Appl. Phys. Lett.* **76**, 351 (2000).
- [15] H. Shekhar, SR Vol4802 Febr. 2011 (2011).
- [16] T. J. Webster, *Int. J. Nanomedicine* **2**, 1 (2007).
- [17] R. P. Feynman, *J. Microelectromechanical Syst.* **1**, 60 (1992).
- [18] R. Zsigmondy and J. Alexander, *Colloids and the Ultramicroscope: A Manual of Colloid Chemistry and Ultramicroscopy ...* (J. Wiley & sons, 1909).
- [19] Y. Li, F. Qian, J. Xiang, and C. M. Lieber, *Mater. Today* **9**, 18 (2006).
- [20] M. Hasan, M. F. Huq, and Z. H. Mahmood, *SpringerPlus* **2**, 1 (2013).
- [21] H. Mizuta and S. Oda, *Microelectron. J.* **39**, 171 (2008).
- [22] V. S.-Y. Lin, K. Motesharei, K.-P. S. Dancil, M. J. Sailor, and M. R. Ghadiri, *Science* **278**, 840 (1997).
- [23] J. M. Rodríguez, I. Tobías, and A. Luque, *Sol. Energy Mater. Sol. Cells* **45**, 241 (1997).
- [24] S. R. Wenham and M. A. Green, *Prog. Photovolt. Res. Appl.* **4**, 3 (1996).
- [25] Y. Jiang, X. Zhang, F. Wang, and Y. Zhao, *RSC Adv.* **5**, 69629 (2015).
- [26] B. Tian, X. Zheng, T. J. Kempa, Y. Fang, N. Yu, G. Yu, J. Huang, and C. M. Lieber, *Nature* **449**, 885 (2007).
- [27] S. Mishra, H. Pandey, P. Yogi, S. K. Saxena, S. Roy, P. R. Sagdeo, and R. Kumar, *Opt. Mater.* **66**, 65 (2017).

- [28] O. Bisi, S. Ossicini, and L. Pavesi, *Surf. Sci. Rep.* **38**, 1 (2000).
- [29] S. Wippermann, Y. He, M. Vörös, and G. Galli, *Appl. Phys. Rev.* **3**, 40807 (2016).
- [30] X. Li, J.-H. Lee, A. N. Sprafke, and R. B. Wehrspohn, *Semicond. Sci. Technol.* **31**, 14009 (2016).
- [31] K. Peng, A. Lu, R. Zhang, and S.-T. Lee, *Adv. Funct. Mater.* **18**, 3026 (2008).
- [32] K. Peng, X. Wang, and S.-T. Lee, *Appl. Phys. Lett.* **92**, 163103 (2008).
- [33] Zhang Baohua, Wang Haishui, Lu Lehui, Ai Kelong, Zhang Guo, and Cheng Xiaoli, *Adv. Funct. Mater.* **18**, 2348 (2008).
- [34] K.-Q. Peng, X. Wang, and S.-T. Lee, *Appl. Phys. Lett.* **95**, 243112 (2009).
- [35] G. Zheng, F. Patolsky, Y. Cui, W. U. Wang, and C. M. Lieber, *Nat. Biotechnol.* **23**, 1294 (2005).
- [36] T. Takamura, S. Ohara, M. Uehara, J. Suzuki, and K. Sekine, *J. Power Sources* **129**, 96 (2004).
- [37] X. H. Liu, L. Q. Zhang, L. Zhong, Y. Liu, H. Zheng, J. W. Wang, J.-H. Cho, S. A. Dayeh, S. T. Picraux, J. P. Sullivan, S. X. Mao, Z. Z. Ye, and J. Y. Huang, *Nano Lett.* **11**, 2251 (2011).
- [38] L.-F. Cui, Y. Yang, C.-M. Hsu, and Y. Cui, *Nano Lett.* **9**, 3370 (2009).
- [39] K. W. Adu, H. R. Gutiérrez, U. J. Kim, and P. C. Eklund, *Phys. Rev. B* **73**, (2006).
- [40] H. Kim, M. Seo, M.-H. Park, and J. Cho, *Angew. Chem. Int. Ed.* **49**, 2146 (2010).
- [41] J. Theis, M. Geller, A. Lorke, H. Wiggers, A. Wieck, and C. Meier, *Nanotechnology* **21**, 455201 (2010).
- [42] T. M. Atkins, A. Y. Louie, and S. M. Kauzlarich, *Nanotechnology* **23**, 294006 (2012).
- [43] T. Song, J. Xia, J.-H. Lee, D. H. Lee, M.-S. Kwon, J.-M. Choi, J. Wu, S. K. Doo, H. Chang, W. I. Park, D. S. Zang, H. Kim, Y. Huang, K.-C. Hwang, J. A. Rogers, and U. Paik, *Nano Lett.* **10**, 1710 (2010).
- [44] L. Li, Y. Yao, Z. Lin, Y. Liu, and C. P. Wong, in *Electron. Compon. Technol. Conf. ECTC 2013 IEEE 63rd* (2013), pp. 581–585.
- [45] D. Dávila, J. P. Esquivel, N. Sabaté, and J. Mas, *Biosens. Bioelectron.* **26**, 2426 (2011).
- [46] B. S. Flavel, M. J. Sweetman, C. J. Shearer, J. G. Shapter, and N. H. Voelcker, *ACS Appl. Mater. Interfaces* **3**, 2463 (2011).
- [47] L. Stalmans, J. Poortmans, H. Bender, M. Caymax, K. Said, E. Vazsonyi, J. Nijs, and R. Mertens, *Prog. Photovolt. Res. Appl.* **6**, 233 (1998).
- [48] S. K. Saxena, P. Yogi, P. Yadav, S. Mishra, H. Pandey, H. M. Rai, V. Kumar, P. R. Sagdeo, and R. Kumar, *Superlattices Microstruct.* **94**, 101 (2016).
- [49] V. Kumar, S. K. Saxena, V. Kaushik, K. Saxena, A. K. Shukla, and R. Kumar, *RSC Adv.* **4**, 57799 (2014).
- [50] J. Huang, G. Orkoulas, and P. D. Christofides, *Ind. Eng. Chem.*

- Res. **52**, 11246 (2013).
- [51] V. Suwanmethanond, E. Goo, P. K. T. Liu, G. Johnston, M. Sahimi, and T. T. Tsotsis, *Ind. Eng. Chem. Res.* **39**, 3264 (2000).
- [52] E. Vyhmeister, H. Valdés-González, A. J. Muscat, D. Suleiman, and L. A. Estévez, *Ind. Eng. Chem. Res.* **52**, 4762 (2013).
- [53] S. B. Amor, I. Haddadi, E. W. Seif, R. Daik, R. Bousbih, W. Dimassi, and H. Ezzaouia, *Superlattices Microstruct.* **88**, 161 (2015).
- [54] L. T. Canham, *Appl. Phys. Lett.* **57**, 1046 (1990).
- [55] A. G. Cullis and L. T. Canham, *Nature* **353**, 335 (1991).
- [56] F. A. Harraz, A. A. Ismail, H. Bouzid, S. A. Al-Sayari, A. Al-Hajry, and M. S. Al-Assiri, *Phys. Status Solidi A* **212**, 1851 (2015).
- [57] A. G. Cullis, L. T. Canham, and P. D. J. Calcott, *J. Appl. Phys.* **82**, 909 (1997).
- [58] F. Maier-Flaig, J. Rinck, M. Stephan, T. Bocksrocker, M. Bruns, C. Kübel, A. K. Powell, G. A. Ozin, and U. Lemmer, *Nano Lett.* (2013).
- [59] T. Tamura and S. Adachi, *J. Appl. Phys.* **105**, 113518 (2009).
- [60] P. Yogi, S. Mishra, S. K. Saxena, V. Kumar, and R. Kumar, *J. Phys. Chem. Lett.* **7**, 5291 (2016).
- [61] P. Yogi, D. Poonia, S. Mishra, S. K. Saxena, S. Roy, V. Kumar, P. R. Sagdeo, and R. Kumar, *J. Phys. Chem. C* **121**, 5372 (2017).
- [62] S. K. Saxena, R. Borah, V. Kumar, H. M. Rai, R. Late, V. g. Sathe, A. Kumar, P. R. Sagdeo, and R. Kumar, *J. Raman Spectrosc.* **47**, 283 (2016).
- [63] P. Yogi, S. K. Saxena, S. Mishra, H. M. Rai, R. Late, V. Kumar, B. Joshi, P. R. Sagdeo, and R. Kumar, *Solid State Commun.* **230**, 25 (2016).
- [64] I. Sychugov, Y. Nakayama, and K. Mitsuishi, *Nanotechnology* **21**, 285307 (2010).
- [65] A. Giguère, J. Beerens, and B. Terreault, *Nanotechnology* **17**, 600 (2006).
- [66] Y. Ishikawa, N. Shibata, and S. Fukatsu, *Appl. Phys. Lett.* **68**, 2249 (1996).
- [67] Z. Peng, H. Hu, M. I. B. Utama, L. M. Wong, K. Ghosh, R. Chen, S. Wang, Z. Shen, and Q. Xiong, *Nano Lett.* **10**, 3940 (2010).
- [68] E. López-Camacho, M. Fernández, and C. Gómez-Aleixandre, *J. Nanosci. Nanotechnol.* **9**, 4187 (2009).
- [69] T. C. Patil, P. Mahajan, and S. Chakrabarti, *Superlattices Microstruct.* **48**, 190 (2010).
- [70] R. W. Fathauer, T. George, A. Ksendzov, and R. P. Vasquez, *Appl. Phys. Lett.* **60**, 995 (1992).
- [71] C. H. Choy and K. W. Cheah, *Appl. Phys. A* **61**, 45 (1995).
- [72] R. Kumar and A. K. Shukla, *Phys. Lett. A* **373**, 2882 (2009).
- [73] M. Abouda-Lachiheb, N. Nafie, and M. Bouaicha, *Nanoscale Res. Lett.* **7**, 455 (2012).
- [74] B. González-Díaz, R. Guerrero-Lemus, N. Marrero, C. Hernández-Rodríguez, F. A. Ben-Hander, and J. M. Martínez-Duart, *J. Phys. Appl. Phys.* **39**, 631 (2006).
- [75] Z. Huang, N. Geyer, P. Werner, J. de Boer, and U. Gösele, *Adv.*

- Mater. **23**, 285 (2011).
- [76] K. Peng, Y. Xu, Y. Wu, Y. Yan, S.-T. Lee, and J. Zhu, *Small* **1**, 1062 (2005).
- [77] S. D. Campbell, L. A. Jones, E. Nakamichi, F. -X. Wei, L. D. Zajchowski, and D. F. Thomas, *J. Vac. Sci. Technol. B Microelectron. Nanometer Struct. Process. Meas. Phenom.* **13**, 1184 (1995).
- [78] S. K. Saxena, V. Kumar, H. M. Rai, G. Sahu, R. Late, K. Saxena, A. K. Shukla, P. R. Sagdeo, and R. Kumar, *Silicon* **1** (2015).
- [79] H. S. Mavi, S. Prusty, M. Kumar, R. Kumar, A. K. Shukla, and S. Rath, *Phys. Status Solidi -Appl. Mater. Sci.* **203**, 2444 (2006).
- [80] L. Lin, S. Guo, X. Sun, J. Feng, and Y. Wang, *Nanoscale Res. Lett.* **5**, 1822 (2010).
- [81] X. Li and P. W. Bohn, *Appl. Phys. Lett.* **77**, 2572 (2000).
- [82] M. Dovrat, *Phys. Rev. B* **75**, (2007).
- [83] L. H. Lin, X. Z. Sun, R. Tao, Z. C. Li, J. Y. Feng, and Z. J. Zhang, *J. Appl. Phys.* **110**, 73109 (2011).
- [84] G. Ledoux, J. Gong, F. Huisken, O. Guillois, and C. Reynaud, *Appl. Phys. Lett.* **80**, 4834 (2002).
- [85] C. M. Hessel, J. Wei, D. Reid, H. Fujii, M. C. Downer, and B. A. Korgel, *J. Phys. Chem. Lett.* **3**, 1089 (2012).
- [86] A. S. Krylov, E. M. Merkushova, A. N. Vtyurin, and L. I. Isaenko, *Phys. Solid State* **54**, 1275 (2012).
- [87] G. Gouadec and P. Colomban, *Prog. Cryst. Growth Charact. Mater.* **53**, 1 (2007).
- [88] R. Kumar and A. K. Shukla, *Phys. Lett. A* **373**, 133 (2008).
- [89] N. Fukata, *Adv. Mater.* **21**, 2829 (2009).
- [90] R. Kumar, G. Sahu, S. K. Saxena, H. M. Rai, and P. R. Sagdeo, *Silicon* **6**, 117 (2014).
- [91] H. Richter, Z. P. Wang, and L. Ley, *Solid State Commun.* **39**, 625 (1981).
- [92] N. Fukata, T. Oshima, K. Murakami, T. Kizuka, T. Tsurui, and S. Ito, *Appl. Phys. Lett.* **86**, 213112 (2005).
- [93] J. R. Lombardi and R. L. Birke, *J. Phys. Chem. C* **114**, 7812 (2010).
- [94] Q. Hao, B. K. Juluri, Y. B. Zheng, B. Wang, I.-K. Chiang, L. Jensen, V. Crespi, P. C. Eklund, and T. J. Huang, *J. Phys. Chem. C* **114**, 18059 (2010).
- [95] C. L. Baldwin, N. W. Bigelow, and D. J. Masiello, *J. Phys. Chem. Lett.* **5**, 1347 (2014).
- [96] D. M. Sagar, J. M. Atkin, P. K. B. Palomaki, N. R. Neale, J. L. Blackburn, J. C. Johnson, A. J. Nozik, M. B. Raschke, and M. C. Beard, *Nano Lett.* **15**, 1511 (2015).
- [97] M. Jouanne, R. Beserman, I. Ipatova, and A. Subashiev, *Solid State Commun.* **16**, 1047 (1975).
- [98] Y. Li, Y. Yi, V. Coropceanu, and J.-L. Brédas, *Phys. Rev. B* **85**, (2012).
- [99] L. Canham, in *Handb. Porous Silicon*, edited by L. Canham (Springer International Publishing, 2014), pp. 1–8.
- [100] M. L. Schultz, *Infrared Phys.* **4**, 93 (1964).

- [101] M. Cardona and F. H. Pollak, *Phys. Rev.* **142**, 530 (1966).
- [102] W.-W. Zhang, H. Yu, S.-Y. Lei, and Q.-A. Huang, *J. Micromechanics Microengineering* **22**, 85007 (2012).
- [103] R. Tubino, L. Piseri, and G. Zerbi, *J. Chem. Phys.* **56**, 1022 (1972).
- [104] V. Y. Davydov, A. A. Klochikhin, A. N. Smirnov, I. Y. Strashkova, A. S. Krylov, H. Lu, W. J. Schaff, H.-M. Lee, Y.-L. Hong, and S. Gwo, *Phys. Rev. B* **80**, 81204 (2009).
- [105] S. Wei and M. Y. Chou, *Phys. Rev. B* **50**, 2221 (1994).
- [106] A. M. Fox, *Optical Properties of Solids* (Oxford University Press, 2001).
- [107] S. M. Sze and K. K. Ng, *Physics of Semiconductor Devices* (John Wiley & Sons, 2006).
- [108] F. Gonella and P. Mazzoldi, *Handbook of Nanostructured Materials and Nanotechnology* (Academic Press, San Diego, 2000).
- [109] Y. Zhu and J. Appenzeller, *Nanoscale Res. Lett.* **10**, (2015).
- [110] Kittel, *INTRODUCTION TO SOLID STATE PHYSICS, 7TH ED* (John Wiley & Sons, 2007).
- [111] A. D. Yoffe, *Adv. Phys.* (2006).
- [112] C. V. Raman and K. S. Krishnan, *Nature* **121**, 501 (1928).
- [113] R. Loudon, *Adv. Phys.* **13**, 423 (1964).
- [114] R. Loudon, *Proc R Soc Lond A* **275**, 218 (1963).
- [115] P. A. Temple and C. E. Hathaway, *Phys. Rev. B* **7**, 3685 (1973).
- [116] H. J. Fan, M. H. Kuok, S. C. Ng, R. Boukherroub, J.-M. Baribeau, J. W. Fraser, and D. J. Lockwood, *Phys. Rev. B* **65**, 165330 (2002).
- [117] V. Paillard, P. Puech, M. A. Laguna, R. Carles, B. Kohn, and F. Huisken, *J. Appl. Phys.* **86**, 1921 (1999).
- [118] J. Zi, K. Zhang, and X. Xie, *Phys. Rev. B* **55**, 9263 (1997).
- [119] Null Simonian, null Sproul, null Shi, and null Gauja, *Phys. Rev. B Condens. Matter* **52**, 5672 (1995).
- [120] M. Chandrasekhar, J. B. Renucci, and M. Cardona, *Phys. Rev. B* **17**, 1623 (1978).
- [121] U. Fano, *Phys. Rev.* **124**, 1866 (1961).
- [122] E. Burstein, D. L. Mills, and R. F. Wallis, *Phys. Rev. B* **4**, 2429 (1971).
- [123] J. B. Renucci, R. N. Tyte, and M. Cardona, *Phys. Rev. B* **11**, 3885 (1975).
- [124] D. Bermejo and M. Cardona, *J. Non-Cryst. Solids* **32**, 405 (1979).
- [125] M. H. Brodsky, in *Light Scatt. Solids I* (Springer Berlin Heidelberg, 1983), pp. 205–251.
- [126] J. S. Lannin, *Solid State Commun.* **12**, 947 (1973).
- [127] M. Wihl, M. Cardona, and J. Tauc, *J. Non-Cryst. Solids* **8**, 172 (1972).
- [128] J. E. Smith, M. H. Brodsky, B. L. Crowder, M. I. Nathan, and A. Pinczuk, *Phys. Rev. Lett.* **26**, 642 (1971).
- [129] C. Thomsen and E. Bustarret, *J. Non-Cryst. Solids* **141**, 265 (1992).

- [130] R. L. C. Vink, G. T. Barkema, and W. F. van der Weg, *Phys. Rev. B* **63**, 115210 (2001).
- [131] M. Marinov and N. Zotov, *Phys. Rev. B* **55**, 2938 (1997).
- [132] D. Beeman, R. Tsu, and M. F. Thorpe, *Phys. Rev. B* **32**, 874 (1985).
- [133] R. Shuker and R. W. Gammon, *Phys. Rev. Lett.* **25**, 222 (1970).
- [134] S. Amdouni, M. Rahmani, M.-A. Zaïbi, and M. Oueslati, *J. Lumin.* **157**, 93 (2015).
- [135] J. P. Proot, C. Delerue, and G. Allan, *Appl. Phys. Lett.* **61**, 1948 (1992).
- [136] G. D. Sanders and Y.-C. Chang, *Phys. Rev. B* **45**, 9202 (1992).
- [137] S. Chattopadhyay, X. Li, and P. W. Bohn, *J. Appl. Phys.* **91**, 6134 (2002).
- [138] A. J. Read, R. J. Needs, K. J. Nash, L. T. Canham, P. D. J. Calcott, and A. Qteish, *Phys. Rev. Lett.* **69**, 1232 (1992).
- [139] T. Ito, T. Ohta, and A. Hiraki, *Jpn. J. Appl. Phys.* **31**, L1 (1992).
- [140] W. Ding, J. Zheng, W. Qi, W. Yu, and G. Fu, in (2008), pp. 713508-713508–9.
- [141] O. Demichel, V. Calvo, P. Noé, B. Salem, P.-F. Fazzini, N. Pauc, F. Oehler, P. Gentile, and N. Magnea, *Phys. Rev. B* **83**, 245443 (2011).
- [142] G. Ledoux, O. Guillois, D. Porterat, C. Reynaud, F. Huisken, B. Kohn, and V. Paillard, *Phys. Rev. B* **62**, 15942 (2000).
- [143] G. Ouyang, A. Zhang, Z. Zhu, W. Zhu, and G. Yang, *J. Appl. Phys.* **110**, 33507 (2011).
- [144] M. S. Brandt, H. D. Fuchs, M. Stutzmann, J. Weber, and M. Cardona, *Solid State Commun.* **81**, 307 (1992).
- [145] L. Tsybeskov and P. M. Fauchet, *Appl. Phys. Lett.* **64**, 1983 (1994).
- [146] K. Balasundaram, J. S. Sadhu, J. C. Shin, B. Azeredo, D. Chanda, M. Malik, K. Hsu, J. A. Rogers, P. Ferreira, S. Sinha, and X. Li, *Nanotechnology* **23**, 305304 (2012).
- [147] B. M. Bang, H. Kim, H.-K. Song, J. Cho, and S. Park, *Energy Environ. Sci.* **4**, 5013 (2011).
- [148] K. K. Al-Khazraji, B. G. Rasheeda, M. A. Ibrahim, and A. F. Mohammed, *Procedia Eng.* **38**, 1381 (2012).
- [149] R. Kumar, A. K. Shukla, B. Joshi, and S. S. Islam, *Jpn. J. Appl. Phys.* **47**, 8461 (2008).
- [150] R. Kumar, H. S. Mavi, and A. K. Shukla, *Silicon* **2**, 25 (2010).
- [151] J. Gonzalez-Hernandez, G. H. Azarbajegani, R. Tsu, and F. H. Pollak, *Appl. Phys. Lett.* **47**, 1350 (1985).
- [152] N. Hondow, R. Brydson, and A. Brown, *J. Phys. Conf. Ser.* **522**, 12055 (2014).
- [153] C. V. Raman, *Curr. Sci.* **74**, 382 (1998).
- [154] V. J. Cadarso, N. Chidambaram, L. Jacot-Descombes, and H. Schiff, *Microsyst. Nanoeng.* **3**, 17017 (2017).
- [155] P. Yogi, S. K. Saxena, A. Chaudhary, D. K. Pathak, S. Mishra, P. Mondal, B. Joshi, P. R. Sagdeo, and R. Kumar, *Superlattices Microstruct.* **120**, 141 (2018).
- [156] P. Kubelka, *JOSA* **38**, 448 (1948).

- [157] V. Mishra, A. Sagdeo, V. Kumar, M. K. Warshi, H. M. Rai, S. K. Saxena, D. R. Roy, V. Mishra, R. Kumar, and P. R. Sagdeo, *J. Appl. Phys.* **122**, 65105 (2017).
- [158] J. H. Nobbs, *Rev. Prog. Color. Relat. Top.* **15**, 66 (1985).
- [159] J. R. Lakowicz, *Principles of Fluorescence Spectroscopy*, 3rd ed. (Springer US, 2006).
- [160] K. A. Zachariasse, *Nachrichten Aus Chem. Tech. Lab.* **33**, 896 (1985).
- [161] A. Backes, A. Bittner, M. Leitgeb, and U. Schmid, *Scr. Mater.* **114**, 27 (2016).
- [162] S. K. Saxena, G. Sahu, V. Kumar, P. K. Sahoo, P. R. Sagdeo, and R. Kumar, *Mater. Res. Express* **2**, 36501 (2015).
- [163] H. He, C. Liu, L. Sun, and Z. Ye, *Appl. Phys. Lett.* **99**, 123106 (2011).
- [164] Y. Qi, Z. Wang, M. Zhang, F. Yang, and X. Wang, *J. Phys. Chem. C* **117**, 25090 (2013).
- [165] A. P. Bonifas and R. L. McCreery, *Anal Chem* **84**, 2459 (2012).
- [166] V. Lehmann and H. Föll, *J. Electrochem. Soc.* **137**, 653 (1990).
- [167] P. Yogi, D. Poonia, P. Yadav, S. Mishra, S. K. Saxena, S. Roy, P. R. Sagdeo, and R. Kumar, *Silicon* **1** (2018).
- [168] S. K. Saxena, P. Yogi, S. Mishra, H. Mohan Rai, V. Mishra, M. Kamal Warshi, S. Roy, P. Mondal, P. R. Sagdeo, and R. Kumar, *Phys. Chem. Chem. Phys.* **19**, 31788 (2017).
- [169] Y. Chen, B. Peng, and B. Wang, *J. Phys. Chem. C* **111**, 5855 (2007).
- [170] B. Li, D. Yu, and S.-L. Zhang, *Phys. Rev. B* **59**, 1645 (1999).
- [171] K. W. Adu, H. R. Gutiérrez, U. J. Kim, G. U. Sumanasekera, and P. C. Eklund, *Nano Lett.* **5**, 409 (2005).
- [172] K. W. Adu, Q. Xiong, H. R. Gutierrez, G. Chen, and P. C. Eklund, *Appl. Phys. A* **85**, 287 (2006).
- [173] I. H. Campbell and P. M. Fauchet, *Solid State Commun.* **58**, 739 (1986).
- [174] G. Faraci, S. Gibilisco, P. Russo, A. R. Pennisi, and S. La Rosa, *Phys. Rev. B* **73**, 33307 (2006).
- [175] K. W. Adu, H. R. Gutierrez, and P. C. Eklund, *Vib. Spectrosc.* **42**, 165 (2006).
- [176] D. Abidi, B. Jusserand, and J.-L. Fave, *Phys. Rev. B* **82**, 75210 (2010).
- [177] R. Gupta, K. P. Jain, S. C. Abbi, and M. Balkanski, *Solid State Commun.* **55**, 285 (1985).
- [178] J. Zi, H. Büscher, C. Falter, W. Ludwig, K. Zhang, and X. Xie, *Appl. Phys. Lett.* **69**, 200 (1996).
- [179] F. J. Bartoli and T. A. Litovitz, *J. Chem. Phys.* **56**, 404 (1972).
- [180] M. P. Chamberlain, C. Trallero-Giner, and M. Cardona, *Phys. Rev. B* **51**, 1680 (1995).
- [181] C. Trallero-Giner, A. Debernardi, M. Cardona, E. Menéndez-Proupín, and A. I. Ekimov, *Phys. Rev. B* **57**, 4664 (1998).
- [182] M. I. Vasilevskiy, A. G. Rolo, and M. J. M. Gomes, *Solid State Commun.* **104**, 381 (1997).
- [183] T. Lopez and L. Mangolini, *Nanoscale* **6**, 1286 (2014).

- [184] R. Al-Salman, J. Mallet, M. Molinari, P. Fricoteaux, F. Martineau, M. Troyon, S. Z. E. Abedin, and F. Endres, *Phys. Chem. Chem. Phys.* **10**, 6233 (2008).
- [185] P. Alfaro, R. Cisneros, M. Bizarro, M. Cruz-Irisson, and C. Wang, *Nanoscale* **3**, 1246 (2011).
- [186] X. Jia, Z. Lin, T. Zhang, B. Puthen-Veetil, T. Yang, K. Nomoto, J. Ding, G. Conibeer, and I. Perez-Wurfl, *RSC Adv.* **7**, 34244 (2017).
- [187] İ. Doğan and M. C. M. van de Sanden, *J. Appl. Phys.* **114**, 134310 (2013).
- [188] M. Tanwar, P. Yogi, S. Lambora, S. Mishra, S. K. Saxena, P. R. Sagdeo, A. S. Krylov, and R. Kumar, *Adv. Mater. Process. Technol.* **0**, 1 (2017).
- [189] S. Ves, I. Loa, K. Syassen, F. Widulle, and M. Cardona, *Phys. Status Solidi B* **223**, 241 (2001).
- [190] N. H. Nickel, P. Lengsfeld, and I. Sieber, *Phys. Rev. B* **61**, 15558 (2000).
- [191] A. T. Voutsas, M. K. Hatalis, J. Boyce, and A. Chiang, *J. Appl. Phys.* **78**, 6999 (1995).
- [192] W.-E. Hong and J.-S. Ro, *J. Appl. Phys.* **114**, 73511 (2013).
- [193] G. P. Gopal, E. W. Roger, K. S. Ashok, L. Changwoo, J. A. Nicholas, E. Harry, H. Pradeep, and L. H. Jennifer, *Adv. Mater. Phys. Chem.* **2012**, (2012).
- [194] P. Yogi, M. Tanwar, S. K. Saxena, S. Mishra, D. K. Pathak, A. Chaudhary, P. R. Sagdeo, and R. Kumar, *Anal. Chem.* (2018).
- [195] C. Gérard, A. Martinez, and D. Robert, *Commun. Math. Phys.* **121**, 323 (1989).
- [196] E. Janzén, G. Grossmann, R. Stedman, and H. G. Grimmeiss, *Phys. Rev. B* **31**, 8000 (1985).
- [197] S.-J. Xiong and Y. Yin, *Phys. Rev. B* **66**, 153315 (2002).
- [198] S. Bar-Ad, P. Kner, M. V. Marquezini, S. Mukamel, and D. S. Chemla, *Phys. Rev. Lett.* **78**, 1363 (1997).
- [199] Y. S. Joe, A. M. Satanin, and C. S. Kim, *Phys. Scr.* **74**, 259 (2006).
- [200] J. Faist, F. Capasso, C. Sirtori, K. W. West, and L. N. Pfeiffer, *Nature* **390**, 589 (1997).
- [201] M. Kroner, A. O. Govorov, S. Remi, B. Biedermann, S. Seidl, A. Badolato, P. M. Petroff, W. Zhang, R. Barbour, B. D. Gerardot, R. J. Warburton, and K. Karrai, *Nature* **451**, 311 (2008).
- [202] L. E. Calvet, J. P. Snyder, and W. Wernsdorfer, *Phys. Rev. B* **83**, 205415 (2011).
- [203] R. Gajić, D. Braun, F. Kuchar, A. Golubović, R. Korntner, H. Löschner, J. Butschke, R. Springer, and F. Letzkus, *J. Phys. Condens. Matter* **15**, 2923 (2003).
- [204] D. M. Cardamone, C. A. Stafford, and S. Mazumdar, *Nano Lett.* **6**, 2422 (2006).
- [205] J. R. Lombardi and R. L. Birke, *J. Chem. Phys.* **136**, 144704 (2012).
- [206] A. E. Miroshnichenko, S. Flach, and Y. S. Kivshar, *Rev. Mod. Phys.* **82**, 2257 (2010).

- [207] Y. G. Wang, S. P. Lau, B. K. Tay, and X. H. Zhang, *J. Appl. Phys.* **92**, 7253 (2002).
- [208] K. Jin and S. J. Xu, *Appl. Phys. Lett.* **90**, 32107 (2007).
- [209] D. Pröpper, A. N. Yaresko, T. I. Larkin, T. N. Stanislavchuk, A. A. Sirenko, T. Takayama, A. Matsumoto, H. Takagi, B. Keimer, and A. V. Boris, *Phys. Rev. Lett.* **112**, 87401 (2014).
- [210] J. Humlíček, *Thin Solid Films* **313–314**, 656 (1998).
- [211] V. A. Volodin and M. D. Efremov, *J. Exp. Theor. Phys. Lett.* **82**, 86 (2005).
- [212] B. G. Burke, J. Chan, K. A. Williams, Z. Wu, A. A. Puretzky, and D. B. Geohegan, *J. Raman Spectrosc.* **41**, 1759 (2010).
- [213] R. Kumar, H. S. Mavi, A. K. Shukla, and V. D. Vankar, *J. Appl. Phys.* **101**, 64315 (2007).
- [214] N. Fukata, K. Sato, M. Mitome, Y. Bando, T. Sekiguchi, M. Kirkham, J. Hong, Z. L. Wang, and R. L. Snyder, *ACS Nano* **4**, 3807 (2010).
- [215] R. Gupta, Q. Xiong, C. K. Adu, U. J. Kim, and P. C. Eklund, *Nano Lett* **3**, 627 (2003).
- [216] R. Kumar, A. K. Shukla, H. S. Mavi, and V. D. Vankar, *Nanoscale Res. Lett.* **3**, 105 (2008).
- [217] M. Balkanski, K. Jain, R. Beserman, and M. Jouanne, *Phys. Rev. B* **12**, 4328 (1975).
- [218] A. K. Shukla and V. Kumar, *J. Appl. Phys.* **110**, (2011).
- [219] X. L. Wu, S. J. Xiong, L. T. Sun, J. C. Shen, and P. K. Chu, *Small* **5**, 2823 (2009).
- [220] A. G. Milekhin, L. L. Sveshnikova, T. A. Duda, N. A. Yeryukov, E. E. Rodyakina, A. K. Gutakovskii, S. A. Batsanov, A. V. Latyshev, and D. R. T. Zahn, *Phys. E Low-Dimens. Syst. Nanostructures* **75**, 210 (2016).
- [221] Y. Feng, S. Lin, S. Huang, S. Shrestha, and G. Conibeer, *J. Appl. Phys.* **117**, 125701 (2015).
- [222] A. Escobedo Morales, E. Sánchez Mora, and U. Pal, *Rev. Mex. Fis. Suppl.* **53**, 18 (2007).
- [223] A. B. Murphy, *Sol. Energy Mater. Sol. Cells* **91**, 1326 (2007).
- [224] R. T. Collins, P. M. Fauchet, and M. A. Tischler, *Phys. Today* **50**, 24 (2008).
- [225] N.-M. Park, T.-S. Kim, and S.-J. Park, *Appl. Phys. Lett.* **78**, 2575 (2001).
- [226] X. Zhang, Q.-H. Tan, J.-B. Wu, W. Shi, and P.-H. Tan, *Nanoscale* **8**, 6435 (2016).
- [227] J. H. Kim, H. H. An, and C. S. Yoon, *J. Appl. Phys.* **105**, 76102 (2009).
- [228] C. Wu, W. Qin, G. Qin, D. Zhao, J. Zhang, W. Xu, and H. Lin, *Chem. Phys. Lett.* **378**, 368 (2003).
- [229] S. Kim, C. O. Kim, D. H. Shin, S. H. Hong, M. C. Kim, J. Kim, S.-H. Choi, T. Kim, R. G. Elliman, and Y.-M. Kim, *Nanotechnology* **21**, 205601 (2010).
- [230] R. Ghosh, P. K. Giri, K. Imakita, and M. Fujii, *Nanotechnology* **25**, 45703 (2014).